DESIGN OF A CLOSED LOOP WIRELESS POWER TRANSFER SYSTEM FOR AN ELECTROCORTICOGRAPHY DEVICE TO BE IMPLANTED IN THE BRAIN OF A RAT OVER AN EXTENDED PERIOD

by

Jeremiah Luke Stuemke

A thesis submitted to the faculty of
The University of North Carolina at Charlotte
in partial fulfillment of the requirements
for the degree of Master of Science in
Electrical Engineering

Charlotte

2018

Approved by:

_____
Dr. Ryan Adams

_____
Dr. Jeremy Holleman

_____
Dr. Tom Weldon

ABSTRACT

JEREMIAH LUKE STUEMKE. Design of a closed loop wireless power transfer system for an electrocorticography device to be implanted in the brain of a rat over an extended period. (Under the direction of DR. RYAN ADAMS)

A biomedical power and communications system is currently under development for the purpose of continuously monitoring neural activity in rats with epilepsy over a period of nine months. A closed loop system is employed that dynamically adjusts for optimal performance across a variety of conditions, such as motion of the rat in its environment. The system is designed to deliver 250 mW to the implant wirelessly at 13.56 MHz power carrier over distances ranging from 1 cm to 25 cm. The total system efficiency is theorized to be at least 15%, which is consistent with current state of the art. The analysis and design of such a biomedically implantable system is discussed in detail and specific components are chosen such that a prototype may be constructed in future work.

ACKNOWLEDGEMENTS

I would like to thank Dr. Adams, whose knowledge and experience were invaluable to the project. I would like to thank Dr. Holleman, who spent many hours helping me think through problems related to the project. I would also like to thank Dr. Weldon, who taught me to question everything, including what I think of as fact.

DEDICATION

To Kyle T. Stewart, a great friend. Miss ya, bud.

TABLE OF CONTENTS

LIST OF FIGURES

LIST OF TABLES

CHAPTER 1: INTRODUCTION

1.1 Background Information

The discussion of wireless power transfer for biomedical implants is a broad topic that encompasses many fields of expertise. This section discusses the relevant information needed to begin thinking about the types of problems encountered when designing an implantable unit.

1.1.1 Epilepsy and Neural Recording

Epilepsy is a neurological disease that is developed by 1 in 26 individuals in the United States at some point during their lives. The disease is characterized by having chronic seizures, although it is possible to have seizures without having epilepsy. Prior to 2014, Epilepsy was referred to as a disorder, but its escalation led to reclassification as a disease by the International League Against Epilepsy (ILAE) in order to inform the public of its seriousness [14].

One method of gathering data of brain activity is known as electroencephalography (EEG), which involves implanting an electrode array on the surface of the skull to detect electrical signals produced by neurons, known as local field potentials (LFPs). A similar method of gathering brain data is known as electrocorticography (ECoG) in which electrodes are placed on the surface of the brain. For this reason, electrocorticography is also referred to as an intracranial EEG (icEEG). An example of neural signals acquired through EEG is depicted in Figure 1.1.

This work seeks to interface with an electrode array that was patented previously by members in association with this work [15]. This array is fault-tolerant, consisting of a grid of primary electrodes and backup electrodes and dedicated control circuitry that

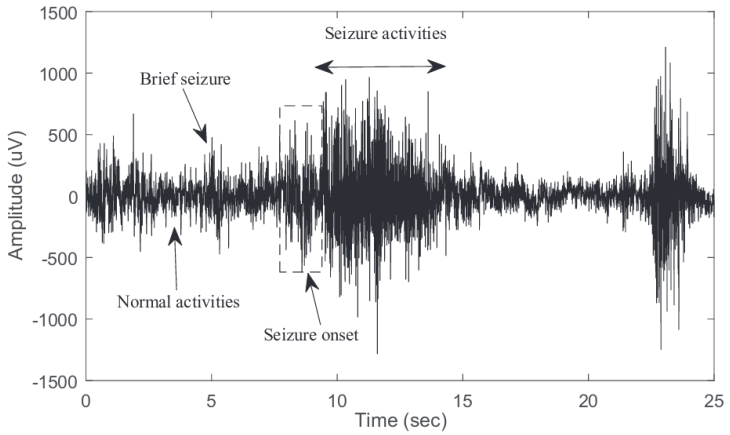

Figure 1.1: An example of an EEG depicting local field potentials over a time span containing seizures [1].

handles the replacement of primary electrodes in the event of a fault. The electrodes have been designed on a flexible material that sits on the surface of the brain tissue in order to measure the ECoG signals.

1.1.2 Specifications and Scope

This work is one piece of a combined effort between the University of North Carolina at Charlotte and Yale University to develop a neural monitoring system for the purpose of studying epilepsy by gathering data from the brain of a rat over an extended period of time. The contributions discussed in this work are specifically related to first and foremost **i)** the wireless powering of the implant and second **ii)** the obtaining of neural data. All other aspects of the over-arching project are outside the scope of this thesis.

The environment inhabited by the test subject (henceforth referred to as "the cage") is a plexiglass boundary of square cross section with side length 30.48 cm and a height of 22.86 cm.

Table 1.1: The list of measurable specifications required for successful completion of the project.

Reference	Category	Minimum	Maximum	Units	Description
S.00	Purpose	–	–	True/False	Should be implanted in the brain of a rat.
S.01	Data Rate	1.0	8.0	Mbps	Should sample neural data adequately to reconstruct the signals.
S.02	Bio-Compatibility	0.0	1.6	W/kg	SAR should not exceed FCC limits.
S.03	Size	0.0×0.0×0.0	2.0×2.0×0.8	cm^3	Implant dimensions should allow for implanting
S.04	Power Data Integrity	0.0	0.1	%	Power packet error rate for any point in cage volume.
S.05	Power Data Integrity	0.0	0.1	%	Power packet error rate for any implant orientation.
S.06	Operating Life	9.0	–	Months	Implant should operate continuously without failure.
S.07	Frequency	–	–	True/False	Power delivery should occur in an FCC allotted ISM band.

Normal operation is defined as successful transmission of data packets with a maximum dropped packet rate of 0.1%. The Federal Communications Commission (FCC) specifies an upper limit for public exposure from cellular telephones to a SAR of 1.6 watts per kilogram. This FCC limit is adopted here as a reasonable metric, even though this project does not involve human interaction with radiation from cellular phones. The restrictions on data-rate are calculated based on an array of 32 electrodes with 16-bit ADC and signals in the range of 300 Hz – 7 kHz. The data rate is computed using (1.1).

$$\text{Rate} = N\frac{\text{samples/s}}{\text{channel}} \times C \text{ channels} \times M\frac{\text{bits}}{\text{sample}} \tag{1.1}$$

1.1.3 Modeling Biological Tissue

In general, biological tissue is considered to be a dielectric material with no strong magnetic response (i.e. $\mu = \mu_0$). In order to account for loss, the permittivity is modeled as a frequency dependent complex number (1.2).

$$\hat{\varepsilon}(\omega) = \varepsilon'(\omega) - j\varepsilon''(\omega) \tag{1.2}$$

Extensive research has been performed to determine appropriate functions for $\varepsilon'(\omega)$ and $\varepsilon''(\omega)$ in biological media. Notably is the work by Cole and Cole who developed

the Cole-Cole dispersion equation (1.3).

$$\frac{\hat{\varepsilon}(\omega)}{\varepsilon_0} = \varepsilon_\infty + \sum_n \frac{\Delta\varepsilon_n}{1 + (j\omega\tau_n)^{1-\alpha_n}} + \frac{\sigma_i}{j\omega\varepsilon_0} \tag{1.3}$$

Here, τ is the relaxation time constant of the polarization, ε_∞ is the permittivity when $\omega\tau \gg 1$, ε_s is the permittivity when $\omega\tau \ll 1$. ε_0 is the permittivity of free-space, σ_i is the static ionic conductivity, and α is a parameter to describe the distribution of the dispersion. The sum term contains as many terms as necessary to adequately model the particular tissue. In this work, a four term Cole-Cole model is used.

$$\begin{aligned}
\varepsilon_r &= \mathrm{Re}\left\{\frac{\hat{\varepsilon}(\omega)}{\varepsilon_0}\right\} \\
&= \varepsilon_\infty + \sum_n \frac{1 + (\omega\tau_n)^{1-\alpha_n}\cos\left(\frac{\pi}{2}(1-\alpha_n)\right)}{1 + (\omega\tau_n)^{2(1-\alpha_n)} + 2(\omega\tau_n)^{1-\alpha_n}\cos\left(\frac{\pi}{2}(1-\alpha_n)\right)}\Delta\varepsilon_n
\end{aligned} \tag{1.4}$$

$$\begin{aligned}
\sigma &= -\omega\mathrm{Im}\left\{\hat{\varepsilon}(\omega)\right\} \\
&= \sigma_i + \omega\varepsilon_0 \sum_n \frac{(\omega\tau_n)^{1-\alpha_n}\sin\left(\frac{\pi}{2}(1-\alpha_n)\right)}{1 + (\omega\tau_n)^{2(1-\alpha_n)} + 2(\omega\tau_n)^{1-\alpha_n}\cos\left(\frac{\pi}{2}(1-\alpha_n)\right)}\Delta\varepsilon_n
\end{aligned} \tag{1.5}$$

These expressions for the dispersive nature of several biological tissues is explored in [2]. The 4-term Cole-Cole parameters are extracted for seventeen different types of tissue and are given in Table 1.2. For gray matter brain tissue, the resulting relative permittivity and conductivity are $\varepsilon_r \approx 263$, $\sigma \approx 0.327$ at 13.56 MHz, as seen in Figure 1.2.

Table 1.2: Curve fitting parameters used in the 4-term Cole-Cole model for seventeen biological tissues [2].

Tissue type	ε_∞	$\Delta\varepsilon_1$	τ_1 (ps)	α_1	$\Delta\varepsilon_2$	τ_2 (ns)	α_2	$\Delta\varepsilon_3$	τ_3 (μs)	α_3	$\Delta\varepsilon_4$	τ_4 (ms)	α_4	σ
Blood	4.0	56.0	8.38	0.1	5200	132.63	0.10	0.0	0.00	0.0	0.0	0.000	0.00	0.7000
Bone (cancellous)	2.5	18.0	13.26	0.22	300	79.58	0.25	2.00E+04	159.15	0.2	2.00E+07	15.915	0.00	0.0700
Bone (cortical)	2.5	10.0	13.26	0.2	180	79.58	0.20	5.00E+03	159.15	0.2	1.00E+05	15.915	0.00	0.0200
Brain (grey matter)	4.0	45.0	7.96	0.1	400	15.92	0.15	2.00E+05	106.10	0.2	4.00E+07	5.305	0.00	0.0200
Brain (white matter)	4.0	32.0	7.96	0.1	100	7.96	0.10	4.00E+04	53.05	0.3	3.50E+07	7.958	0.02	0.0200
Fat (infiltrated)	2.5	9.0	7.96	0.2	35	15.92	0.10	3.30E+04	159.15	0.1	1.00E+07	15.915	0.01	0.0350
Fat (not infiltrated)	2.5	3.0	7.96	0.2	15	15.92	0.10	3.30E+04	159.15	0.1	1.00E+07	7.958	0.01	0.0100
Heart	4.0	50.0	7.96	0.1	1200	159.15	0.05	4.50E+05	72.34	0.2	2.50E+07	4.547	0.00	0.0500
Kidney	4.0	47.0	7.96	0.1	3500	198.94	0.22	2.50E+05	79.58	0.2	3.00E+07	4.547	0.00	0.0500
Lens cortex	4.0	42.0	7.96	0.1	1500	79.58	0.10	2.00E+05	159.15	0.1	4.00E+07	15.915	0.00	0.3000
Liver	4.0	39.0	8.84	0.1	6000	530.52	0.20	5.00E+04	22.74	0.2	3.00E+07	15.915	0.05	0.0200
Lung (inflated)	2.5	18.0	7.96	0.1	500	63.66	0.10	2.50E+05	159.15	0.2	4.00E+07	7.958	0.00	0.0300
Muscle	4.0	50.0	7.23	0.1	7000	353.68	0.10	1.20E+06	318.31	0.1	2.50E+07	2.274	0.00	0.2000
Skin (dry)	4.0	32.0	7.23	0	1100	32.48	0.20	0.0	0.00	0.0	0.00E+00	0.000	0.00	0.0002
Skin (wet)	4.0	39.0	7.96	0.1	280	79.58	0.00	3.00E+04	1.59	0.2	3.00E+04	1.592	0.20	0.0004
Spleen	4.0	48.0	7.96	0.1	2500	63.66	0.15	2.00E+05	265.26	0.3	5.00E+07	6.366	0.00	0.0300
Tendon	4.0	42.0	12.24	0.1	60	6.37	0.10	6.00E+04	318.31	0.2	2.00E+07	1.326	0.00	0.2500

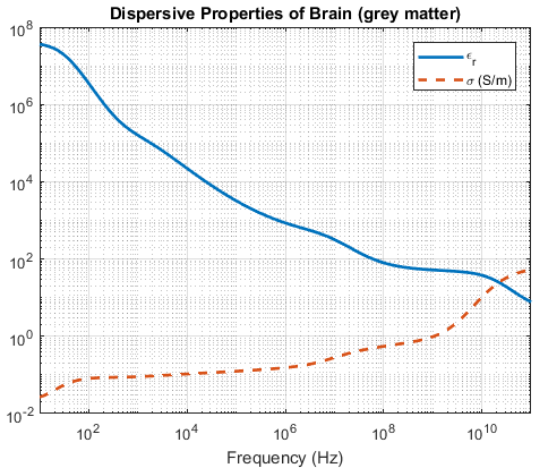

Figure 1.2: Relative permittivity and effective conductivity of grey matter using the 4-term Cole-Cole model parameters given in [2] from 10 Hz to 100 GHz.

1.1.4 Specific Absorption Rate

The specific absorption rate (SAR) is a metric defined to keep track of the amount of electromagnetic energy absorbed into a biological medium. Specifically, it is defined

as the time rate of change of electromagnetic energy per unit of biological mass. An expression used to compute SAR is given as (1.7) and is typically expressed in W/kg or mW/g [16].

$$SAR \equiv \frac{\text{Average Power Absorbed by the Volume}}{\text{Total Mass of the Volume}} \tag{1.6}$$

For a uniform planewave incident through a volume V, the average power absorbed by the volume may be determined by a phasor form of Poynting's theorem. The specific absorption rate is then computed with (1.7).

$$SAR = \frac{\int_v \mathbf{J}^* \cdot \mathbf{E} dV}{\int_v \rho dV} \tag{1.7}$$

In order to determine the expression for current density, the complex permittivity is inserted into Ampere's law as shown in (1.8).

$$\begin{aligned} \nabla \times \mathbf{H}^* &= -j\omega\hat{\varepsilon}^*(\omega)\mathbf{E}^* \qquad (1.8)\\ &= -j\omega\left(\varepsilon'(\omega) + j\varepsilon''(\omega)\right)\mathbf{E}^* \\ &= -j\omega\varepsilon'(\omega)\mathbf{E}^* + \omega\varepsilon''(\omega)\mathbf{E}^* \\ &= -j\omega\varepsilon'(\omega)\mathbf{E}^* + \mathbf{J}^* \\ \mathbf{J}^* &= \omega\varepsilon''(\omega)\mathbf{E}^* \qquad (1.9) \end{aligned}$$

The fields produced by a constant current I_0 in a circular loop of radius a at a distance r from the origin are given by (1.10) – (1.11).

$$\mathbf{E} = -\eta\frac{(\gamma a)^2 I_0 \sin\theta}{4r}\left[1 + \frac{1}{\gamma r}\right]e^{-\gamma r}\hat{\phi} \tag{1.10}$$

$$\mathbf{H} = \frac{\gamma a^2 I_0 \cos\theta}{2r^2}\left[1 + \frac{1}{\gamma r}\right]e^{-\gamma r}\hat{r} + \frac{(\gamma a)^2 I_0 \sin\theta}{4r}\left[1 + \frac{1}{\gamma r} + \frac{1}{(\gamma r)^2}\right]e^{-\gamma r}\hat{\phi} \tag{1.11}$$

These expressions have been adapted from [17] where the propagation constant has been replaced by its lossy version, $jk \rightarrow \gamma = \alpha + j\beta$. For this application, the frequency is too low for there to be significant propagation defined by the imaginary part of the propagation constant. Instead, γ is dominated by the attenuation constant α. In general, both the real and imaginary parts of the propagation constant are dependent on the complex permittivity.

The attenuation constant may be determined by expanding the complex propagation constant using the lossy dielectric expression, as shown in (1.12)

$$\begin{aligned}
\gamma &= \sqrt{j\omega\mu(\sigma + j\omega\varepsilon_r\varepsilon_0)} \\
&= \sqrt{j\omega^2\mu\varepsilon(1 - j\tan\delta)} \\
&= \sqrt{w^2\mu\varepsilon\sec\delta e^{-j\delta}e^{j\pi/2}} \\
&= \omega\sqrt{\mu\varepsilon\sec\delta}\left[\cos\left(\frac{\pi}{4} - \delta\right) + j\sin\left(\frac{\pi}{4} - \delta\right)\right]
\end{aligned} \tag{1.12}$$

where $\delta = \mathrm{Tan}^{-1}\left(\frac{\sigma}{\omega\varepsilon}\right) = -\mathrm{Tan}^{-1}\left(\frac{\mathrm{Im}\{\hat{\varepsilon}\}}{\mathrm{Re}\{\hat{\varepsilon}\}}\right)$. Hence, $\alpha = \mathrm{Re}\{\gamma\}$.

Prior work on specific absorption rate in the human body due to electromagnetic radiation from near-field communication (NFC) devices operating at 13.56 MHz suggests that the human body is not strongly affected by the radiation [18]. The maximum SAR obtained in this study was 11.2 mW/kg – well below the FCC limit of 1.6 W/kg.

1.1.5 Q-Factor of an RLC Circuit

The quality factor of an RLC circuit is defined as the ratio between stored energy and dissipated power per cycle. This is described mathematically by (1.13).

$$Q \equiv \frac{E_s}{\left(\frac{P}{\omega}\right)} \tag{1.13}$$

The energy stored in LC circuit given by (1.14), stating that half part of the energy is stored in the capacitor's electric field and the other part stored in the inductor's magnetic field.

$$E_s = \frac{1}{2}LI_L^2 + \frac{1}{2}CV_C^2 \tag{1.14}$$

At resonance, the energy stored by the inductor is equal to the energy stored by the capacitor. Therefore, the total stored energy can be can be written in either one of the two forms represented in (1.15), (1.16).

$$E_s = LI_L^2 \tag{1.15}$$

$$= CV_C^2 \tag{1.16}$$

For a series RLC circuit, the power loss may be computed using $P = I^2R$. Since the power loss is expressed using current, the expression for energy relating to current, (1.15), is used to find the quality factor of the series circuit (1.17).

$$Q_s = \frac{L_sI^2}{\left(\frac{I^2R_s}{\omega_0}\right)} = \frac{\omega_0 L_s}{R_s} = \frac{1}{\omega_0 R_s C_s} \tag{1.17}$$

Similarly, the power loss in a parallel RLC circuit may be computed using $P = \frac{V^2}{R}$. Since the power loss is expressed using voltage, the expression for energy relating to voltage, (1.16), is used to find the quality factor of the parallel circuit (1.18)

$$Q_p = \frac{C_pV^2}{\left(\frac{V^2}{R_p\omega_0}\right)} = \omega_0 R_p C_p = \frac{R_p}{\omega_0 L_p} \tag{1.18}$$

Another useful definition of the quality of an RLC circuit describes its relationship to the bandwidth and is given by (1.19). This expression emphasizes that in order to have high Q, the bandwidth must be small since they are inversely proportional to

one another.

$$Q \equiv \frac{\omega_0}{\Delta\omega} = \frac{f_0}{\Delta f} = \frac{f_0}{BW} \tag{1.19}$$

1.1.5.1 Series to Parallel Transformations

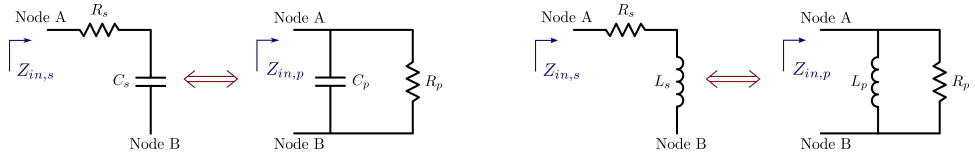

(a) Series to parallel transformation of an RC circuit.

(b) Series to parallel transformation of an RL circuit.

Figure 1.3: Description of equivalent series and parallel circuits. The equivalence is only valid over a narrow bandwidth determined by the Q-factor.

Sometimes it is necessary to transform a circuit from series to parallel, or vice versa, in order to simplify some analysis. The math governing this transformation is made straight forward when quality factor is utilized. The input impedance of a series RC circuit is given by (1.20). The input impedance of a parallel RC circuit is given by (1.21). It is clear from the two expressions that they are not equal for all frequencies, however they may be equal at a single frequency. Thus, this series to parallel transformation is a narrowband solution.

$$Z_{inS} = R_s - j\frac{1}{\omega C_s} \tag{1.20}$$

$$Z_{inP} = \frac{R_p}{1+\omega^2 R_p^2 C_p^2} - j\frac{\omega R_p^2 C_p}{1+\omega^2 R_p^2 C_p^2} \tag{1.21}$$

At resonance ($\omega = \omega_0$), $Z_{inS} = Z_{inP}$ and $Q_s = Q_p$ for the transformation to be valid. By equating real parts of (1.20) and (1.21), (1.22) is obtained. By equating

(1.17) to (1.18) and substituting (1.22), (1.23) is obtained.

$$R_p = (1 + Q^2)R_s \tag{1.22}$$

$$C_p = \frac{Q^2}{1 + Q^2}C_s \tag{1.23}$$

A similar analysis may be performed on RL circuits. However, note that at resonance $\omega_0 L = \frac{1}{\omega_0 C}$. Therefore, the solution for inductance is the dual of the solution for capacitance and is obtained by inverting (1.23) and replacing C's with L's. The result is (1.24).

$$L_p = \frac{1 + Q^2}{Q^2}L_s \tag{1.24}$$

Note that the resistance transformation remains as (1.22). However, it may also be rewritten as (1.25).

$$Q = \sqrt{\frac{R_p}{R_s} - 1} \tag{1.25}$$

1.1.5.2 Closed Form Solution for a Common Equation

In a few cases, it will be necessary to solve an equation of the form (1.26).

$$Q = \sqrt{ax - 1} + \sqrt{bx - 1} \tag{1.26}$$

The equation is quadratic in x and may rewritten as (1.27).

$$(b - a)^2x^2 - 2(b + a)Q^2x + Q^2(Q^2 + 4) = 0 \tag{1.27}$$

The solution (removing extraneous solution) is (1.28). If purely real solutions are desired, the equation is constrained under (1.29).

$$x = \frac{Q^2(b+a) - 2Q\sqrt{Q^2ab - (b-a)^2}}{(b-a)^2} \tag{1.28}$$

$$Q^2ab \geq (b-a)^2 \tag{1.29}$$

1.1.5.3 Methods of Impedance Matching

As an example, consider matching 0.1 Ω to 50 Ω at 13.56 MHz.

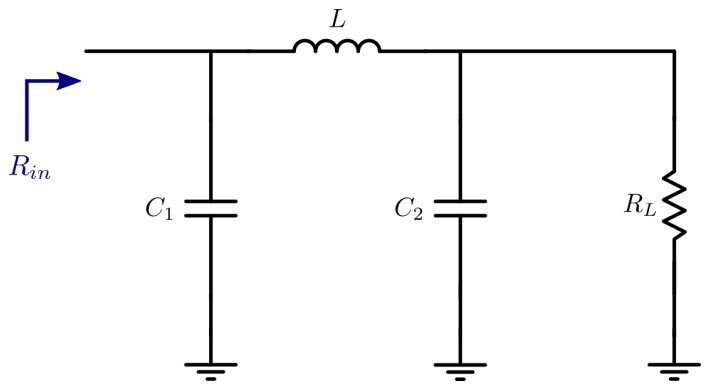

Figure 1.4: Π-network impedance matching topology.

Suppose a Π shaped topology is used to realize the matching network as shown in Figure 1.4. In order to match 0.1 Ω to 50 Ω, the quality factor is constrained to a minimum value based on (1.29) and given by (1.30).

$$\begin{aligned} Q_{\min} &= \frac{|R_L - R_{in}|}{\sqrt{R_{in}R_L}} \\ &\approx 22.32 \end{aligned} \tag{1.30}$$

Therefore the Q is chosen to be 45. In order to find the total network Q, the network is converted to a purely series network. Therefore the two parallel RC networks are converted to their series equivalents. The total Q is then found by summing the Q of each section given by (1.25). The total Q is given by (1.31). Solving this for the intermediate resistance gives (1.32).

$$Q_{\text{Tot}} = \sqrt{\frac{R_{in}}{R_I} - 1} + \sqrt{\frac{R_L}{R_I} - 1} \tag{1.31}$$

$$R_I = \frac{(R_L - R_{in})^2}{Q^2(R_L + R_{in}) - 2Q\sqrt{Q^2 R_{in} R_L - (R_L - R_{in})^2}} \tag{1.32}$$

$$\approx 0.0266\ \Omega$$

Therefore, the Q of each section is:

$$Q_1 = \sqrt{\frac{R_{in}}{R_I} - 1} \approx 1.66$$

$$Q_2 = \sqrt{\frac{R_L}{R_I} - 1} \approx 43.34$$

$$\text{and } Q_1 + Q_2 = 45$$

Therefore the capacitor values are related to the respective quality factor using (1.18). The inductor value is related to the total network Q using (1.17).

$$C_1 = \frac{Q_1}{\omega_0 R_{in}} \approx 194.94\ \text{nF}$$

$$C_2 = \frac{Q_2}{\omega_0 R_L} \approx 10.17\ \text{nF}$$

$$L = \frac{Q R_I}{\omega_0} \approx 14.05\ \text{nH}$$

Alternatively, a T-shaped network could be utilized to match 0.1 Ω to 50 Ω, as shown in Figure 1.5. The minimum quality factor is still given by (1.30). Therefore, Q is again chosen to be 45. In order to find the total network Q, it may be converted to a purely parallel network by converting the two series R-L networks to their parallel equivalents. The total Q is then found by summing the Q of each section. This is shown as (1.25). The total Q is given by (1.33). Solving this for the intermediate

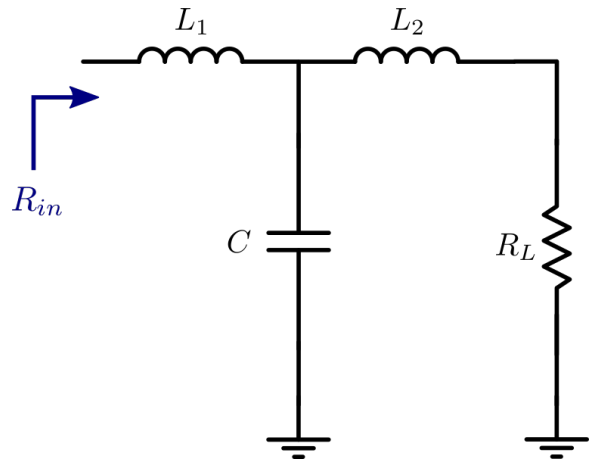

Figure 1.5: T-network impedance matching topology.

resistance gives (1.34).

$$Q_{\text{Tot}} = \sqrt{\frac{R_I}{R_{in}} - 1} + \sqrt{\frac{R_I}{R_L} - 1} \tag{1.33}$$

$$R_I = \frac{Q^2\left(\frac{1}{R_L} + \frac{1}{R_{in}}\right) - 2Q\sqrt{\frac{Q^2}{R_{in}R_L} - \left(\frac{1}{R_L} - \frac{1}{R_{in}}\right)^2}}{\left(\frac{1}{R_L} - \frac{1}{R_{in}}\right)^2} \tag{1.34}$$

$$\approx 187.93\ \Omega$$

Therefore the Q of each section is:

$$Q_1 = \sqrt{\frac{R_I}{R_{in}} - 1} \approx 43.3391$$

$$Q_2 = \sqrt{\frac{R_I}{R_L} - 1} \approx 1.6609$$

$$\text{and } Q_1 + Q_2 = 45$$

Therefore the inductor values are related to the respective quality factor using (1.17). The capacitor value is related to the total network Q using (1.18).

$$L_1 = \frac{Q_1 R_{in}}{\omega_0} \approx 50.87 \text{ nH}$$
$$L_2 = \frac{Q_2 R_L}{\omega_0} \approx 974.7 \text{ nH}$$
$$C = \frac{Q}{\omega_0 R_I} \approx 2.8105 \text{ nF}$$

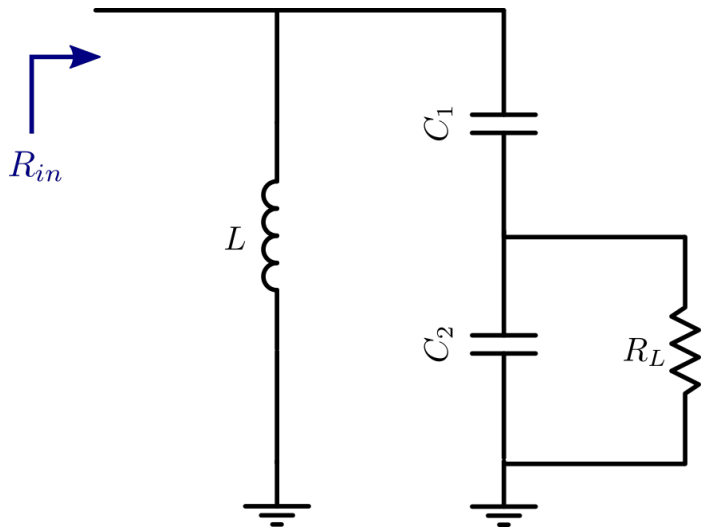

Figure 1.6: Impedance matching tapped capacitor topology.

Alternatively, a tapped capacitor network may be used as observed in Figure 1.6. The total Q of the network may be expressed using (1.18). Therefore, the inductance may be found as (1.35).

$$L = \frac{R_{in}}{\omega_0 Q} \tag{1.35}$$

Converting the R_{in}-L sub-network into its series equivalent gives:

$$R_{ins} = \frac{R_{in}}{1+Q^2}$$
$$L_s = \frac{Q^2}{1+Q^2} L$$

Similarly, the R_L-L sub-network is converted into its series equivalent:

$$R_{Ls} = \frac{R_L}{1+Q_2^2}$$
$$C_{2s} = \frac{1+Q_2^2}{Q_2^2} C_2$$

At resonance, the input resistance is simply R_{Ls}. Therefore, this must be matched to R_{ins}.

$$\frac{R_{in}}{1+Q^2} = \frac{R_L}{1+Q_2^2}$$
$$\rightarrow Q_2 = \sqrt{\frac{R_L}{R_{in}}(1+Q^2) - 1}$$

Equation(1.18) may also be used to find $Q_2 = \omega_0 R_L C_2$. Therefore, the value of C_2 is given by (1.36).

$$C_2 = \frac{\sqrt{\frac{R_L}{R_{in}}(1+Q^2) - 1}}{\omega_0 R_L} \tag{1.36}$$

The overall Q of the series equivalent circuit may be described with (1.17). Thus the value of C_1 is given by (1.37).

$$
\begin{aligned}
Q &= \frac{1}{\omega_0 R_{Ls}\left(\frac{C_1 C_{2s}}{C_1+C_{2s}}\right)} \\
&= \frac{C_1 + \left(\frac{1+Q_2^2}{Q_2^2}\right) C_2}{\omega_0 R_{Ls} C_1 \left(\frac{1+Q_2^2}{Q_2^2}\right) C_2} \\
&= \frac{Q_2^2 C_1 + (1+Q_2^2) C_2}{\omega_0 \left(\frac{R_L}{1+Q_2^2}\right) C_1 (1+Q_2^2) C_2} \\
\rightarrow C_1 &= \frac{(1+Q_2^2) C_2}{Q_2 (Q - Q_2)}
\end{aligned} \tag{1.37}
$$

For C_1 to be meaningful, the total Q must be greater than Q_2 (denominator of (1.37)), so (1.38) must hold.

$$
\begin{aligned}
Q^2 &> \frac{R_L}{R_{in}}(1+Q^2) - 1 \\
0 &> (1+Q^2)\left(\frac{R_L}{R_{in}} - 1\right) \\
\rightarrow R_L &< R_{in}
\end{aligned} \tag{1.38}
$$

For C_2 to be meaningful, it must be a positive real number (discriminant of (1.36)), so (1.39) must hold.

$$
R_L \geq \frac{R_{in}}{1+Q^2} \tag{1.39}
$$

Lumping these two constraints gives (1.40).

$$
1 < \frac{R_{in}}{R_L} \leq 1 + Q^2 \tag{1.40}
$$

For the specific values given in the example, in order for the inequality to hold true, $R_{in} = 50\ \Omega$ and $R_L = 0.1\ \Omega$. In other words, it must be driven from the tapped side,

and loaded on the shunt inductor side.

Therefore the component values are obtained from (1.35), (1.36), and (1.37).

$$L \approx 13.041 \text{ nH}$$

$$C_1 \approx 205.05 \text{ nF}$$

$$C_2 \approx 10.995 \text{ nF}$$

1.2 A Review of Existing Wireless Power Transfer Systems

The notion of transfering power wirelessly is not a new one and harkens back to the early 1900's with Nikola Tesla's first inventions. However, more than 100 years later, there is more work to be done in this area. In the literature, wireless power transfer systems have been used from 23 kHz [19] to 200 GHz [20], for applications ranging from powering a vehicle on the kilowatt scale, to harvesting energy in implantable electronics in the nanowatt range. It is important to review work that has already been completed by others, in order to begin this research in a direction that makes sense for the desired application.

A survey of work in the field of wireless power transfer, especially as it relates to biomedical applications, has been compiled here for reference. These references serve as a basis on which to build the fundamentals of the underlying wireless power transfer goals of this project. A brief overview of each method is presented with more detail being provided where relevant to the project. Similar surveys have been performed by others [21], [22], [23], [24], [25] and are drawn from as well.

The primary metrics of interest to this research are powering distance, efficiency and secondary coil size, so these will be explicitly mentioned where possible.

1.2.1 Inductive Coupling

Most methods of WPT to date employ inductive coupling. Inductive coupling is often referred to in the literature as "magnetic resonance," in an effort to describe

the physical phenomenon responsible for power transfer. Namely the Faraday-Lenz Law (1.41), which states that a time-varying magnetic flux generates a voltage in the circuit through which the flux was measured.

$$V_{EMF} = -\frac{\partial \Phi_B}{\partial t} \tag{1.41}$$

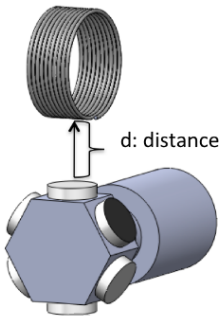

Figure 1.7: The drawing of a DC motor with permanent magnets for induction of voltage into the coil at distance d [3].

In order to produce this time varying magnetic flux, permanent magnets may be attached to a motor and placed in the vicinity of a wire loop as depicted in Figure 1.7. As the magnets rotate, their fields periodically enter and exit the loop, thus generating a voltage [3]. A system has been designed based on this method, and suggests the ability to transfer 10 W to a 3.4 cm coil of 600 turns at a 1 cm powering distance. However, the received power is not rectified or delivered to any load. It is simply the power dissipated by the inductor's equivalent resistance due to an induced open circuit voltage. Since it is an open circuit voltage, the induced current is zero, resulting in 0 W delivered power.

Although the rotating magnet method is perfectly valid, it is not the typical way time varying magnetic flux is generated. Ampere's Law states that a magnetic field is related to the total current that it encompasses (1.42). In the event that this magnetic field intersects a nearby second circuit, a time varying voltage is produced across that circuit.

$$\oint_{\gamma} \mathbf{H} \cdot d\boldsymbol{\ell} = \iint_{S} \left(\mathbf{J} + \frac{\partial \mathbf{D}}{\partial t} \right) \cdot d\mathbf{s} \tag{1.42}$$

A circuit in which a time-varying current produces a magnetic field (by Ampere's Law) which penetrates a second circuit, thereby inducing a voltage (by Faraday's Law) is said to be inductively coupled to that same circuit. This is most commonly seen in power transformers where two wires are wrapped around a common magnetic core. Inductively coupled coils may also be viewed as a transformer, where the core is air in place of the magnetic medium. The key difference between a traditional transformer and a pair of inductively coupled coils is that the coils are exchanging energy at a common resonant frequency, whereas a transformer is broadband.

There are two primary methods of analyzing inductively coupled circuits: through circuit theory using an equivalent circuit model and by examining analyzing the energy transferred between two resonating objects, which is known as Coupled Mode Theory (CMT). It may be shown that in the case of coils that are weakly coupled and are low in loss, circuit analysis and CMT produce almost identical results yet the CMT approach reduces the differential equation order [26]. However, when the coils are of low quality factor and are strongly coupled, the results obtained by Coupled Mode Theory are inaccurate.

A fundamental paper on WPT that employs CMT was presented by Kurs *et al.* A system consisting of four coils was designed that transfers power at 10 MHz over a distance of 2 meters with 40% efficiency [27]. The resonators were copper helical coils of 30 cm radius, 3 mm wire radius, and 5.25 turns.

It has been demonstrated that inductive coupling is much more efficient at resonance than its non-radiating counterpart. 5 Watts of power was successfully transmitted wirelessly over a distance of 2 cm with efficiency of 30% [4], as depicted in Figure 1.8. Therefore, it is seen that wireless power transfer is feasible, although it is desired to have greater than 30% efficiency.

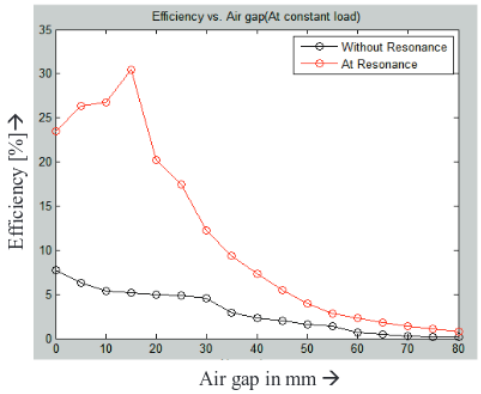

Figure 1.8: Experimental results of efficiency vs. distance from [4]

Further research suggests the ability to increase efficiency by simply adding an impedance matching network on the primary coil side [5]. The results results obtained by this method may be observed in Figure 1.9. In other work, the impedance matching network is added on the secondary side with similar results[28].

It is worth mentioning at this point that there are two commonly used metrics for wireless power transfer efficiency. The first (most common) is the ratio of power consumed by the load to the total power supplied by the source (1.43). The other is the square of the magnitude of transmission parameter S_{21} (1.44).

$$\eta_p = \frac{P_{out}}{P_{in}} \tag{1.43}$$

$$\eta_s = |S_{21}|^2 \tag{1.44}$$

Although it is not obvious, these two definitions of efficiency are not equivalent. Therefore, the subscripts "p" and "s" will be used in this work in order to avoid ambiguity. The relationship between the two definitions is given by (1.45) [29],

$$\eta_p = \frac{|S_{21}|^2 \left(1 - |\Gamma_L|^2\right)}{\left(1 - |1 - |\Gamma_L|^2|^2\right) |1 - S_{22}\Gamma_L|^2} \tag{1.45}$$

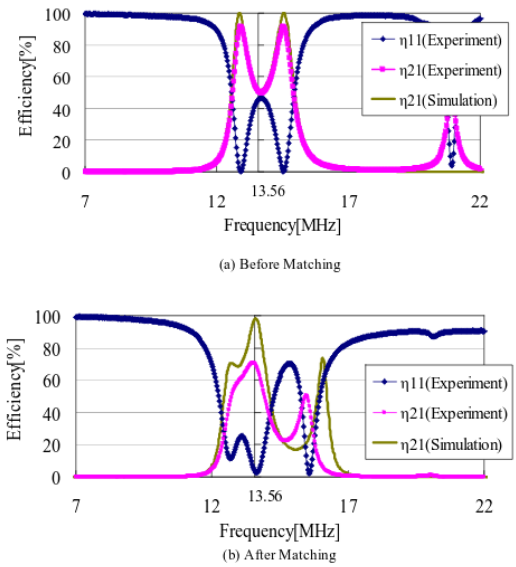

Figure 1.9: Experimental results of efficiency vs. frequency from [5]. Note that the efficiency at 13.56 MHz increases from about 50% to about 70%.

where Γ_L is the reflection coefficient at the load boundary, defined in a common form by (1.46).

$$\Gamma_L = \frac{Z_L - Z_0}{Z_L + Z_0} \tag{1.46}$$

In other work, a lot of focus is placed on delivering wireless power at maximum output power, even at the expense of lower efficiency. For systems in which the input power is allowed to vary, this approach is misguided.

From maximum power transfer theory, it is tempting to make the sweeping statement that maximum output power occurs when $R_L = R_s$ regardless of the circumstances applicable to the desired application. While this statement is true, it is important to understand the conditions upon which it is true. Consider the two resistive dividers shown in Figure 1.10 consisting of a load resistor R_L driven by a source with resistance R_s.

The current through the first circuit is $\frac{2\text{ V}}{1\ \Omega + 1\ \Omega} = 1$ A. The current through the second circuit is $\frac{6\text{ V}}{1\ \Omega + 3\ \Omega} = 1.5$ A. The output power of the first circuit is $(1\text{ A})^2 1\ \Omega = 1$

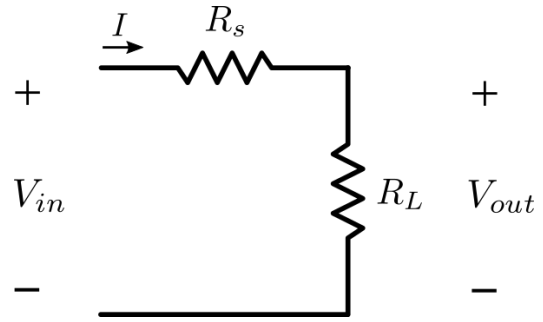

Figure 1.10: A resistive divider used to illustrate the importance of high efficiency over maximum power output.

W and maximum power transfer is satisfied because $R_L = R_s$. The output power of the second circuit is $(1.5\text{ A})^2 3\ \Omega = 6.75$ W, but $R_L \neq R_s$ so maximum power transfer is not satisfied, yet the output power is higher than in the case where maximum power transfer is satisfied! Obviously, the reason for this is the increase in supply voltage.

The reason this is being discussed is that there are published works that suggest operating at a lower efficiency simply because it is somehow desirable to operate at maximum power transfer [19]. In this work, it is suggested that efficiency should be the target. If the output power is too low at this efficiency, simply increase the input power. A summary of maximum power transfer is provided in Table 1.3.

Table 1.3: Summary of Power Transfer Cases for a Resistive Divider

Case ID	I	P_{in}	P_{out}	$\eta_p = \frac{R_L}{R_s+R_L}$
$\mathbf{A}_{\ R_L=0}$	V_s/R_s	I^2R_s	0	0.0
$\mathbf{B}_{R_L=R_s}$	$V_s/(2R)$	$2I^2R$	I^2R	0.5
$\mathbf{C}_{R_L\to\infty}$	$\to 0$	$\to 0$	$\to 0$	$\to 1$
$\mathbf{D}_{\ R_s=0}$	V_s/R_L	I^2R_L	I^2R_L	1.0

The system efficiency for a resonating wireless power transfer system with secondary side matching network has an efficiency given by (1.47) [30].

$$\eta_p = \frac{Q_{2L}}{Q_L} \frac{k_{12}^2 Q_1 Q_{2L}}{1 + k_{12}^2 Q_1 Q_{2L}} \tag{1.47}$$

From (1.47), it is clear that efficiency is proportional to the product of coupling coefficient and quality factor, referred to as the kQ product [31]. Therefore, optimization of these systems involves maximizing the coupling coefficient and maximizing the quality factor. Coupling coefficient may be increased in two ways: by manipulating the coil geometries in order to increase mutual inductance and by decreasing the distance between the coils. The quality factor is the ratio between reactance to equivalent series resistance of the coil (1.48). Therefore increasing inductance (more coil turns), increasing operating frequency, and decreasing losses, all help power efficiency. However, many of these parameters are in tension with each other, so design tradeoffs must be made.

$$Q = \frac{\omega L}{R_s} \tag{1.48}$$

Similarly, an expression for power transfer efficiency has been derived for a system containing an arbitrary number of coils [32]. The resulting expression is given by (1.49)

$$\eta_{m-coil} = \frac{Q_{mL}}{Q_L} \prod_{j=1}^{m-1} \frac{k_{j,j+1}^2 Q_j Q_{(j+1)L}}{1 + k_{j,j+1}^2 Q_j Q_{(j+1)L}} \tag{1.49}$$

where

$$Q_j = \frac{\omega L_j}{R_j}$$
$$Q_L = \frac{R_L}{\omega L_m}$$
$$Q_{jL} = \frac{Q_j Q_L}{Q_j + Q_L}$$
$$Q_{mL} = \frac{\omega L_m}{R_m + R_L}$$

Although the efficiency may be improved by increasing coupling and using higher Q-factor resonators, there is more that can be done. Further investigation of the equation for efficiency reveals that there is a global maximum relative to loading impedance. Therefore, an optimal loading impedance exists and can be attained by transforming the actual load to this optimal value [33].

Wireless power transfer has been used to charge cellular devices, as shown possible in [34]. A commercial version of this has been developed by various companies and standardized under the marketing term "Qi" charging by the Wireless Power Consortium.

A high power wireless power transfer system was designed to transmit 220 Watts over a distance of 30 cm at 96% efficiency [35].

Wireless power transfer systems composed of three inductive coils have also been theorized and implemented [36], [37]. Similar analysis has been theorized and constructed for systems of four coils [13], [38], [39].

A comparison of three types of inductively coupled systems was made in [40]. The three setups are: two mutually coupled inductors, the same coupled inductors with added capacitors for resonance, and a four coil system where the inner coils are resonating due to their parasitic capacitances. It was discovered that the four coil system operates most efficiently – upwards of 90% at 30 cm.

If inductive coupling is used for WPT, it is critical to know the self inductance of each coil, as well as the mutual inductances between each coil. This is not, in general, a trivial task. A numerical technique to solving Neumann's formula for mutual inductance of arbitrarily shaped coil geometries is discussed in [41]. Methods for calculating self and mutual inductance has been studied at great length over the years. There are many formulas and tables that describe these quantities for special case scenarios (such as single-turn, circular loops) [42], [43]. See the appendix for more details on calculating coil parameters.

One restriction on power transfer efficiency is the quality factor of the coils used. Quality factor is correlated with losses such that the higher Q implies lower loss. Losses increase with increasing frequency due to the skin effect. When a conductor carries alternating current, it produces a circulating magnetic field that surrounds the conductor. This magnetic field in turn induces a current in the conductor in the opposite direction, effectively creating a much larger impedance than is seen at DC. This reverse induced current causes the overall current distribution to be nonuniform such that current tends to flow mostly on the conductor surface or "skin". This is particularly pronounced in PCB trace inductors since there is not a large volume of conductor in a trace. One method for mitigating the skin effect is to split a trace into multiple smaller traces that electrically connect at various points. This forces current to flow more evenly, reducing the skin effect and increasing the Q [44].

It has also been suggested that the use of ferrites could improve wireless power transfer efficiency [45]. This is due to the increased mutual inductance in the presence of the ferrite.

Relatively high efficiency has been reported for large distances. For example, 58% efficiency has been achieved at a powering distance of 1 meter in [46]. The operating frequency of the powering link was 5.5 MHz and each of the resonating coils were identical 7-turn square coils of side length 40 cm and wire radius 0.16 mm.

Physical size is an extreme limiting factor on implantable wireless power transfer systems. However, there is research that supports the possibility of implantable coils on the millimeter scale [47].

Inductive systems involving multiple receivers has also been theorized and described in the literature. Analysis is performed using matrices in order to account for the arbitrary number of receivers, but is otherwise the same as systems with one receiver [48]. Since many receivers may be oriented arbitrarily, the transmitter is designed to be omni-directional [49].

1.2.2 Capacitive Coupling

Another technique discussed in research literature involves capacitively coupled circuits [50]. In this concept, large parallel plates are placed in the near vicinity of each other such that an air-gap capacitor is formed. A resonant tank is formed by including series inductors on the primary side. The approach may be thought of as the dual of inductive coupling in which the coupling field is the electric field between the plates as opposed to the magnetic field through coils. For current state-of-the-art, range seems to be a heavy limiting factor. Power transfer distances were reported only to be 5 mm [51] and 1.2 cm [52] with 60% and 90% efficiency, respectively. The capacitve plates are also larger than inductive coupling coils would be for same efficiency at that powering distance.

The authors of [51] suggest that capacitive systems are better in comparison with inductive systems for applications where higher frequency is desired, large receiver size is acceptable, biosafety is a concern, moderate power transfer efficiency is acceptable, receiver deformation or misalignment is possible, and EM interference is a concern.

1.2.3 True Antennas for Power Transfer

In some cases, the resonator coils used in inductive coupling are referred to as antennas. However, they are electrically small, do not radiate well, and operate in the

near field which leads them to not be classified as antennas. In contrast, there has been research that employs true antennas for the purpose of power transfer. These circuits typically operate in the hundreds of megahertz to low gigahertz range.

An attempted generalization of wireless power transfer was explored from an antenna theory perspective in [53]. An effective impedance matrix was formulated for two identical electrically small antennas and the power transfer efficiency was computed and maximized using this impedance matrix. However, this formulation is stated to be valid only for distance greater than 0.1λ, due to assumption that only the TE_{10} and TM_{10} modes are present. Additionally, the analysis was performed under the assumption that the two antennas are the same. This theory could potentially be expanded to account for different transmitting and receiving antennas.

Another use of antenna theory for wireless power transmission for biomedical applications is presented in [54] with the goal of determining the optimal frequency at which antennas exchange energy through a dispersive dielectric medium. The optimal frequency is defined as the frequency at which the ratio between received power and power absorbed by biological tissue is maximized. This frequency is determined to be in the 1 – 10 GHz range for distances less than 1 cm in various types of biological tissue. The optimal frequency decreases as separation distance increases and is given by (1.50)

$$f_{opt} \approx \frac{1}{2\pi}\sqrt{\frac{c\sqrt{\epsilon_{r0}}}{d\tau\Delta\epsilon}} \tag{1.50}$$

where c is the speed of light in vacuum, d is the distance between the antennas, and $\epsilon,\ \tau$ are dielectric properties defined by the Debye relaxation model (1.51). The Debye model is a faster, less accurate version of the Cole-Cole model (1.3).

$$\varepsilon(\omega) = \varepsilon_{\infty} + \frac{\Delta\varepsilon}{1 + j\omega\tau} \tag{1.51}$$

A pair of folded helical dipoles was constructed to transmit and receive power at 195 MHz [55]. The powering distance was $\lambda/4 \approx 0.39$ m. The power transfer efficiency was measured to be 40%, approaching the theoretical bounds. Although the antennas are electrically small, they are still too large for implantable applications, measuring at approximately 10 cm $\times$ 10 cm.

A 2.45 GHz WPT system was designed using a transmitting horn antenna (30 cm $\times$ 25 cm $\times$ 61 cm) and a 3$\times$4 array of patch antennas (20 cm $\times$ 26 cm). Each patch in the array contains an RF-DC rectifier with a conversion efficiency of 46%. The system was physically fabricated and tested and found to be capable of charging an unmanned arial vehicle at a distance of 4 meters with about 0.4% efficiency [56].

Another 2.45 GHz system has been designed that transmits power over distances of 0.3 m to 4.0 m at an efficiency of 5.5% to 0.2% [57]. The receive antenna is a square patch with approximate dimensions 2.9 cm $\times$ 4.5 cm including the microstrip feed line.

A 4.3 GHz system has been designed that transmits power at an efficiency of 11.2% for single patch antenna and 19.9% for a 1$\times$4 patch array. The antenna dimensions were not specified, nor was powering distance. From the photographs, it appears that each patch is about 2.5 cm$\times$ 2.5 cm with a powering distance of about 15 cm [58]. Output DC power was measured for use in efficiency calculations. The measured output voltage was 2.1 V at 7.36 mA, or about 15 mW.

A neural monitoring implant system was designed to transmit wireless power at 915 MHz with $\lambda_e \approx 50$ mm at a distance of 15 mm. The system uses a 2cm $\times$ 2cm transmit antenna and a 2mm $\times$ 2mm receive loop antenna. A total of 140 μW was delivered to the implant that was designed to operate at low power [59].

An implantable wireless power receiver was designed that receives power at 39.86 MHz and transfers data at 2.45 GHz. Power transmission efficiency was measured at 47% [60].

A flexible antenna was designed to operate well in three different frequency ranges 402 – 405 MHz, 1.45 – 1.6 GHz, and 2.4 – 2.45 GHz [61].

1.2.4 Metamaterial Loading of Inductive Based Systems

Metamaterial loading of wireless power transfer systems has also been explored [7]. In [6], a slotted metal plate is inserted between the transmitting and receiving coils as depicted in Figure 1.11. The efficiency is dependent on the size and orientation of the slots. Unfortunately, the plate tends to reduce the efficiency since it shields the secondary from the primary. The efficiency without a plate is reported to be 90%, while the efficiency with an unslotted metal plate is just 0.1%. By introducing slots, the efficiency climbs to 66% with a slot gap of 0.1 mm and to 84% with a slot gap of 1 mm. In all cases, the efficiency with the plate is lower than the efficiency with no plate.

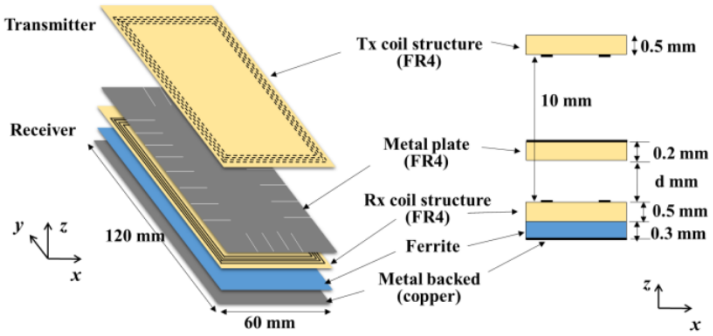

Figure 1.11: The diagram from [6] depicting the WPT system including the slotted plate.

Although the presence of the metal plate is not useful for increasing the efficiency, this work suggests that if implantable electronics are required to be enclosed behind some metal, the link efficiency may be improved by placing small slots in the metal.

In [7], a 3×3 array of spirals is inserted between two inductively coupled coils. The authors refer to this array as a matrix power repeater. Circuit model analysis is performed where the mutual inductance between each of the spirals is considered. The

system was physically constructed and measured. The dimensions of the array are 13 cm×13 cm×0.177 cm. The transmitter and receiver coils are identical spiral coils of 10 turns with inner radius of 3 cm and outer radius of 6 cm. The two coils were placed a distance of 5 cm apart for the experiment with the repeater in the center (2.5 cm away from each). Measurements show that the output power is increased by about 34% when the matrix is present versus absent. This implies that the effiency of the system is increased by the array, since the output power increased while the input power remained constant. The system may be observed in Figure 1.12.

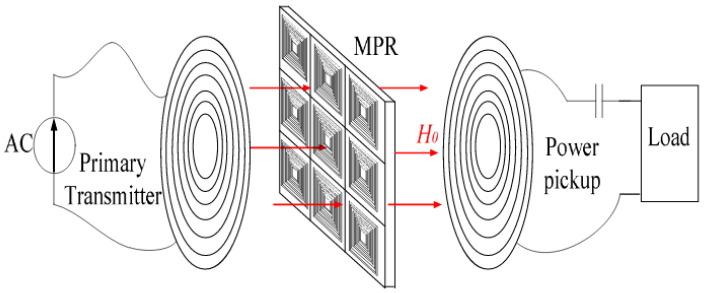

Figure 1.12: The diagram from [7] depicting a WPT system with improved efficiency due to the presence of an array of resonant printed spiral coils.

.

1.2.5 Cavity Resonator Transfer

An optogenetic implant was created in 2015 that wirelessly stimulated the brains of mice [8]. This implant employed a novel wireless powering system that has not been found in other literature and may be seen in Figure 1.13. The system consists of a cylindrical resonant cavity of 21 cm diameter by 15 cm height, with a surface lattice of 2.5 cm diameter hexagons. Up to 10 mW of power was delivered at 1.5 GHz to a 3-turn coil of 0.16 cm diameter.

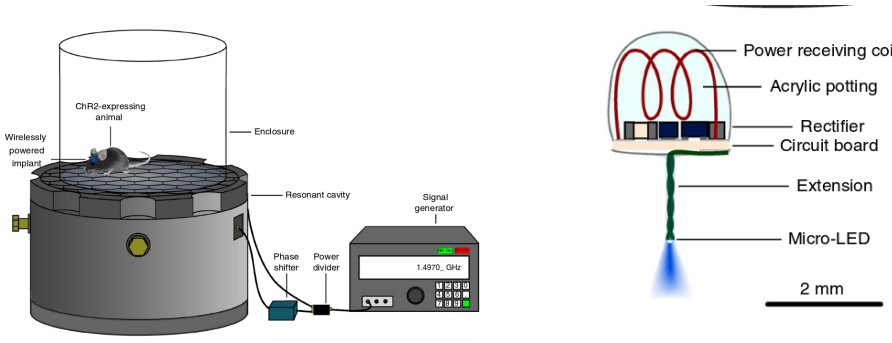

(a) The transmission system employing a cylindrical cavity resonator.

(b) The implantable receiver structure.

Figure 1.13: The novel resonant cavity based wireless power transmission system from [8].

1.3 A Review of Biomedical Implant Wireless Power Transfer Applications

There have been other systems in the literature that use wireless power transfer schemes to power biomedical implants. Much of the research presented here draws upon concepts and solutions published in previous work. A few noteworthy examples are listed here. In some cases, the circuits are theorized but not fabricated, while in others, a prototype is fabricated and measured.

The integrated circuit design of retinal and neural implants have been discussed in [62] and [9], respectively. In each, a prototype was fabricated and tested for their specific purposes. In [62], considerations for designing on-chip, analog biomedical circuits is discussed.

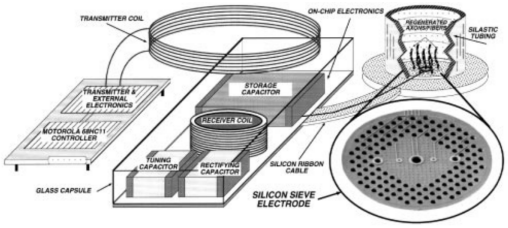

Figure 1.14: The system diagram depicting open-loop wireless power delivery to a neural implant [9].

The neural data acquisition system discussed in [9] may be observed in Figure 1.14.

The implant was designed to record neural signals, but the authors state that the circuits may be used in other types of implants provided an appropriate electrode is used. Power was transferred wirelessly to the implant by inductive coupling at 2 MHz. The maximum powering distance was reported to be 0.6 cm. The system is open loop – using no feedback to control power delivery. No mention is made of powering efficiency.

A similar system is designed that transferred power over a distance of 2.5 cm [63]. An additional accomplishment of this work was reducing the data packet error rate from 1.68×10^{-3} to 3×10^{-5} at a data rate of 10 kbps. The chip successfully recorded EEG signals from 4-channels when the device was implanted in the brain of a rat.

Another similar system is presented in [64]. Much more detail is given regarding the design of the complete system. The authors include considerations of SAR, design of multi-turn printed spiral coils, optimal loading impedance transformation network, and transmitter design.

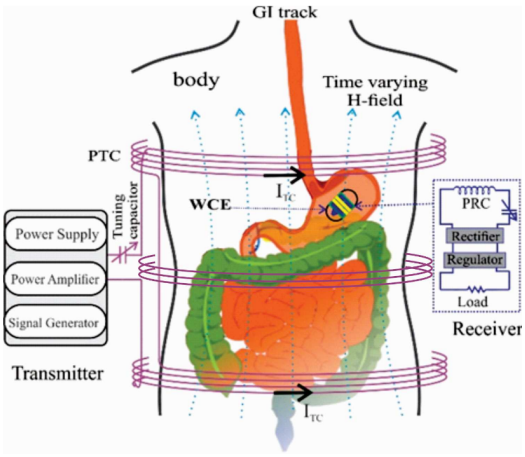

Figure 1.15: The power transmission scheme for endoscopy applications consisting of a wearable vest and 3-axis receiver [10].

Yet another system is designed similar to the previous, where the receiver is designed to be an endoscopy device [10]. This link also uses inductive coupling, this time with three driving coils that are worn like a vest by the human patient, depicted in Figure 1.15. Transmitters consisting of two, three, and four coils were compared and it was

determined that three coils produced highest power transfer efficiency. An interesting receiver coil architecture was also implemented consisting of three coils oriented perpendicularly to each other such that their area normal vectors aligned with the three coordinate axes, in order to maximize received power regardless of orientation of the endoscope. The power received by each of the three coils are rectified separately and then combined. The resulting system achieves 8.2% efficiency while delivering 750 mW.

Typically, a wireless power transfer system is designed to operate efficiently at a fixed powering distance (directly correlated with coupling coefficient) and fixed load resistance. Hence, deviations from the designed conditions lead to non-optimal power transfer. Since coupling decreases rapidly with distance, "non-optimal" can easily mean "not usable". More recently, work has been done to develop a system that dynamically adjusts to meet these adaptions to maintain efficiency across a variety of conditions. This maximum efficiency point tracking (MEPT) system accomplishes its goal by dynamically changing the load impedance and input voltage using DC-DC converters in both the transmitter and receiver [65].

Another similar system employs a closed-loop design to account for variations in rectified voltage over time is implemented in [66]. When the rectified voltage rises above a certain reference voltage, a switch is triggered that shorts the input to the rectifier. Since the rectifier is shorted, it cannot operate and the output voltage begins to drop. After a specific delay time, the switch releases and the circuit continues operating normally. While this method is effective at protecting the subsequent circuits from over-voltage, it is does nothing in the event of an under-voltage.

A large amount of research regarding the current state of the art biomedically implantable systems has been reviewed and briefly presented here for reference. Based on this, resonant inductive coupling is chosen as the wireless power transfer scheme to be implemented since it has the highest score when compared against other researched

technologies as apparent in Table 1.4.

Table 1.4: The decision matrix used to determine the method of wireless power delivery in this work.

Type	**Bio-Compatibility** $\alpha_1 = 0.3$	**Implant Size** $\alpha_2 = 0.25$	**Efficiency** $\alpha_3 = 0.15$	**Range** $\alpha_4 = 0.15$	**Power Capability** $\alpha_5 = 0.1$	**Existing Systems** $\alpha_6 = 0.05$	**Total**
Inductive Coupling	3	4	4	4	5	4	0.76
Far-Field Antennas	4	5	1	3	1	2	0.65
Resonant Cavity	3	5	1	3	2	2	0.61
Rotating Magnet	4	2	3	3	2	2	0.58
Mid-Field Antennas	3	5	1	2	1	2	0.56
Ultrasonic	1	4	4	3	3	2	0.55
Capacitive Coupling	3	1	3	1	4	1	0.44

1.3.1 Review of an Influential Paper

While researching previous work in related areas, one paper stuck out due to its similarities to this work. In the paper of interest, a fully integrated wireless power transfer system was developed for a biomedical implant for retinal prothesis [11]. Thus, reviewing this paper is a convenient starting point with which to discuss the current work.

1.3.2 Motivation

Wireless power transfer for biomedical applications has been studied in many other works. In most cases, the transmission distance is fixed, and the circuitry does not have multiple modes of operation. Different operating modes require different amounts of power, implying a dynamic system. The motivation behind this paper is for wireless power transfer systems where the transmission distance is not constant and there are multiple operation modes.

For static designs where changes in loading and coupling are not considered, any change in these parameters leads to non-optimal conditions, thereby leading to too little or too much power transferred. Both of these cases must be avoided so the circuits operate correctly and are not damaged. In order to account for a dynamic

system, closed loop control must be employed. This paper offers one approach to a closed loop design.

1.3.3 System Architecture

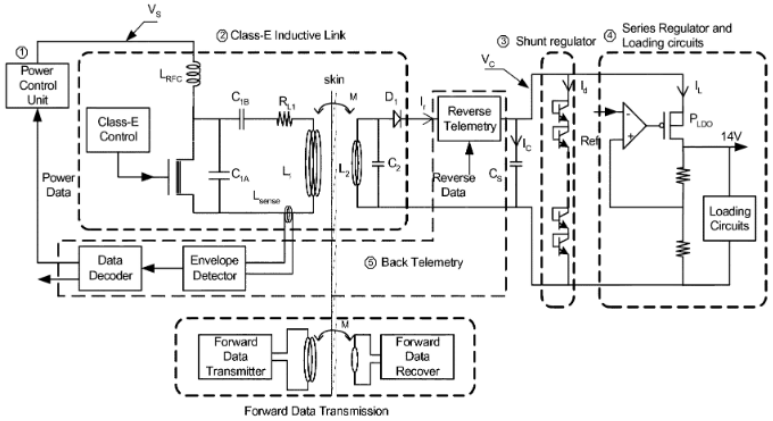

Figure 1.16: The system architecture presented in [11] for the purposes of power transfer to a retinal implant.

The architecture presented by Wang, Liu, *et al.* is shown in Figure 1.16. There are two discrete parts to the system: the external driving circuit, and the implanted receiving circuit. The two are inductively joined through an air/tissue interface. Both external and implanted circuits may be broken down into sub circuits: The power control unit, Class E inductive link, shunt regulator, series regulator, and back telemetry. Each of these are reviewed in more detail in the following sections.

1.3.4 Class E Power Link

The Class E inductive link, coined by the authors, consists of a Class E power amplifier, two inductively coupled coils, and a simple rectifier. The Class E power amplifier was chosen to drive the wireless power transfer subsystem due to its high efficiency and ability to drive inductive loads. The pair of coils are electrically, but not physically connected, allowing one to be implanted. The implanted coil alone cannot achieve the required voltage, so a resonant capacitor was added. A simple diode and capacitor is used to convert AC to DC for use in powering the subsequent circuits.

An off-chip rectification diode must be used since the current through it may be too large for an on-chip to handle.

1.3.5 Regulation

The DC power is regulated by a series of diode connected bipolar devices before being fed into a low dropout regulator. One reason for the series of diodes instead of a zener regulator is to divide the voltage down to a level acceptable for the analog-to-digital converter used in the reverse telemetry circuitry. Unfortunately, the design of the low dropout regulator is not discussed in this paper.

1.3.6 Reverse Telemetry

By temporarily disconecting the load, a change in current in the primary coil may be detected. Thus data can be encoded by modulating a switch that switches between two distinct loads. The amount of time that the load is disconnected is denoted as T_{off}. Using different T_{off} times to encode 0 and 1 is not an option because there could be fluxuations in the pulsewidth which corrupt the data. Instead, the time differential between two off pulses is used.

The data encoding scheme works as follows: The switch is normally closed and is only disabled for short periods of time. Hence the gate signal is usually high, but then goes low for some time, T_{off}. Each bit is encoded by sending two pulses in a 300 μs window. When the time between the two pulses is 60% of the total period (180 μs), it is interpreted as a 1. When the time between the two pulses is 40% of the period (120 μs), it is interpreted as a 0.

1.3.7 Power Control Unit

The power control unit consists of a detector, decoder, PWM generator, and buck/boost converter. The detector circuit converts small changes in primary inductor current into a serial stream of data. The data is then decoded and interpreted by an FPGA. The output of the FPGA, which is based on the control protocol, is fed to a

PWM generator whose output duty cycle is proportional to its digital input. This PWM signal modulates the gate of a transistor in the DC-DC converter. The output of the converter is a DC voltage whose value is proportional to the duty cycle of the input PWM signal, $V_s = D_{cycle}V_{dc}$. The output of the DC-DC converter is the power amplifier supply voltage, thus closing the feedback loop.

Anything that causes changes in primary inductor current will be detected by the current sensing inductor, therefore potentially corrupting the data. The DC-DC converter introduces a ripple on the supply voltage, and therefore can cause the inductor current to change and corrupt the data signal. This can be mitigated by increasing the filter capacitance on the converter. The trade-off is primary inductor current settling time. Recall that 1.2 ms is allotted to allow for settling, placing an upper limit on how large the filter capacitor can be.

1.3.8 Stability

Closed loop circuit design is not complete without a discussion of stability and steady state error. Stability analysis was performed by linearizing each sub-circuit and finding the loop transfer function. A controller was added whose transfer function was chosen specifically to increase stability. The voltage across the smoothing capacitor is the function to be stabilized.

The Class-E inductive link is characterized as a gain, K_E. The power control unit is represented as $\frac{F(s)}{s}$ where F(s) is the stabilization controller and the integrator term is for minimization of steady state error. Since reverse telemetry requires a non-zero encoding/decoding time, its block was modeled as a time delay whose Laplace transform is e^{-sD}. The transmission delay, D, is 7 bits long. Since each bit period is 300 μs, the transmission delay is about 2.1 ms.

The shunt regulator diodes have an exponential IV-characteristic. For transfer function analysis, this relationship is linearized around the stabilization voltage of 15 V. The linearization is valid for small changes in V_c, which is physically the case since

regulators allow only small changes in voltage. Therefore, the equivalent resistance R_d is found through the linearization as (1.52). From their curvefit parameters ($V_0 = 0.588$ V and $I_0 = 7.5 \times 10^{-16}$ A), this resistance is calcuated to be about 6.5 kΩ.

$$R_d = \frac{V_0}{I_0} e^{-\frac{V_c}{V_0}} \Bigg|_{V_c=15V} \tag{1.52}$$

A Bode plot of the uncompensated transfer function shows the system is close to unstable, therefore requiring compensation. The compensation tranfer function is denoted as F(s). Therefore, the total system transfer funciton is denoted by $T(s)$ in (1.53).

$$\begin{aligned} T(s) &= \frac{G(s)}{1 + G(s)H(s)} \\ G(s) &= \frac{1}{1/R_d + sC} \\ H(s) &= \frac{K_E}{s} e^{-sD} F(s) \end{aligned} \tag{1.53}$$

The smoothing capacitor and input resistance of the shunt regulator provide a pole at $\frac{1}{R_d C_s} \approx 10$ Hz that, without F(s), determines stability. The higher the pole (lower R_d and C_s), the more stable. Lower R_d means more power consumed in the regulator. Lower C_s means larger voltage ripple. Neither of these are desirable, so F(s) is employed to improve the phase response without the need for reducing R_d or C_s.

The best choice for F(s) is to add a zero to partially cancel the effect of the pole. Therefore F(s) has the form (1.54). Addition is accomplished by parallel circuits. Therefore F(s) is composed of the parallel combination of a differentiator ($K_D s$) and gain block (K_A). The differentiation and gain constants are chosen to partially cancel the pole, with value at 16 Hz. The differntiation circuit topology consists of two differential switched capacitors and an amplifier. The gain is provided by a 4-bit ADC.

$$F(s) = K_A + K_D s \tag{1.54}$$

1.3.9 Data Encoding

As stated in the section on reverse telemetry, data is encoded in current changes sensed in the primary coil. However, adjusting the power level also causes a change in current in the primary coil, and thus can corrupt the data signal. In order to avoid this issue, power adjustment and data reading are scheduled to occur at different times. The power is adjusted at the beginning of a data packet. During this time, any changes in coil current are ignored. The authors allot 1.2 ms for the power adjustment to settle before beginning to read data.

The sampling frequency was chosen to be 167 Hz, roughly 10 times larger than the compensation zero, corresponding to a 6 ms packet period. The data packet format is given by (1.55), where T_{settle} is the 1.2 ms current settling period due to updating the amplifier supply voltage, X_i are reserved for information such as tissue impedance and temperature, D_{derv} is the derivative bit, D_i are the 4 ADC bits, and P_i are two parity bits. There are 9 bits of information, 5 bits of power information, and 2 parity bits for a total of 16 bits. Each bit period is 300 μs, so the packet period is 16 bit periods plus the null settling time header for a total packet period of 6 ms.

$$\text{Packet} \equiv T_{settle} X_8 X_7 X_6 X_5 X_4 X_3 X_2 X_1 X_0 D_{derv} D_3 P_1 D_2 D_1 D_0 P_2 \tag{1.55}$$

The derivative bit determines whether the rectified voltage is increasing or decreasing. The ADC bits determine the voltage value. The parity bits help to ensure that the decoded information has been received correctly.

1.3.10 Data Decoding

The data is decoded on the primary side through an analog envelope detector and digital data decoder. Changes in primary coil current are detected by a current sensing

inductor, which converts the current into a voltage that is then passed to the data decoding circuitry. Since data is encoded as the time between two pulses, the design is insensitive to variations in the pulse widths. The digital decoder was implemented in an FPGA.

1.3.11 Verification

The circuits were physically fabricated and tested with predictable, desirable results. The power efficiency achieved is reported to be worst case 33.3% and best case 65.8%.

1.4 The Proposed Closed Loop Wireless Power Transfer System

There has been a significant amount of research similar to that of this project, some of which has been reviewed in the previous sections. The insight from these has been used as a foundation to develop a system that is capable of transferring power to a neural recording implant while maintaining the specifications discussed formerly. A block diagram of the proposed system may be observed in Figure 1.17.

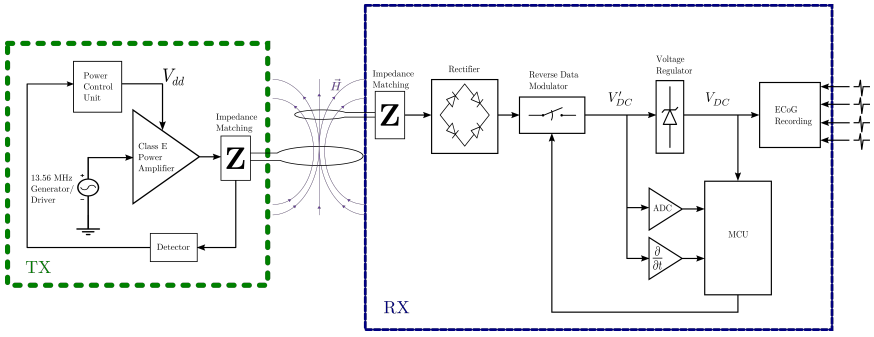

Figure 1.17: The transmitting and receiving architectures of the proposed wireless power transfer system.

The system consists of an external power transmission circuit and an internal power receiving circuit. At some point, the receiver will be miniaturized on chip in order to satisfy the implant size constraint. For prototype purposes, size is not considered a constraint such that the concepts may be emphasized and off-the-shelf components may be utilized.

The power transmitter consists of a 13.56 MHz frequency generator, power amplifier,

reverse data detector, and a power control unit. The receiver consists of a rectifier, regulator, neural data processing chip and electrodes, and a data driven switch controlled by a microcontroller. The TX and RX circuits are inductively linked with a system of coils that employ a reconfigurable impedance matching network. The impedance matching dynamically shifts due to changes in the environmental conditions such that optimal or near optimal efficiency may be achieved at all times.

In the following sections, theoretical analysis is presented that is necessary to fully understand biomedically implantable systems that are powered wirelessly through a set of inductively coupled coils. From the analysis, the design considerations of such a system are discussed.

CHAPTER 2: RESONANT WIRELESS POWER TRANSFER THEORETICAL ANALYSIS AND DESIGN

2.1 Resonant Wireless Power Transfer Theory

This section seeks to draw from and expand upon the theory behind resonant based wireless power transfer systems. In particular, the equations stated in [13] are derived in detail to avoid ambiguity.

It has been known since the days of Faraday that two circuits not physically connected may still be linked such that a time-varying voltage applied to one circuit causes a time-varying voltage in the other circuit. This principal is known as magnetic induction. Power transfer between two inductively coupled circuits requires two main components: a time-varying source and rapidly spacially-varying circuits (inductors). Power transfer between two inductively coupled circuits is summarized by Faraday's and Ampere's laws.

$$\nabla \times \vec{E} = -\frac{\partial \vec{B}}{\partial t} \tag{2.1}$$

$$\nabla \times \vec{H} = \vec{J} + \frac{\partial \vec{D}}{\partial t} \tag{2.2}$$

From (2.1), we see that an external time-varying magnetic field produces a voltage in the circuit. From (2.2), we see that a time-varying electric current in a circuit produces a circulating magnetic field.

Some circuit geometries are more conducive to inductive coupling than others, namely, coils of wire. When two coils of wire are placed near each other with a source on one and a load on the other, the magnetic field from the source coil intersects

the load coil, inducing a voltage in the load coil. This is the fundamental basis of transformers, as well as wireless power transfer.

2.1.1 Input Impedance of a Coil

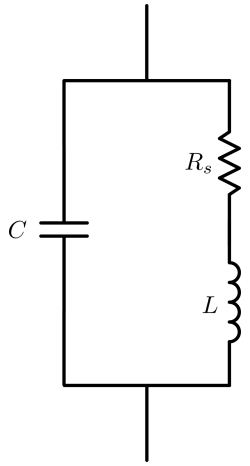

Figure 2.1: The equivalent circuit model of a wire coil using lumped circuit elements.

A wire coil may be modeled as a parallel LC tank where the inductor has a small series resistance and the capacitor has a small parallel conductance. This is displayed in Figure 2.1 with the parallel conductance loss negligible compared to the inductor equivalent series resistance. The input impedance of such circuit is given by (2.3a) – (2.3b).

$$R_{in} = \frac{R_s(1 + R_sG) + \omega^2L^2G}{(1 + R_sG - \omega^2LC)^2 + \omega^2(LG + R_sC)^2} \tag{2.3a}$$

$$X_{in} = \frac{\omega L(1 - \omega^2LC) - \omega R_s^2C}{(1 + R_sG - \omega^2LC)^2 + \omega^2(LG + R_sC)^2} \tag{2.3b}$$

Here, C refers to the total capacitance of the coil. This includes the parasitic capacitance of the coil, which is typically small, and any external capacitance which is physically connected across the coil terminals. In the latter case, a physical capacitor will have some losses which manifest themselves as an equivalent parallel conductance, G.

The resonant frequency of a circuit occurs when the imaginary part of its input impedance equals zero (*i.e.* $X_{in} = 0$). For a coil of wire, this frequency is given by (2.4).

$$f_{res} = \frac{1}{2\pi}\sqrt{\frac{1}{LC} - \left(\frac{R_s}{L}\right)^2} \tag{2.4}$$

When the coil is a single turn, its self capacitance is small, therefore having a high resonant frequency. If the operating frequency is much smaller than the self-resonant frequency, the capacitance may be ignored altogether. The simplified circuit is then a series RL with input impedance $Z_{in} = R_s + j\omega L$.

A single inductive loop was constructed in HFSS as shown in Figure 2.2.

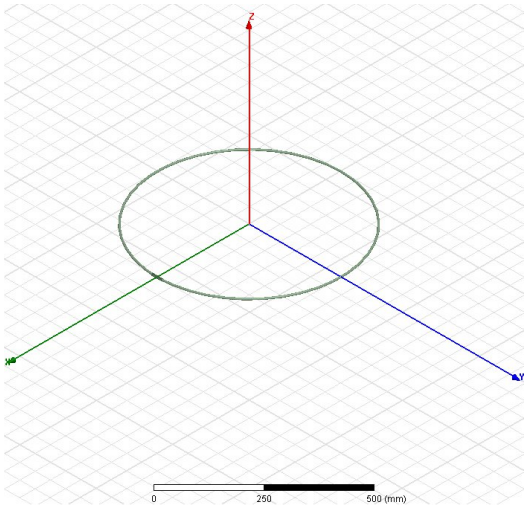

Figure 2.2: A Single-Turn Loop Drawn in HFSS

2.1.2 Analysis of Non-Resonant Power Transfer Between Two Coils

Two axially aligned inductive loops may be modeled as the circuit of Figure 2.3. Since the loops have only one turn, their self capacitance is low. For this analysis, it is assumed that the operating frequency is much lower than the self resonant frequency, such that the capacitors may be ignored.

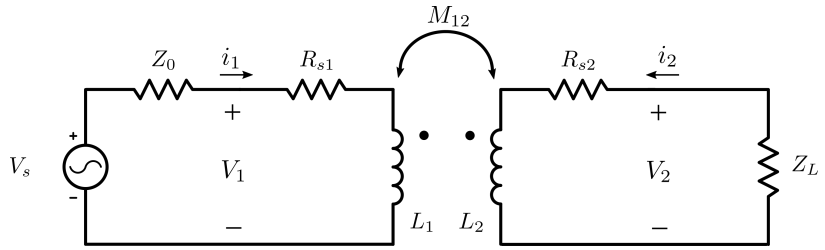

Figure 2.3: Approximate Circuit for Two Inductively Coupled Coils

2.1.3 Linear System for Currents

Ignoring capacitors and applying Kirchoff's Voltage Law (KVL) to each mesh results in the linear system (2.5)

$$\begin{aligned} V_s &= Z_1 i_1 - Z_{12} i_2 \\ 0 &= Z_{12} i_1 - Z_2 i_2 \end{aligned} \tag{2.5}$$

The solution is given by (2.6).

$$\begin{bmatrix} i_1 \\ i_2 \end{bmatrix} = \frac{V_s}{Z_1 Z_2 - Z_{12}^2} \begin{bmatrix} Z_2 \\ Z_{12} \end{bmatrix} \tag{2.6}$$

where the impedances are defined as (2.7) – (2.9).

$$Z_1 = Z_0 + R_{s1} + j\omega L_1 \tag{2.7}$$

$$Z_2 = R_{s2} + R_L + j\left(X_L + \omega L_2\right) \tag{2.8}$$

$$Z_{12} = j\omega M_{12} \tag{2.9}$$

2.1.4 Mutual Inductance and Coupling Coefficients

The mutual inductance between two circuits may be expressed by Neumann's form (2.10).

$$M_{ij} = \frac{\mu_0}{4\pi} \oint_{C_i} \oint_{C_j} \frac{\mathbf{d}\boldsymbol{\ell}_i \cdot \mathbf{d}\boldsymbol{\ell}_j}{|\mathbf{r}_j - \mathbf{r}_i|} \tag{2.10}$$

After a considerable amount of work, it can be shown that in the case of two axially aligned, single turn, circular coils, the mutual inductance is given by (2.11)

$$M_{ij} = \mu_0 \sqrt{r_i r_j k_{ij}^2} \int_0^{\frac{\pi}{2}} \frac{2\sin^2\phi - 1}{\sqrt{1 - k_{ij}^2 \sin^2\phi}} d\phi \tag{2.11}$$

where, $k_{ij}^2 = \frac{4r_i r_j}{d_{ij}^2 + (r_i + r_j)^2}$.

Therefore, the coupling coefficient between coils i and j is given by (2.12).

$$K_{ij} = \frac{M_{ij}}{\sqrt{L_i L_j}} \tag{2.12}$$

2.1.5 Power Transfer Efficiency

Four useful parameters, when determining power transfer efficiency, are the input and output voltages, the magnitudes squared of the currents, and the real part of the current in the primary coil. From the circuit diagram and (2.6), it is clear that:

$$\begin{cases} V_{in} = V_s - i_1 Z_0 \\ V_{out} = i_2 Z_L \\ |i_{1,2}|^2 = \frac{V_s^2}{\left|Z_1 Z_2 - Z_{12}^2\right|^2} |Z_{2,12}|^2 \\ \Re\{i_1\} = \frac{V_s}{\left|Z_1 Z_2 - Z_{12}^2\right|^2} \left(|Z_2|^2 \Re\{Z_1\} - Z_{12}^2 \Re\{Z_2\}\right) \end{cases}$$

The power transfer efficiency is given by (2.13).

$$
\begin{aligned}
\eta = \frac{P_{out}}{P_{in}} &= \frac{\frac{1}{2}\Re\left\{V_{out} i_2^*\right\}}{\frac{1}{2}\Re\left\{V_{in} i_1^*\right\}} \\
&= \frac{R_L |i_2|^2}{V_s \Re\left\{i_1\right\} - Z_0 |i_1|^2} \\
&= \frac{R_L |Z_{12}|^2}{|Z_2|^2 \Re\left\{Z_1\right\} - Z_{12}^2 \Re\left\{Z_2\right\} - Z_0 |Z_2|^2} \\
&= \frac{R_L |Z_{12}|^2}{|Z_2|^2 R_{s1} - Z_{12}^2 \left(R_L + R_{s2}\right)} \\
&= \frac{\omega^2 M_{12}^2 R_L}{R_{s1}\left[(R_L + R_{s2})^2 + (X_L + \omega L_2)^2\right] + \omega^2 M_{12}^2 \left(R_L + R_{s2}\right)}
\end{aligned}
\tag{2.13}
$$

2.1.6 Optimal Load and Maximum Efficiency

By equating the derivatives of η with respect to R_L and X_L to zero, the value of the complex load may be determined, which allows power transfer at optimal efficiency.

$$
\begin{cases}
\frac{\partial \eta}{\partial X_L} = 0 \\
\frac{\partial \eta}{\partial R_L} = 0
\end{cases}
$$

The derivative with respect to the reactive part is simple, as X_L only appears once. Therefore, it may be determined that the optimal value for the load reactance is $X_L = -\omega L_2$. The derivative with respect to the resistive part is more complicated. The efficiency is a linear function of load resistance, divided by a quadratic function of load resistance. So, for simplicity, the constant terms will be lumped and arbitrarily named.

$$\begin{aligned}
\eta &= \frac{AR_L}{BR_L^2 + CR_L + D} \\
\frac{\partial \eta}{\partial R_L} &= \frac{-AR_L(2BR_L + C)}{(BR_L^2 + CR_L + D)^2} + \frac{A}{BR_L^2 + CR_L + D} = 0 \\
&\Rightarrow -R_L(2BR_L + C) + BR_L^2 + CR_L + D = 0 \\
&\Rightarrow BR_L^2 - D = 0 \\
&\Rightarrow R_L = \pm\sqrt{\frac{D}{B}}
\end{aligned} \tag{2.14}$$

The negative value of load resistance may be thrown away, as negative resistors will not be addressed here. D is the term constant with respect to R_L in the denominator of (2.13). B is the coefficient of the quadratic term with respect to R_L in the denominator of (2.13). Therefore, the optimal loading impedance is given by (2.15).

$$Z_L^{opt} = R_{s2}\sqrt{1 + \omega^2 M_{12}^2 \tfrac{1}{R_{s1}R_{s2}}} - j\omega L_2 \tag{2.15}$$

There are two terms that appear commonly in the analysis of the discussed wireless power transfer system. Therefore, the intermediate variable Δ will be defined as (2.16) for future simplicity.

$$\Delta = \omega^2 M_{12}^2 \tfrac{1}{R_{s1}R_{s2}} \tag{2.16}$$

The other useful term, derived in (2.17), comes about when deriving the input impedance to two coils in the next section, and carries through the remainder of the

derivations.

$$
\begin{aligned}
& 1+\frac{\Delta}{1+\sqrt{1+\Delta}} \\
&= \frac{1+\Delta+\sqrt{1+\Delta}}{1+\sqrt{1+\Delta}} \cdot \frac{1-\sqrt{1+\Delta}}{1-\sqrt{1+\Delta}} \\
&= \frac{1+\Delta+\sqrt{1+\Delta}-(1+\Delta+\sqrt{1+\Delta})\sqrt{1+\Delta}}{1-(1+\Delta)} \\
&= \sqrt{1+\Delta}
\end{aligned} \tag{2.17}
$$

Therefore, when the two coils are loaded optimally, power is transfered at a maximum and the maximum efficiency is given by (2.18).

$$
\begin{aligned}
\eta_{max} &= \eta\big|_{Z_L=R_{s2}\sqrt{1+\Delta}-j\omega L_2} \\
&= \frac{\omega^2 M_{12}^2 R_{s2}\sqrt{1+\Delta}}{R_{s1}\left[(R_{s2}\sqrt{1+\Delta}+R_{s2})^2\right]+\omega^2 M_{12}^2\left(R_{s2}\sqrt{1+\Delta}+R_{s2}\right)} \\
&= \frac{R_{s2}\sqrt{1+\Delta}}{R_{s2}(1+\sqrt{1+\Delta})} \cdot \frac{\omega^2 M_{12}^2}{R_{s1}R_{s2}(1+\sqrt{1+\Delta})+\omega^2 M_{12}^2} \cdot \frac{\frac{1}{R_{s1}R_{s2}}}{\frac{1}{R_{s1}R_{s2}}} \\
&= \frac{\sqrt{1+\Delta}}{(1+\sqrt{1+\Delta})} \cdot \frac{\Delta}{(1+\sqrt{1+\Delta})+\Delta} \\
&= \frac{\Delta}{(1+\sqrt{1+\Delta})} \cdot \frac{\sqrt{1+\Delta}}{\sqrt{1+\Delta}+1+\Delta} \cdot \frac{\frac{1}{\sqrt{1+\Delta}}}{\frac{1}{\sqrt{1+\Delta}}} \\
&= \frac{\Delta}{\left(1+\sqrt{1+\Delta}\right)^2}
\end{aligned} \tag{2.18}
$$

2.1.7 Input Impedance and Mutual Impedance

The input impedance of two coils terminated with the optimal load from (2.15) (given by $Z_{in} = \frac{V_{in}}{i_1}$) is derived below.

$$
\begin{aligned}
Z_{in}|_{Z_L=Z_L^{opt}} &= \frac{(R_{s1}+j\omega L_1)i_1 - j\omega M_{12} i_2}{i_1} \\
&= R_{s1} + j\omega L_1 - j\omega M_{12}\tfrac{Z_{12}}{Z_2} \\
&= R_{s1} + j\omega L_1 + \left.\frac{\omega^2 M_{12}^2}{R_{s2}+R_L+j(X_L+\omega L_2)}\right|_{Z_L=Z_L^{opt}} \\
&= R_{s1} + \frac{\omega^2 M_{12}^2}{R_{s2}+R_{s2}\sqrt{1+\omega^2 M_{12}^2 \frac{1}{R_{s1}R_{s2}}}} \cdot \frac{\frac{R_{s1}}{R_{s1}R_{s2}}}{\frac{1}{R_{s2}}} + j\omega L_1 \\
&= R_{s1} + \frac{R_{s1}\Delta}{1+\sqrt{1+\Delta}} + j\omega L_1 \\
&= R_{s1}\sqrt{1+\Delta} + j\omega L_1
\end{aligned} \tag{2.19}
$$

The authors of [13] state that the input impedance is (2.20).

$$
\begin{aligned}
Z_{in}|_{Z_L=Z_L^{opt}} &= R_{s1}\left(1+\eta_{max}\right) + j\omega L_1 \\
&= R_{s1}\left(1 + \frac{\Delta}{\left(1+\sqrt{1+\Delta}\right)^2}\right) + j\omega L_1 \\
&\neq R_{s1}\left(1 + \frac{\Delta}{1+\sqrt{1+\Delta}}\right) + j\omega L_1
\end{aligned} \tag{2.20}
$$

This equation is simply stated in the paper, not derived.

As described in the second line of (2.19), the mutual impedance between two coils is given by (2.21)

$$
Z_{Mij} = \frac{\omega^2 M_{ij}^2}{Z_j} \tag{2.21}
$$

where Z_j is the series loop impedance of the j^{th} coil. This will be useful in the analysis of systems of four coils.

2.1.8 Analysis of Resonant Power Transfer Between Four Coils

In a wireless power transfer system composed of four coils, the center two may be considered to be the same as those discussed in the two coil system. The two outer coils are added for the purpose of impedance matching. The overall network may be treated as a two port network and is shown in Figure 2.4.

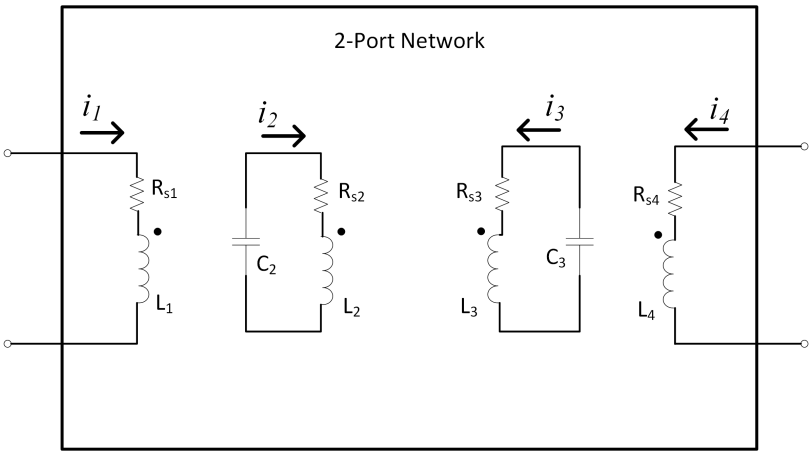

Figure 2.4: Four Coil WPT System Represented as a 2-Port Network

With the existence of an additional load-side coil, the impedance looking from coil 3 to coil 4 may be set equal to the optimal load impedance. This is shown below.

$$\begin{aligned} Z_{M34} + \frac{1}{j\omega C_3} &= Z_L^{opt} \\ \frac{\omega^2 M_{34}^2}{R'_L + jX'_L} + \frac{1}{j\omega C_3} &= Z_L^{opt} \\ \frac{\omega^2 M_{34}^2}{R_L'^2 + X_L'^2}\left(R'_L - jX'_L\right) - j\frac{1}{\omega C_3} &= R_{s3}\sqrt{1+\Delta} - j\omega L_3 \end{aligned} \tag{2.22}$$

where $R'_L = R_L + R_{s4}$ and $X'_L = X_L + \omega L_4$.

By equating real and imaginary parts, the following expressions for coupling coefficient and capacitance may be determined as given by (2.23) and (2.24).

$$K_{34} = (1+\Delta)^{1/4}\sqrt{\frac{R_{s3}\left(R_L'^2 + X_L'^2\right)}{\omega^2 L_3 L_4 R_L'}} \tag{2.23}$$

$$C_3 = \frac{1}{\omega^2 L_3}\cdot\frac{1}{1-\left(\frac{X_L' R_{s3}\sqrt{1+\Delta}}{\omega L_3 R_L'}\right)} \tag{2.24}$$

It should be noted here that in [13], the imaginary part of the load is assumed to be zero, leading to a slight inconsistancy. The inclusion of X_L in (2.23) and (2.24) does not complicate the equations any further. Therefore it is included for more generality.

Now, the input impedance looking into an optimally loaded coil pair has already been derived as (2.19). In order to match this impedance to the characteristic impedance of the source, a final coil is added adjacent. Therefore, the input impedance to the entire system is given as (2.25).

$$Z_{in} = R_{s1} + j\omega L_1 + \frac{\omega^2 M_{12}^2}{R_{s2}\sqrt{1+\Delta} + j\left(\omega L_2 - \frac{1}{\omega C_2}\right)} \tag{2.25}$$

$$\begin{cases} \omega L_1 - \frac{\omega^2 M_{12}^2\left(\omega L_2 - \frac{1}{\omega C_2}\right)}{R_{s2}^2\sqrt{1+\Delta}^2 + \left(\omega L_2 - \frac{1}{\omega C_2}\right)^2} = X_{in} \\ R_{s1} + \frac{\omega^2 M_{12}^2 R_{s2}\sqrt{1+\Delta}}{R_{s2}^2\sqrt{1+\Delta}^2 + \left(\omega L_2 - \frac{1}{\omega C_2}\right)^2} = R_{in} \end{cases}$$

In [13], the real part was equated to an arbitrary resistance, R_{in}. The design choice of R_{in} will be examined later. For now, this resistance may be set equal to the characteristic impedance of the input source, Z_0.

For convenience, define $X_2 = \omega L_2 - \frac{1}{\omega C_2}$. The equation forcing the imaginary component of Z_{in} to X_{in} gives K_{12}. The equation matching the real component of

Z_{in} to R_{in} gives X_2.

$$K_{12}^2 = \frac{(\omega L_1 - X_{in})\left(R_{s2}^2\sqrt{1+\Delta}^2 + X_2^2\right)}{\omega^2 L_1 L_2 X_2}$$
$$X_2 = \frac{\omega L_1 R_{s2}\sqrt{1+\Delta}}{R_{in} - R_{s1}}$$

And thus,

$$K_{12} = (1+\Delta)^{1/4}\sqrt{\frac{R_{s2}\left((R_{in}-R_{s1})^2 + (\omega L_1 - X_{in})^2\right)}{\omega^2 L_1 L_2 (R_{in}-R_{s1})}} \tag{2.26}$$
$$C_2 = \frac{1}{\omega^2 L_2}\cdot\frac{1}{1-\frac{R_{s2}\sqrt{1+\Delta}(\omega L_1 - X_{in})}{(R_{in}-R_{s1})\omega L_2}} \tag{2.27}$$

In [13], K_{12} is reported to have a factor of $\sqrt{\frac{(1+\Delta)\left[\Delta^2+8\Delta+8+4(\Delta+2)\sqrt{1+\Delta}\right]}{4\Delta^2+12\Delta+8+(\Delta^2+8\Delta+8)\sqrt{1+\Delta}}}$. In reality, this quantity is simply equal to $(1+\Delta)^{1/4}$, and the equation is consistent with the derivation presented here.

2.1.9 Impedance Parameters

The analysis presented in [13] and reviewed above is a great starting point for this research. However, the power transfer effiency η is not necessarily the best metric for assessing the performance of the system. A more common metric in electromagnetics is a network's S-parameters.

Since the analysis of this system is elementary in terms of an equivalent circuit using standard circuit analysis techniques, it makes sense to begin by determining the Z-parameters. Once these are obtained, a conversion from Z to S parameters will be made.

For a two-port network, the dimensions of the impedance matrix is 2x2. The first column of this matrix will be determined by applying a voltage to port 1, while port 2 is left open. This setup may be observed in Fig. 2.5.

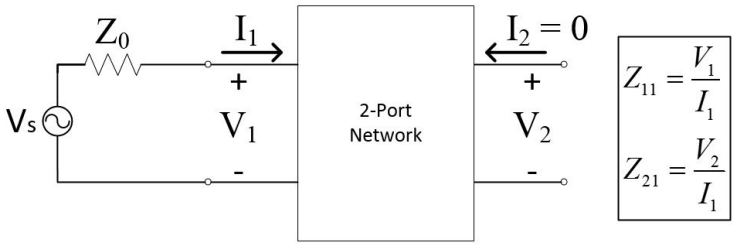

Figure 2.5: Circuit 1 – Apply Vs to Port 1, Open Circuit Port 2

The second column of the impedance matrix will be determined by applying a voltage to port 2, while port 1 is left open. This setup may be observed in Fig. 2.6.

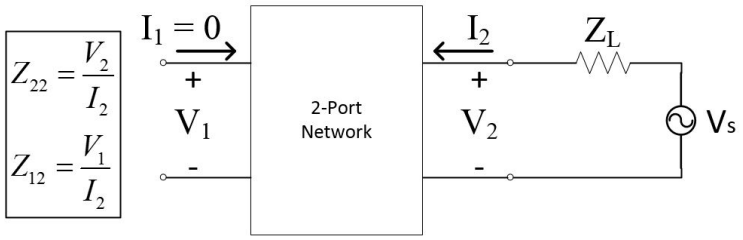

Figure 2.6: Circuit 2 – Apply Vs to Port 2, Open Circuit Port 1

The equivalent circuit of the four coil system may be interpreted as a two port network as described by Fig. 2.4. For analysis purposes, the directions of the four currents is arbitrary. For consistency with 2-port network theory, i_1 and i_4 were chosen to conduct *into* the ports. Currents i_2 and i_3 were arbitrarily chosen.

Fig. 2.4 assumes that all four coils are wound the same direction, as is implied by the dot convention shown. In terms of power transfer, the dot convention is irrelevant. In terms of analysis, some convention must be assumed and parameters such as the Z-parameters are relative to this assumption. All currents were chosen into the respective dots and therefore the sign of each mutual inductance term matches the sign of its respective self inductance term.

Careful consideration must be given to determine the signs of the mutual inductance terms. A single incorrect sign will result in meaningless results.

For the purposes of this analysis, define the circuit's impedances as follows. The four inductor impedances are given as Z_i'. The six mutual impedances are given as Z_{ij}.

$$Z_i' = R_{si} + j\omega L_i$$

$$Z_{ij} = j\omega M_{ij}$$

The four series loop impedances are given by Z_i.

$$\begin{aligned} Z_1 &= Z_0 + Z_1' \\ Z_2 &= \frac{1}{G_2 + j\omega C_2} + Z_2' \\ Z_3 &= \frac{1}{G_3 + j\omega C_3} + Z_3' \\ Z_4 &= Z_L + Z_4' \end{aligned}$$

2.1.10 The Dot Convention for Inductors

From time to time, it may be helpful to review how to determine the polarity of a mutual inductance with the dot convention. There are many ways to solve this problem, one of which is presented here.

1. Arbitrarily assign direction of current through inductors.
2. Use KVL to determine the sign of the self inductance term.
3. If both currents enter or both leave their dotted terminals, the mutual inductance sign matches the sign of the self inductance.
4. Inversely, if one current enters a dot while the other leaves, the sign of the mutual inductance is opposite the sign of the self inductance.

A summary of this method is given in Figure 2.7.

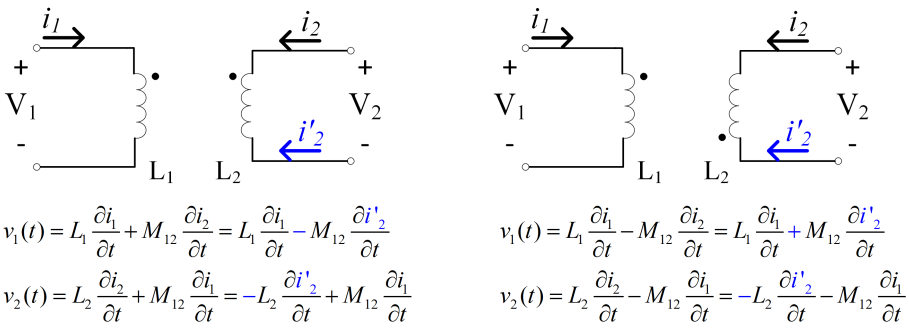

(a) Mutually Coupled Inductors with Same Polarity and Their Equations

(b) Mutually Coupled Inductors with Opposite Polarity and Their Equations

Figure 2.7: Summary of Mutual Inductance Polarity

2.1.11 Determining $[\mathbf{Z}]_{11}$ and $[\mathbf{Z}]_{21}$ with Circuit 1

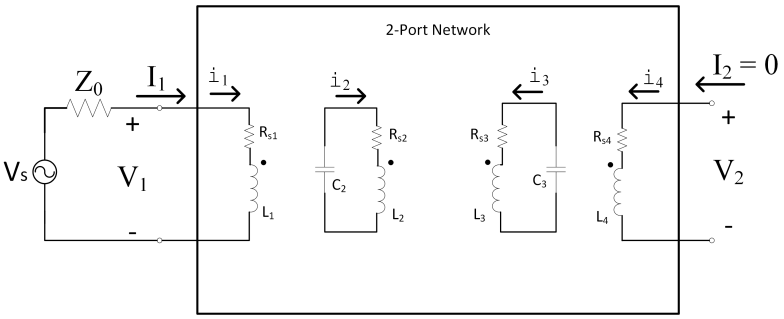

Figure 2.8: Circuit 1 – Apply Vs to Port 1, Open Circuit Port 2

The circuit of Fig. 2.4 may be connected in the configuration of Fig. 2.5 such that $[\mathbf{Z}]_{11}$ and $[\mathbf{Z}]_{21}$ may be determined.

Kirchoff's Voltage Law may be applied to each of the loops, generating the equations below. Note that $I_2 = i_4 = 0$ is known, so only three equations are necessary.

$$
\begin{aligned}
V_s - (Z_0 + R_{s1} + j\omega L_1)i_1 - (j\omega M_{12})i_2 - (j\omega M_{13})i_3 &= 0 \\
-\left(\frac{1}{G_2 + j\omega C_2} + R_{s2} + j\omega L_2\right) i_2 - (j\omega M_{12})i_1 - (j\omega M_{23})i_3 &= 0 \\
-\left(\frac{1}{G_3 + j\omega C_3} + R_{s3} + j\omega L_3\right) i_3 - (j\omega M_{13})i_1 - (j\omega M_{23})i_2 &= 0
\end{aligned}
$$

KVL may also be applied separately to the first and last loop to determine expressions

for the port voltages, V_1 and V_2.

$$V_1 = V_s - Z_0 i_1$$

$$V_2 = (j\omega M_{14})i_1 + (j\omega M_{24})i_2 + (j\omega M_{34})i_3$$

These two sets of equations are presented compactly in matrix form.

$$\begin{bmatrix} Z_1 & Z_{12} & Z_{13} \\ Z_{12} & Z_2 & Z_{23} \\ Z_{13} & Z_{23} & Z_3 \end{bmatrix} \begin{bmatrix} i_1 \\ i_2 \\ i_3 \end{bmatrix} = \begin{bmatrix} V_s \\ 0 \\ 0 \end{bmatrix} \tag{2.28}$$

$$\begin{bmatrix} V_1 \\ V_2 \end{bmatrix} = \begin{bmatrix} -Z_0 & 0 & 0 \\ Z_{14} & Z_{24} & Z_{34} \end{bmatrix} \begin{bmatrix} i_1 \\ i_2 \\ i_3 \end{bmatrix} + \begin{bmatrix} V_s \\ 0 \end{bmatrix} \tag{2.29}$$

The expressions for current may be obtained through various linear algebra techniques. Cramer's Rule is a good choice in this situation.

$$[\mathbf{Z}]_{11} = \frac{V_1}{i_1} = Z_1' - \frac{Z_{12}^2 Z_3 - 2Z_{12}Z_{13}Z_{23} + Z_{13}^2 Z_2}{Z_2 Z_3 - Z_{23}^2} \tag{2.30}$$

$$[\mathbf{Z}]_{21} = \frac{V_2}{i_1} = Z_{14} + \frac{Z_{24}(Z_{13}Z_{23} - Z_3 Z_{12}) + Z_{34}(Z_{12}Z_{23} - Z_2 Z_{13})}{Z_2 Z_3 - Z_{23}^2} \tag{2.31}$$

2.1.12 Determining $[\mathbf{Z}]_{22}$ and $[\mathbf{Z}]_{12}$ with Circuit 2

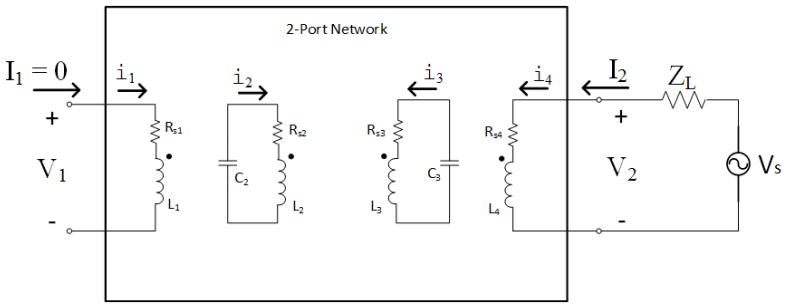

Figure 2.9: Circuit 1 – Apply Vs to Port 1, Open Circuit Port 2

The circuit of Fig. 2.4 may be connected in the configuration of Fig. 2.6 such that $[\mathbf{Z}]_{22}$ and $[\mathbf{Z}]_{12}$ may be determined.

Kirchoff's Voltage Law may be applied to each of the loops, generating the equations below. Note that $I_1 = i_1 = 0$ is known, so only three equations are necessary.

$$\begin{aligned} V_s - (Z_L + R_{s4} + j\omega L_4)i_4 - (j\omega M_{24})i_2 - (j\omega M_{34})i_3 = 0 \\ -\left(\frac{1}{G_3 + j\omega C_3} + R_{s3} + j\omega L_3\right) i_3 - (j\omega M_{23})i_2 - (j\omega M_{34})i_4 = 0 \\ -\left(\frac{1}{G_2 + j\omega C_2} + R_{s2} + j\omega L_2\right) i_2 - (j\omega M_{23})i_3 - (j\omega M_{24})i_4 = 0 \end{aligned}$$

KVL may also be applied separately to the first and last loop to determine expressions for the port voltages, V_1 and V_2.

$$\begin{aligned} V_1 &= (j\omega M_{12})i_2 + (j\omega M_{13})i_3 + (j\omega M_{14})i_4 \\ V_2 &= V_s - Z_L i_4 \end{aligned}$$

These two sets of equations are presented compactly in matrix form.

$$\begin{bmatrix} Z_2 & Z_{23} & Z_{24} \\ Z_{23} & Z_3 & Z_{34} \\ Z_{24} & Z_{34} & Z_4 \end{bmatrix} \begin{bmatrix} i_2 \\ i_3 \\ i_4 \end{bmatrix} = \begin{bmatrix} 0 \\ 0 \\ V_s \end{bmatrix} \tag{2.32}$$

$$\begin{bmatrix} V_1 \\ V_2 \end{bmatrix} = \begin{bmatrix} Z_{12} & Z_{13} & Z_{14} \\ 0 & 0 & -Z_L \end{bmatrix} \begin{bmatrix} i_2 \\ i_3 \\ i_4 \end{bmatrix} + \begin{bmatrix} 0 \\ V_s \end{bmatrix} \tag{2.33}$$

Therefore,

$$[\mathbf{Z}]_{22} = \frac{V_2}{i_4} = Z_4' - \frac{Z_{24}^2 Z_3 - 2Z_{24}Z_{34}Z_{23} + Z_{34}^2 Z_2}{Z_2 Z_3 - Z_{23}^2} \tag{2.34}$$

$$[\mathbf{Z}]_{12} = \frac{V_1}{i_4} = Z_{14} + \frac{Z_{12}(Z_{34}Z_{23} - Z_3 Z_{24}) + Z_{13}(Z_{24}Z_{23} - Z_2 Z_{34})}{Z_2 Z_3 - Z_{23}^2} \tag{2.35}$$

2.2 Scattering Parameters

For situations where both characteristic impedances are purely real, the following equation may be used.

$$[\mathbf{S}] = ([\mathbf{Z}][Y_0] + [U])^{-1} ([\mathbf{Z}][Y_0] - [U])$$

where $[Y_0] = [Z_0]^{-1}$ and $[U]$ is the 2×2 identity matrix. However, since the load impedance may be complex, the conversion to S-parameters becomes the more complicated (2.36) [67].

$$[\mathbf{S}] = F\left([\mathbf{Z}] - [Z_0]^*\right)\left([\mathbf{Z}] + [Z_0]\right)^{-1} F^{-1} \tag{2.36}$$

where,

$$F = \begin{bmatrix} \frac{1}{2\sqrt{|R_0|}} & 0 \\ 0 & \frac{1}{2\sqrt{|R_L|}} \end{bmatrix}$$

$$[Z_0] = \begin{bmatrix} Z_0 & 0 \\ 0 & Z_L \end{bmatrix}$$

Therefore,

$$[\mathbf{S}]_{11} = \frac{([\mathbf{Z}]_{11} - Z_0^*)([\mathbf{Z}]_{22} + Z_L) - [\mathbf{Z}]_{12}[\mathbf{Z}]_{21}}{([\mathbf{Z}]_{11} + Z_0)([\mathbf{Z}]_{22} + Z_L) - [\mathbf{Z}]_{12}[\mathbf{Z}]_{21}} \tag{2.37}$$

$$[\mathbf{S}]_{21} = \frac{2[\mathbf{Z}]_{21}\sqrt{|R_0 R_L|}}{([\mathbf{Z}]_{11} + Z_0)([\mathbf{Z}]_{22} + Z_L) - [\mathbf{Z}]_{12}[\mathbf{Z}]_{21}} \tag{2.38}$$

2.2.1 Deviation in Capacitance

An LC circuit resonates at $f_{res} = \frac{1}{2\pi\sqrt{LC}}$. Assume that L is fixed and C may vary. suppose that C deviates from its original value by some amount $\Delta C = C_{new} - C$. Then its new value is defined to be:

$$C_{new} = \left(1 + \frac{\Delta C}{C}\right) C \tag{2.39}$$

where $\left(1 + \frac{\Delta C}{C}\right) \cdot 100\%$ is the percentage by which C has changed.

Therefore, the resonant frequency has shifted:

$$\begin{aligned} f_{new} &= \frac{1}{2\pi\sqrt{L\left(1 + \frac{\Delta C}{C}\right) C}} \\ &= \frac{1}{\sqrt{1 + \frac{\Delta C}{C}}} f_{res} \end{aligned} \tag{2.40}$$

Solving for the new capacitance gives:

$$\begin{aligned} \sqrt{1 + \frac{\Delta C}{C}} &= \frac{f_{res}}{f_{new}} \\ 1 + \frac{\Delta C}{C} &= \left(\frac{f_{res}}{f_{new}}\right)^2 \\ C + (C_{new} - C) &= C\left(\frac{f_{res}}{f_{new}}\right)^2 \\ C_{new} &= C\left(\frac{f_{res}}{f_{new}}\right)^2 \end{aligned} \tag{2.41}$$

Therefore, if an LC circuit is resonating at an undesirable frequency, the capacitance

value may be changed by $\left(1+\frac{\Delta C}{C}\right)\cdot 100\%$ and cause resonance at a desired frequency.

$$C_{new} = C_{current}\left(\frac{f_{undesired}}{f_{desired}}\right)^2 \tag{2.42}$$

For this WPT system, the optimal capacitance is given by (2.27), (2.24). Under normal conditions, the denominators of (2.27)), (2.24) are ≈ 1. Therefore, the resonant frequencies of the two main loops are well approximated by

$$f_{res2} = \frac{1}{2\pi\sqrt{L_2C_2}}$$
$$f_{res3} = \frac{1}{2\pi\sqrt{L_3C_3}}$$

As an example, suppose the desired resonant frequency is $f_d = 13.56$ MHz and the capacitor values were calculated to be $C_2 = 71.1$ pF and $C_3 = 2430$ pF. When the system is measured, two distinct resonant spikes are noticed at $f_{u1} = 14.1$ MHz and $f_{u2} = 14.2$ MHz. The new capacitor values that shift the undesired resonances to desired are:

$$C_{2,new} = (71.1\text{ pF})\left(\frac{14.1}{13.56}\right)^2 \approx 76.9\text{ pF}$$
$$C_{3,new} = (2430\text{ pF})\left(\frac{14.2}{13.56}\right)^2 \approx 2665\text{ pF}$$

In order for this calculation to be valid, it is required to know which resonant peak is due to loop 2 and which is due to loop 3. This may be accomplished by physically moving the loop and noting which peak shifts, or by trial and error.

2.2.2 Tunable Impedance Matching with Varactors

The method of optimization of the four coil WPT system involved transformation of the load impedance to its optimal value. It was discovered that this transformation

depends on coupling coefficient, which in turn, depends on separation between the coils. Hence, the system performance is a function of the distance between the coils. This may be good in some applications, but not for long-term biomedical implants.

It is unreasonable to assume that a rat fitted with an implant will maintain a certain distance to the external power transmitter. This means that if a four coil system is used, coupling coefficient K_{23} will vary with time as the rat moves through its environment. The optimal coupling between the other two pairs of coils, K_{12}^{opt} and K_{34}^{opt}, were found to be functions of K_{23}. So, in order to account for a varying K_{23}, the distance between the primary coils and the distance between the secondary coils must change with time.

In some applications in may be valid to use some form of actuator to physically move the coils closer and farther apart. But, that is difficult to do in the realm of an implantable unit. Therefore, an alternative method is theorized here that uses a variable Π-matching network to transform the load impedance to its optimal value as a function of the a capacitance used in the network.

When this capacitance is made variable through the use of a varactor, it may be possible to achieve optimal power transfer as a funciton of the varactor bias rather than distance.

A varactor is a type of diode whose equivalent capacitance is a funciton of the reverse voltage applied to the diode. Applying a small reverse voltage creates a small depletion region. As the reverse voltage is increased, the depletion region increases, which decreases the capacitance. Thus, varactor capacitance decreases as reverse voltage is applied. Varactor diodes are used as a variable capacitors in circuits that require tuning, such as in voltage controlled oscillators. The downside to using these devices is that they must be biased such that they do not begin to conduct in the forward direction, which requires the use of at least one additional inductor and capacitor, as shown in Figure 2.10.

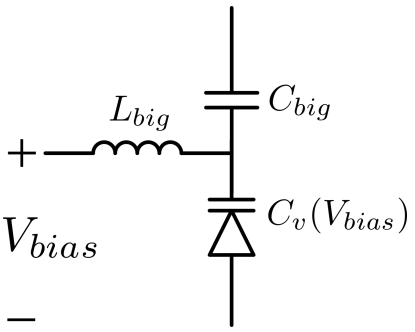

Figure 2.10: A typical method of applying a DC bias for a tunable capacitor.

The proposed matching network topology is a simple Π-matching network shown in Figure 2.11. This network replaces the fourth coil from the four coil WPT scheme with an inductor, capacitor, and variable capacitor. The design of the network is the same as for any Π-match, and follows the method presented in the introduction of this work with one small change.

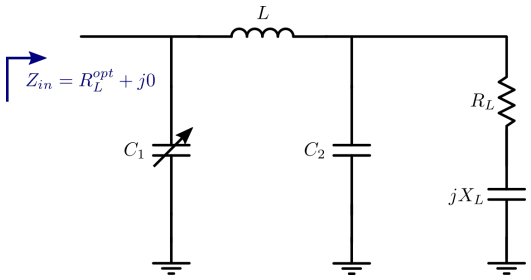

Figure 2.11: A Π-match network proposed to allow for dynamic adjustment of power transfer.

The input impedance of the rectifier section is considered to be the load impedance that needs to be transformed. This impedance typically has a small real part and large, negative imaginary part. Depending on the magnitude of negative reactance, it may be desirable to cancel a portion of this reactance to make the remainder of the matching network physically realizable. Cancellation may be accomplished by adding a series inductor before the rectifier.

Thus there are two steps that needed to be added in the design of the Π-matching network. First, the load impedance becomes $Z_{L,eff} = R_L + R_{offset} + j(\omega_0 L_{offset} - |X_L|)$. So the effective load quality factor is $Q_L = \frac{|X_{L,eff}|}{R_{L,eff}}$. Then the effective load must

transformed from series to parallel using its quality factor. Hence, $R_2 = (1+Q_L^2)R_{L,eff}$ and $X_2 = \frac{1+Q_L^2}{Q_L^2}X_{L,eff}$. The matching network requires a parallel capacitor before the load, part of which is contributed by the capacitance of the load itself. Hence this capacitance will add in parallel with the added capacitor. The equivalent capacitance added by the load is then $C_2' = \frac{1}{\omega_0|X_2|}$. At this point, the analysis follows the normal analysis for a Π-match network.

The varactor capacitance as a function of applied reverse voltage is given as (2.43) [68].

$$C_v(V_r) = \frac{C_0}{\left(1 - \frac{V_r}{\phi}\right)^{\frac{1}{n}}} \tag{2.43}$$

A block diagram of the proposed reconfigurable impedance matching network, realized as a Π-configuration, may be observed in Figure 2.12. The microcontroller programatically adjusts the reverse varactor voltage by outputting a PWM waveform. This waveform is low-pass filtered such that the output is a DC value proportional to the PWM duty cycle.

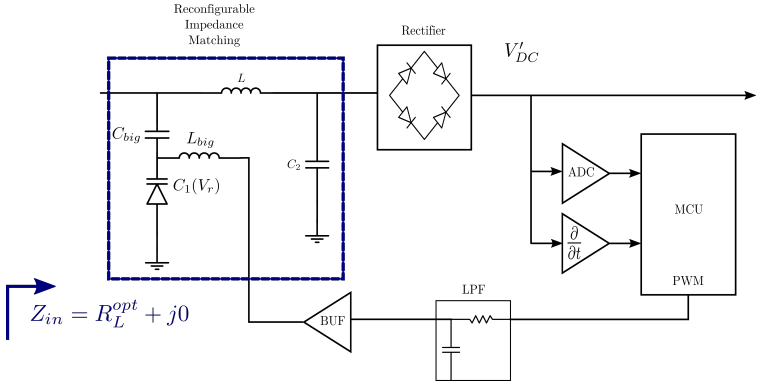

Figure 2.12: The proposed programmable Π-matching network.

There is a microcontroller responsible for dynamically adjusting the reverse varactor voltage. The control algorithm used by this controller may be observed in Figure 2.13. It is similar to that used in the maximum efficiency point tracking system from [65]. The control works as follows:

The varactor voltage is adjusted. The resulting change in rectified voltage is sampled. If this voltage is larger than the previous iteration, the efficiency must have improved due to improved matching. Conversely, if the rectified voltage decreases, the efficiency decreased so the direction of voltage change must be reversed. After a certain number of iterations, it is time to send power data back to the primary side. This allows the power amplifier to alter the power being input to the inductive link.

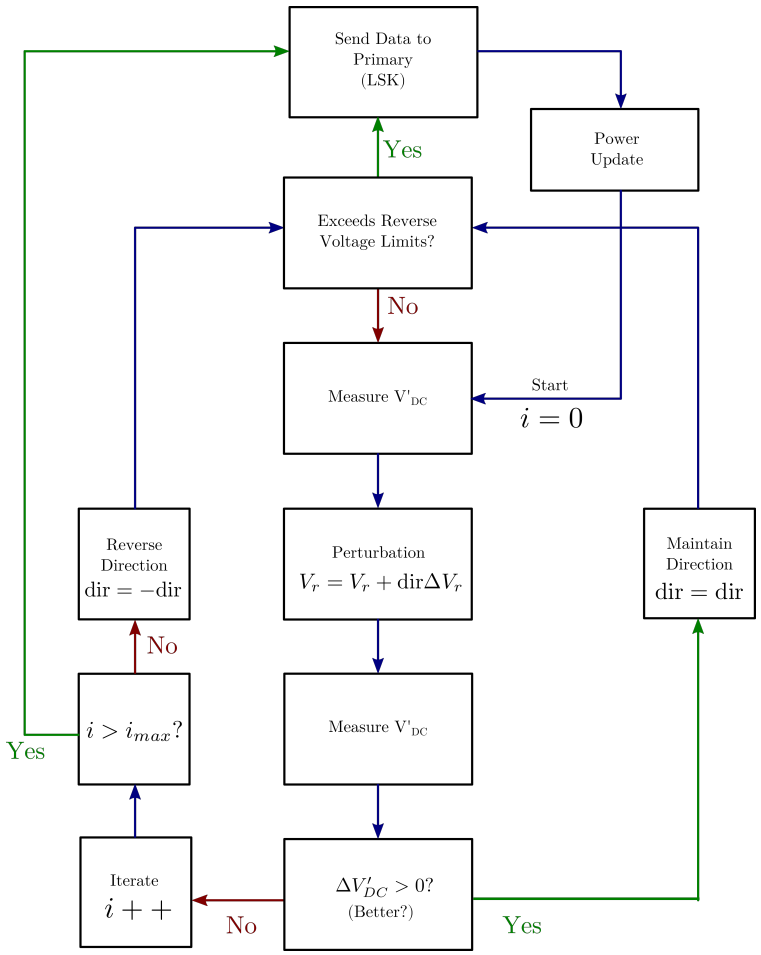

Figure 2.13: The software algorithm used to programatically tune the impedance matching network.

CHAPTER 3: ADDITIONAL SYSTEM CIRCUITRY ANALYSIS AND DESIGN

The circuitry analyzed and discussed in this work closely mirrors that of [11]. Variations are made in the design to more suitably adapt it for this application, as well as to improve upon it, where able. The system architecture is broken down into sub-circuit blocks that are each discussed in detail in the following sections.

.

3.1 Class-E Power Amplifier

The class E power amplifier is a convenient circuit used to develop the required input power for an inductive link. This topology is superior to other types of amplifiers due to its high efficiency and ability to drive inductive loads. In theory, a class E amplifier can achieve 100% efficiency, unlike many other types that are not 100% efficient even in the ideal case. For example, the class A amplifier's theoretical efficiency is only 50%. In practice, class E typically exhibits $> 90\%$ efficiency.

High efficiency is attainable for this topology because of its ability to attain zero-voltage switching. Idealistic switch waveforms may be observed in Figure 3.1. Switching power losses are given by the product of current and voltage $P_{loss} = I_{sw}V_{sw}$. From the ideal waveforms, it is apparent that this loss is zero since the waveforms do not overlap, hence achieving 100% efficiency.

The fundamentals of class E amplifiers has been well established in the literature. This section reviews the design theory of these circuits based on the theory presented in [69].

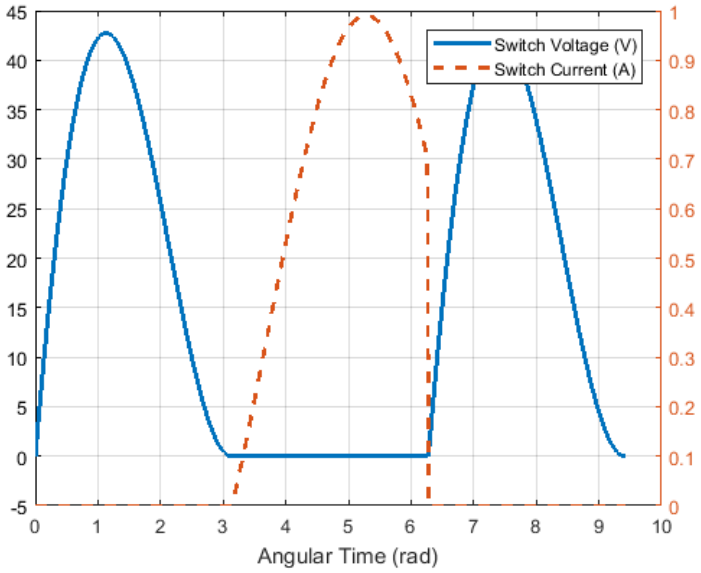

Figure 3.1: Class E idealistic switch voltage and current waveforms, confirming zero voltage switching nature.

3.1.1 Basic Equations

For the following power amplifier analysis, time is expressed in angular units for convenience, as given by (3.1).

$$\theta = \omega t \tag{3.1}$$

In order to utilize this definition, it is necessary to define derivatives with respect to angular time (3.2).

$$\begin{aligned} \frac{\partial \theta}{\partial t} &= \omega \\ \frac{\partial}{\partial t} &= \frac{\partial}{\partial \theta} \cdot \frac{\partial \theta}{\partial t} = \omega \frac{\partial}{\partial \theta} \end{aligned} \tag{3.2}$$

With the definition of derivative, it is now possible to define the voltage across an

inductor and current through a capacitor using (3.3), (3.4).

$$v_L(\theta) = \omega L \frac{\partial i_L}{\partial \theta} \tag{3.3}$$

$$i_C(\theta) = \omega C \frac{\partial v_C}{\partial \theta} \tag{3.4}$$

The power amplifier circuit may be observed in Figure 3.2.

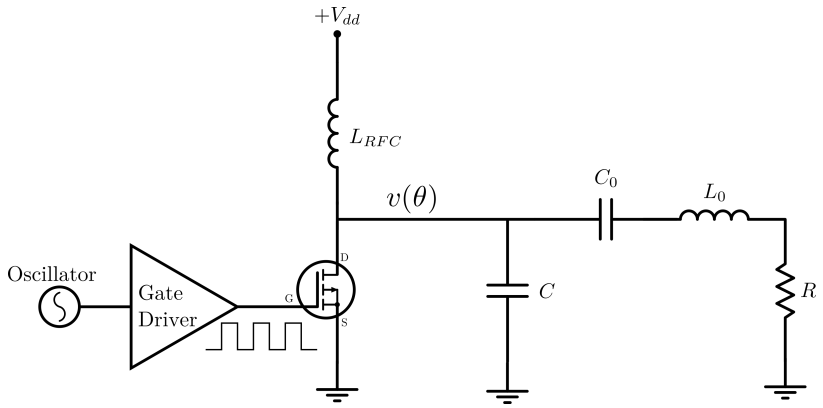

Figure 3.2: The schematic of a class E RF power amplifier using an N-channel MOSFET to approximate the ideal switch.

The output current and voltage are desired to be purely sinusoidal, therefore their forms are assumed as such. The definition of output voltage and current are then given by (3.5), (3.6).

$$v_{out} = v_{0pk} \sin(\theta + \phi) \tag{3.5}$$

$$i_{out} = \frac{v_{0pk}}{R} \sin(\theta + \phi) \tag{3.6}$$

The voltage across the switch and shunt capacitor is given by (3.7)

$$v(\theta) = \frac{1}{\omega C} \int_{\theta_0}^{\theta} i_c(u) du \tag{3.7}$$

where i_c is the current flowing through the shunt capacitor which may be expressed

from a KCL at the drain node (3.8) when the switch is open. Note that the current through the switch is assumed to be zero since the switch is open. In reality, the switch is implemented with a transistor that will have some leakage current.

$$I_{dc} = i_c + i_{out} \tag{3.8}$$

Using this KCL allows the evaluation of (3.7), as given by (3.9). This definiton of the voltage across the switch is only valid while the switch is open, on $\frac{\pi}{2} - y \leq \theta \leq \frac{\pi}{2} + y$. When the switch is closed, the voltage across it is ideally zero.

$$\begin{aligned} v(\theta) &= \frac{1}{\omega C}\int_{\theta_0}^{\theta} I_{dc} - \frac{v_{0pk}}{R}\sin(u+\phi)du \\ &= \frac{1}{\omega C}\left(I_{dc}u + \frac{v_{0pk}}{R}\cos(u+\phi)\right)\Bigg|_{u=\pi/2-y}^{\theta} \\ &= \frac{1}{\omega C}\left(I_{dc}\theta + \frac{v_{0pk}}{R}\cos(\theta+\phi) - I_{dc}\left(\frac{\pi}{2}-y\right) - \frac{v_{0pk}}{R}\cos\left(\frac{\pi}{2}-y+\phi\right)\right) \\ &= \frac{I_{dc}}{\omega C}\left[\theta + y - \frac{\pi}{2} + \frac{v_{0pk}}{I_{dc}R}\Big(\cos(\theta+\phi) + \sin\left(\phi - y\right)\Big)\right] \end{aligned} \tag{3.9}$$

The phasor form of the output voltage (3.5) is given by (3.10).

$$\mathcal{F}\{v_{0pk}\sin(\theta+\phi)\} = -V_0 j e^{j\phi} \tag{3.10}$$

In order for the output voltage to exist as described by (3.5), the voltage across the switch must have a component at the same frequency. Therefore by voltage division, the fundamental frequency component of the switch voltage is given as (3.11).

$$\begin{aligned} -V_0 j e^{j\phi} &= \frac{R}{R+jX}V_1 \\ V_1 &= -V_0 j e^{j\phi}\left(1 + j\frac{X}{R}\right) \end{aligned} \tag{3.11}$$

The time domain equivalent is given as (3.12).

$$\begin{aligned} v_1(\theta) &= \mathrm{Re}\left\{V_1 e^{j\theta}\right\} = v_{0pk}\sin(\theta+\phi) + \frac{v_{0pk}X}{R}\cos(\theta+\phi) \\ &= v_{1pk}\sin(\theta+\phi+\psi) \end{aligned} \tag{3.12}$$

where

$$\begin{aligned} v_{1pk} &= v_{0pk}\sqrt{1+\frac{X^2}{R^2}} \\ \psi &= \mathrm{Tan}^{-1}\left(\frac{X}{R}\right) \end{aligned} \tag{3.13}$$

3.1.2 Fourier Analysis

From Fourier analysis, it is well known that a general periodic signal may be written as a linear combination of all harmonics of the fundamental frequency. This is given in equation form as (3.14).

$$f(t) = \frac{a_0}{2} + \sum_{n=1}^{\infty} a_n\cos(n\omega_0 t) + b_n\sin(n\omega_0 t) \tag{3.14}$$

The Fourier coefficients may be calculated using (3.15) – (3.17).

$$a_0 = \frac{2}{T}\int_{t_0}^{t_0+T} f(t)dt \tag{3.15}$$

$$a_n = \frac{2}{T}\int_{t_0}^{t_0+T} f(t)\cos\left(\frac{2\pi n}{T}t\right)dt \quad n = 1,2,3,\cdots \tag{3.16}$$

$$b_n = \frac{2}{T}\int_{t_0}^{t_0+T} f(t)\sin\left(\frac{2\pi n}{T}t\right)dt \quad n = 1,2,3,\cdots \tag{3.17}$$

Since the voltage across the switch is periodic, it also has a Fourier representation. The amplifier being designed is defined to have an output voltage that is purely odd

with respect to ϕ, as explicitly stated using the sine notation. Therefore its even fundamental frequency component Fourier coefficient is zero (i.e. $a_n|_{n=1} = 0$) (3.19), while its odd fundamental frequency component Fourier coefficient is equal to the amplitude of $v_1(\theta)$ (i.e. $b_n|_{n=1} = v_{1pk}$) (3.20). Furthermore, since there is no DC drop across the RF choke inductor, the DC component of the drain voltage is equal to the supply voltage (i.e. $\frac{a_0}{2} = V_{cc}$) (3.18).

$$a_0 = \frac{1}{\pi}\int_0^{2\pi} v(\theta)d\theta = 2V_{cc} \tag{3.18}$$

$$a_1 = \frac{1}{\pi}\int_0^{2\pi} v(\theta)\cos(\theta+\phi+\psi)d\theta = 0 \tag{3.19}$$

$$b_1 = \frac{1}{\pi}\int_0^{2\pi} v(\theta)\sin(\theta+\phi+\psi)d\theta = v_{1pk} \tag{3.20}$$

Since the switch voltage is only nonzero between times $\theta = \pi/2 - y$ and $\theta = \pi/2 + y$, the integrals (3.18) – (3.20) are evaluated only between these times. The latter integrals (3.19) and (3.20) may be solved using the generic (3.21). Note that in the generic integral, the constants a, b, and c are simply placeholders and are not related to Fourier coefficients.

$$\begin{aligned}\int_{\pi/2-y}^{\pi/2+y} \Big(ax + b\cos(x+\phi) + c\Big)\cos(x+\alpha)dx = \\ -\pi a\sin(\alpha)\sin(y) + 2a\cos(\alpha)\left(y\cos(y) - \sin(y)\right) + \\ by\cos(\phi-\alpha) - \frac{1}{2}b\sin(2y)\cos(\phi+\alpha) - 2c\sin(\alpha)\sin(y)\end{aligned} \tag{3.21}$$

where,

$$\begin{aligned} a &= \frac{I_{dc}}{\omega C} \\ b &= \frac{v_{0pk}}{\omega RC} \\ c &= a\,(y - \pi/2) + b\sin(\phi - y) \\ y &= \pi(1 - D) \end{aligned} \tag{3.22}$$

3.1.3 Solving for v_{0pk}

Letting $\alpha = \phi + \psi$ allows a solution for (3.19) to be obtained. Using the defined expression for the constant c, the integral solution gives (3.23).

$$\begin{aligned} 0 = -a\sin\alpha\sin y\left(\pi + 2\left(y - \frac{\pi}{2}\right)\right) + 2a\cos\alpha\,(y\cos y - \sin y) \\ + by\cos(\phi - \alpha) - \frac{1}{2}b\sin(2y)\cos(\phi + \alpha) \\ - 2b\sin(\phi - y)\sin\alpha\sin y \end{aligned} \tag{3.23}$$

Collecting terms involving a and b gives:

$$\begin{aligned} b\left[y\cos(\phi - \alpha) - \frac{1}{2}\sin(2y)\cos(\phi + \alpha) - 2\sin(\phi - y)\sin\alpha\sin y\right] \\ = 2ay\sin\alpha\sin y - 2a\cos\alpha\,(y\cos y - \sin y) \end{aligned} \tag{3.24}$$

Solving for b gives:

$$b = a\frac{2y\sin\alpha\sin y - 2\cos\alpha\,(y\cos y - \sin y)}{y\cos(\phi - \alpha) - \frac{1}{2}\sin(2y)\cos(\phi + \alpha) - 2\sin(\phi - y)\sin\alpha\sin y} \tag{3.25}$$

Plugging in the expressions for a and b gives a solution for v_{0pk} in terms of DC current, component values and duty cycle.

$$\begin{aligned} v_{0pk} &= I_{dc}R\frac{2y\sin\alpha\sin y - 2\cos\alpha\,(y\cos y - \sin y)}{y\cos(\phi-\alpha) - \frac{1}{2}\sin(2y)\cos(\phi+\alpha) - 2\sin(\phi-y)\sin\alpha\sin y} \\ &= I_{dc}Rg \end{aligned} \tag{3.26}$$

Revisiting the definitions of the constant b:

$$b = \frac{v_{0pk}}{\omega RC} = \frac{I_{dc}Rg}{\omega RC} = ag$$

3.1.4 Solving for v_{1pk}

A similar analysis may be performed using (3.20) by setting the odd fundamental frequency Fourier coefficient equal to the peak voltage from (3.12). Since sine and cosine are cofunctions, (3.21) may also be used to solve (3.20) with $\alpha = \phi + \psi - \pi/2$. However, this analysis does not provide any new information, so it is left out.

3.1.5 Solving for V_{cc}

The expression for switch voltage (3.9) may be rewritten to incorporate g and is given by (3.27).

$$v(\theta) = \frac{I_{dc}}{\omega C}\left[\theta + y - \frac{\pi}{2} + g\Big(\cos(\theta+\phi) + \sin(\phi - y)\Big)\right] \tag{3.27}$$

Applying (3.18) gives a relationship between the supply voltage and DC current, which is expressed as (3.28).

$$
\begin{aligned}
V_{cc} &= \frac{1}{2\pi}\int_0^{2\pi} v(\theta)d\theta \\
&= \frac{I_{dc}}{2\pi\omega C}\int_{\pi/2-y}^{\pi/2+y} \theta + g\cos(\theta+\phi) + \left[y - \frac{\pi}{2} + g\sin(\phi-y)\right] d\theta \\
&= \frac{I_{dc}}{2\pi\omega C}\left[\frac{1}{2}\theta^2 + g\sin(\theta+\phi) + \left[y - \frac{\pi}{2} + g\sin(\phi-y)\right]\theta\right]\Bigg|_{\pi/2-y}^{\pi/2+y} \\
&= \frac{I_{dc}}{2\pi\omega C}\left[\pi y + g\cos(\phi+y) - g\cos(\phi-y) + \left[y - \frac{\pi}{2} + g\sin(\phi-y)\right] 2y\right] \\
&= I_{dc}\left(\frac{1}{\pi\omega C}\right)\left(y^2 + yg\sin(\phi-y) - g\sin(y)\sin\phi\right) \\
&= I_{dc}R_{dc}
\end{aligned} \tag{3.28}
$$

3.1.6 Determination of the Phase Angle ϕ

For 100% efficency, the voltage at switching instant should be zero. Therefore, setting the voltage to zero allows a value for g to be obtained (3.29), provided a value of ϕ and duty cycle are given.

$$
\begin{aligned}
0 = v(\theta)|_{\theta=\pi/2+y} &= \frac{I_{dc}}{\omega C}\left(2y + g\cos(\pi/2+y+\phi) + g\sin\left(\phi-y\right)\right) \\
&= \frac{I_{dc}}{\omega C}\left(2y - g\sin(\phi+y) + g\sin\left(\phi-y\right)\right) \\
&= \frac{2I_{dc}}{\omega C}\left(y - g\cos\phi\sin(y)\right)
\end{aligned}
$$

Setting this voltage equal to zero gives the optimal value for g as (3.29).

$$
g = \frac{y}{\cos\phi\sin(y)} \tag{3.29}
$$

Another parameter to be defined is the normalized slope of the drain voltage, denoted ζ and given by (3.30). Typically, a smooth transition to zero volts is desired, therefore a value of $\zeta = 0$ is usually chosen, though not required.

$$\begin{aligned}\zeta &= \frac{1}{V_{cc}}\frac{\partial v(\theta)}{\partial \theta}\bigg|_{\theta=\pi/2+y} \\ &= \frac{1}{\omega R_{dc} C}\left[1 - g\sin(\pi/2 + y + \phi)\right] \\ &= \frac{1}{\omega R_{dc} C}\left[1 - g\cos(\phi + y)\right]\end{aligned}$$

Since the capacitance C is still unknown, (3.28) is used to substitute an expression for $\omega R_{dc} C$. ζ then becomes (3.30).

$$\zeta = \frac{\pi\left[1 - g(\cos\phi\cos y - \sin\phi\sin y)\right]}{y^2 + yg\sin(\phi - y) - g\sin(y)\sin\phi} \tag{3.30}$$

After some manipulation, it is possible to isolate the $\sin\phi$ and $\cos\phi$ terms, resulting in (3.31).

$$\begin{aligned}&[\zeta y\cos y - (\zeta + \pi)\sin y]\sin\phi \\ &\qquad + [\pi\cos y - \zeta y\sin y]\cos\phi = \frac{\pi - \zeta y^2}{g}\end{aligned} \tag{3.31}$$

Since g depends on ϕ, it is replaced with its definition from (3.29).

$$\begin{aligned}&[\zeta y\cos y - (\zeta + \pi)\sin y]\sin\phi \\ &\qquad + [\pi\cos y - \zeta y\sin y]\cos\phi = \frac{\pi - \zeta y^2}{y}\sin y\cos\phi\end{aligned} \tag{3.32}$$

Dividing both sides by $\cos\phi$ allows a solution for ϕ to be obtained as (3.33).

$$\tan\phi = \frac{\frac{\sin y}{y} - \cos y}{\frac{\zeta}{\pi} y\cos y - \left(1 + \frac{\zeta}{\pi}\right)\sin y} \tag{3.33}$$

The special case when the normalized slope of the drain voltage is zero gives (3.34).

$$\tan\phi\Big|_{\zeta=0} = \cot y - \frac{1}{y} \tag{3.34}$$

3.1.7 Determination of Component Values

The output power dissipated by the real load R is given by (3.35).

$$\begin{aligned} P_{out} &= \frac{1}{2}\frac{v_{0pk}^2}{R} \\ &= \frac{I_{dc}^2 R^2 g^2}{2R} \\ &= \frac{R}{2}\left(\frac{gV_{cc}}{R_{dc}}\right)^2 \end{aligned} \tag{3.35}$$

The input power delivered by the DC power supply is given by (3.36).

$$P_{in} = \frac{V_{cc}^2}{R_{dc}} \tag{3.36}$$

The efficiency of the power amplifier is defined as the ratio of output power to input power, expressed as (3.37).

$$\begin{aligned} \eta &= \frac{P_{out}}{P_{in}} \\ &= \frac{g^2}{2}\frac{R}{R_{dc}} \end{aligned} \tag{3.37}$$

For 100% efficency, $\eta = 1$ and R_{dc} is given by (3.38).

$$R_{dc} = \frac{g^2}{2}R \tag{3.38}$$

From (3.28), the total capacitance in parallel with the switch (including switch parasitics) is given by (3.39).

$$C = \left(\frac{2}{g^2 \pi \omega R}\right)\left(y^2 + yg\sin(\phi - y) - g\sin(y)\sin\phi\right) \tag{3.39}$$

In order to find the values of series resonant circuit formed by L_0 and C_0, the value of the reactance term X must be found. In order to find X, the phase angle ψ must first be found which relates to X by (3.13). ψ may be found by setting (3.21) to zero and expanding the terms invloving α, yielding (3.40).

$$\begin{aligned} 0 = &-(\pi a + 2c)\sin(y)\sin(\alpha) + 2a\left[y\cos y - \sin y\right]\cos(\alpha) \\ &- \frac{1}{2}b\sin(2y)[\cos\phi\cos\alpha - \sin\phi\sin\alpha] \\ &+ by[\cos\phi\cos\alpha + \sin\phi\sin\alpha] \end{aligned} \tag{3.40}$$

Isolating the α terms allows the equation to be solved by dividing out the cosine, leaving behind a tangent (3.41).

$$\begin{aligned} \tan\alpha &= \frac{(\sin(2y) - 2y)\, b\cos\phi - 4a(y\cos y - \sin y)}{(\sin(2y) + 2y)\, b\sin\phi - 2(\pi a + 2c)\sin y} \\ &= \frac{(\sin(2y) - 2y)\, b\cos\phi - 4a(y\cos y - \sin y)}{(\sin(2y) + 2y)\, b\sin\phi - 2(2ay + 2b\sin(\phi - y))\sin y} \\ &= \frac{(\sin(2y) - 2y)\, ag\cos\phi - 4a(y\cos y - \sin y)}{(\sin(2y) + 2y)\, ag\sin\phi - 4a(y + g\sin(\phi - y))\sin y} \end{aligned} \tag{3.41}$$

But α is a parameter that was defined for convenience. Substituting its expression yields (3.42). The righthand side of this equation is lumped into the parameter h.

$$\tan(\phi+\psi) = \frac{(\sin(2y)-2y)\, g\cos\phi - 4(y\cos y - \sin y)}{(\sin(2y)+2y)\, g\sin\phi - 4(y + g\sin(\phi - y))\sin y} = h \tag{3.42}$$

Then ψ may be found as (3.43) by taking the inverse tangent of both sides of (3.42).

$$\psi = \mathrm{Tan}^{-1}(h) - \phi \tag{3.43}$$

Since the equation relating X and R involves a $\tan\psi$, it makes sense to take the tangent of the solution for ψ.

$$\tan\psi = \tan\left(\mathrm{Tan}^{-1}(h) - \phi\right) = \frac{h - \tan\phi}{1 + h\tan\phi} \tag{3.44}$$

$$X = R\tan\psi = R\frac{h - \tan\phi}{1 + h\tan\phi} \tag{3.45}$$

Recall that X is defined as the series reactance of L_0 and C_0. Then a value for C_0 may be obtained using (3.46) given a particular inductor value L_0.

$$\begin{aligned} X &= \omega L_0 - \frac{1}{\omega C_0} \\ \frac{1}{\omega C_0} &= \omega L_0 - X \\ C_0 &= \frac{1}{\omega^2 L_0 - \omega X} \end{aligned} \tag{3.46}$$

Assuming a positive reactance X leads to a constraint on L_0 such that C_0 remains positive. In the event that $X < 0$, any positive value of L_0 will result in a positive value for C_0.

$$L_0 > \frac{X}{\omega} \tag{3.47}$$

The design of the amplifier component values is independent of the supply voltage, however the output power increases with increasing supply voltage. Therefore, the amplifier may be used to deliver variable amounts of power by varying only the supply voltage!

3.1.8 Non-ideal Switches

The presented class E analysis assumes a perfect switch. Here, "perfect" refers to the following:

1. Zero ON-state voltage
2. Zero ON-state resistance
3. Infinite OFF-state resistance
4. Zero switching time

In practice, a transistor is used to approximate a perfect switch, but in reality do not meet any of the idealized switch parameters. The non-ideal nature of transistors is explored in more detail in [70] and [71].

In [72], the switching characteristics of Gallium-Nitride field effect transistors is evaluated and determined to be a good transistor choice for power switching applications where the frequency is greater than 1 MHz.

3.2 Rectifier Circuitry

As previously discussed, it is required to use alternating current for wireless power transfer in order for currents to be induced in the secondary coils. However, for the application of biomedical implants, the purpose of delivering power is to supply data acquisition and transmission circuits with DC power. Therefore, it is necessary to have an intermediate sub-circuit whose role is to convert the RF power to DC power.

RF-to-DC conversion may be accomplished by a number of simple circuits consisting of simple diodes and capacitors. One such circuit is the standard full-wave rectifier as

shown in Figure 3.3. Since the output of a full-wave rectifier is lower than its input voltage by two diode voltage drops, choosing didoes that have intrinsically low forward voltages is preferred for efficiency. Each diode in the rectifier is therefore chosen to be a Schottkey diode for its low forward voltage drop.

Voltage rectifier theory is discussed in [73] and may be used as a guide in understanding how these circuits operate.

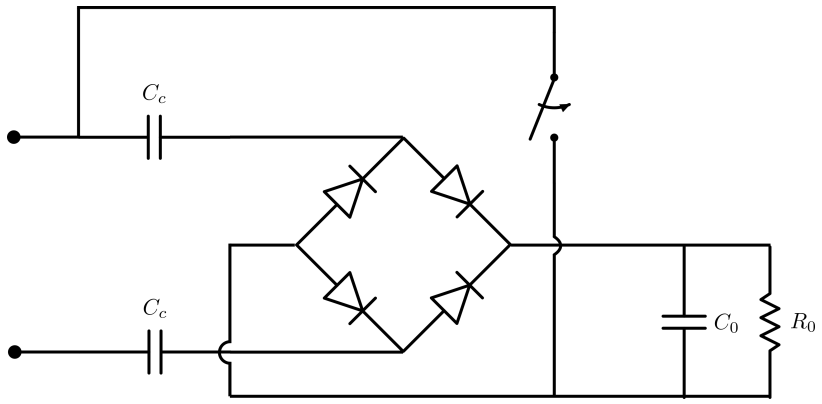

Figure 3.3: Full-wave rectifier topology for RF-to-DC-conversion within the receiver architecture

The AC-to-DC conversions ratio is defined as the ratio between average value of current to the root mean square (RMS) of the current through the rectifier. For a half-wave rectifier, the conversion ratio is (3.48).

3.2.1 Half-Wave Rectifier

A half wave rectifier consists of a single diode and capacitor pair. It allows current to flow in the forward direction once the voltage across the diode exceeds its forward voltage, and blocks current when the diode is reverse biased. In this way, the topology passes the positive half-cycle of a sine wave and rejects the negative half-cycle, earning its name as a half-wave rectifier. The role of the capacitor is to hold the voltage approximately constant while the negative half-cycle is blocked, such that the output does not drop to zero.

The conversion efficiency of a rectifier is defined as the ratio between rectified DC

current and RMS input AC current. The half-wave conversion efficiency is given by (3.48).

$$\frac{DC}{AC} = \frac{\frac{1}{2\pi}\int_0^{2\pi} I(\theta)d\theta}{\sqrt{\frac{1}{2\pi}\int_0^{2\pi} I^2(\theta)d\theta}} = \frac{\frac{1}{2\pi}\int_0^{\pi} I_{pk}\sin\theta d\theta}{\sqrt{\frac{1}{2\pi}\int_0^{\pi} I_{pk}^2\sin^2\theta d\theta}} = \frac{2}{\pi} \tag{3.48}$$

If the input of a half-wave rectifier is driven by a sine wave of amplitude V_{pk}, its output DC voltage is given by (3.49) [74].

$$V_{DC} = V_{pk}\left\{1 - \frac{\ln\alpha}{2\alpha} - \epsilon\sqrt{\frac{\pi}{8}}\left[\sqrt{2\pi}(\lambda+1) - \lambda\right]\right\} \tag{3.49}$$

The output voltage is not totally time independent, having some small AC ripple voltage. This ripple may be expressed as (3.50).

$$V_{AC} = \frac{\epsilon V_{pk}\lambda}{\sqrt{2\pi}}\left[\frac{\pi}{2} - t + 2\text{erf}\left(\frac{\sqrt{\alpha}}{2}\left[t - \frac{\pi}{2}\right]\right)\right] \tag{3.50}$$

For each of the two voltage expressions (3.49) and (3.50), the following substitutions have been made for clarity:

$$\begin{aligned} \alpha &= \frac{q}{kT}V_{pk} \\ \epsilon &= \frac{1}{\omega RC} \\ \lambda &= \frac{I_{pk}R}{V_{pk}} \\ \text{erf}(t) &= \frac{2}{\sqrt{\pi}}\int_0^t e^{-x^2}dx \end{aligned} \tag{3.51}$$

3.2.2 Full-Wave Rectifier

In order to achieve higher conversion efficiency than the half-wave rectifier, a full-wave rectifying topology may be created using four diodes and a capacitor, consisting of two separate circuit branches. In this way, current may conduct through one of the

two branches during both the positive and negative half-cycles.

The improved conversion efficiency is given by (3.52).

$$\frac{DC}{AC} = \frac{\frac{1}{2\pi}\int_0^{2\pi} I(\theta)d\theta}{\sqrt{\frac{1}{2\pi}\int_0^{2\pi} I^2(\theta)d\theta}} = \frac{\frac{1}{\pi}\int_0^{\pi} I_{pk}\sin\theta d\theta}{\sqrt{\frac{1}{\pi}\int_0^{\pi} I_{pk}^2\sin^2\theta d\theta}} = \frac{2\sqrt{2}}{\pi} \tag{3.52}$$

3.2.3 Greinacher Voltage Doubler

Various voltage rectifying topologies have been reviewed in [75]. From this comparison of topologies, the Greinacher voltage doubler stands out as having highest conversion efficiency. Therefore, this circuit is utilized as the rectifying circuit when dealing with data transfer through load-shift keying discussed in another section. The voltage doubler schematic may be seen in Figure 3.6.

3.3 Voltage Regulation Circuitry

It is critical to ensure that the implanted circuitry is receiving the appropriate amount of power. Too litle power will cause the stimulation and measurement circuitry to malfunction, yielding unreliable results. Too much power will cause component failure and potentially excessive tissue heating, which can be dangerous for the subject.

Voltage regulation is a crucial component to the overall system. Without regulation, the voltage could rise to dangerous levels that could harm the animal and damage the circuits that operate at low voltages.

A typical schematic for a low-dropoout regulator is provided in Figure 3.4.

Here, the FET device acts as a voltage controlled resistor whose value depends on the error signal. The error signal is the difference between the feedback voltage and a reference voltage. Thus, the regulator is constantly working to bring the feedback voltage equal to the reference voltage, thus regulating the output.

For the purposes of this research, there is no need to design an LDO since so many off-the-shelf components exist that are suitable. The primary considerations are

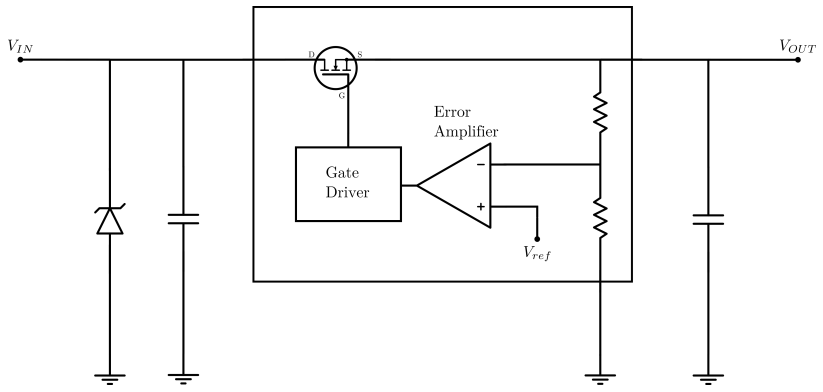

Figure 3.4: The innerworkings of a low-dropout linear voltage regulator.

3.4 Load Shift Keying

In the ever-changing environment of the scope of this project, voltage regulation alone cannot be relied upon to keep the system operating properly. If a voltage regulator is receiving too much voltage at its input, it burns off the excessive voltage as heat. This is not desirable in a biomedical context. Therefore, a closed loop system must be employed that seeks to alter the amount of power being delivered in order to avoid the regulators causing excessive heating in the biological tissue. By measuring the rectified voltage and sending data back to the primary side, logical systems may be put in place to adjust the amount of power being sent.

Reverse data can be encoded by inserting a switch that modifies the load. Rather than adjusting amplitude or phase of a signal as in amplitude and phase shift keying, the load is temporarily switched to a different value. This change is detected from the primary side through a current sensing inductor. Thus, information can be encoded in the changes in current sensed on the primary side.

The load switch can be implemented with an nMOS/pMOS transistor pair as depicted in Figure 3.5. Like any SPST switch, it has two states: off and on. Consider the case when the input gate drive voltage is zero. Since the applied gate-source voltage is zero, which is less than the MOSFET's nonzero threshold voltage, the transistor is off and has a large output impedance. Hence, there is very little current

through the resistor R_{switch}, and a negligable voltage drop. Then the voltage at the gate of the pMOS is the same as its source, so it too has a near zero source-gate voltage, therefore the switch is off.

Now consider the case when the nMOS gate voltage is larger than the threshold. Then current starts flowing through R_{switch}, dropping the pMOS gate voltage down to ground. As the PMOS gate voltage drops below its source voltage, it begins to conduct. Hence, current begins to flow into the load.

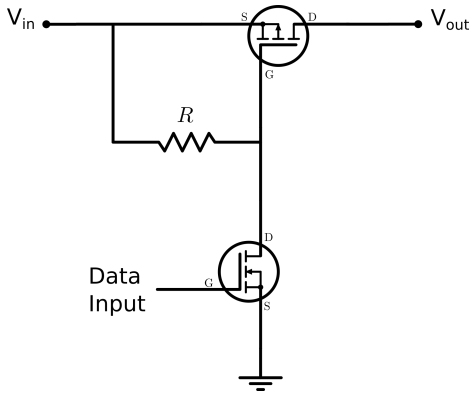

Figure 3.5: The load modulation switch topology chosen by [11].

Inductively coupled coils are sensitive to changes in loading conditions. If the load impedance changes values, the input impedance at the primary also changes. As a result, the primary voltage and current waveforms change. This is the fundamental phenomenon behind implantable biotelemetry closed loop systems that employ inductive coupling. By modulating the secondary side load, changes in primary current may be sensed and decoded as data, accomplishing telemetry.

In order to effect a change in the load, a switch may be used to temporarily short part of the secondary circuit. In order for telemetry to occur, the switch may be driven by data. Suppose the voltage across the primary coil is denoted as V_{in}. This voltage has different peak values when the modulation switch is in its on-state versus its off-state. The amplitude modulation index is then defined as (3.53).

$$m = \left| \frac{V_{in,ON} - V_{in,OFF}}{V_{in,ON} + V_{in,OFF}} \right| \tag{3.53}$$

The particular load-switching scheme presented is given in Figure 3.3 [76]. When the switch is off, the circuit is in its usual full-wave rectifier state. When the switch closes, the topology is converted to a Greinacher voltage doubler rectifier, shown in Figure 3.6. In either case, the AC power is rectified and delivered to the load, but with slightly different equivalent loading values.

When the switch is off, therefore full-wave rectifying topology, the output voltage is equal to the peak delivered voltage less two diode voltage drops. The equivalent AC resistance that dissipates the same amount of power as the DC resistance R_0 is given by (3.54).

$$\begin{aligned}
\frac{V_0^2}{R_0} &= \frac{\left(\frac{V_{pk}}{\sqrt{2}}\right)^2}{R_{ac}} \\
\frac{(V_{pk} - 2V_{diode})^2}{R_0} &= \frac{\left(\frac{V_{pk}}{\sqrt{2}}\right)^2}{R_{ac}} \\
\frac{\left(V_{pk}\left(1 - 2\frac{V_{diode}}{V_{pk}}\right)\right)^2}{R_0} &= \frac{V_{pk}^2}{2R_{ac}} \\
R_{ac,\ off} &= \frac{R_0}{2\left(1 - 2\frac{V_{diode}}{V_{pk}}\right)^2}
\end{aligned} \tag{3.54}$$

In the event that the diode drop is small relative to the peak voltage, this resistance approaches $R_0/2$. This disagrees with Zhengnian Tang *et al*[76], however it agrees with one of their citations, also cited here as [77].

When the switch is on, therefore Greinacher doubler topology, the output voltage is double the peak delivered voltage. The equivalent AC resistance that dissipates the same amount of power as the DC resistance R_0 is given by (3.55). This agrees with Zhengnian Tang *et al*.

$$\frac{V_0^2}{R_0} = \frac{\left(\frac{V_{pk}}{\sqrt{2}}\right)^2}{R_{ac}} \text{ and } V_0 = 2V_{pk} \text{ Voltage Doubler}$$
$$\frac{4}{R_0} = \frac{1}{2R_{ac}}$$
$$R_{ac,\ on} = \frac{R_0}{8} \tag{3.55}$$

Suppose that the output DC voltage is 9 V and the diode drop is 0.6 V, the off-state equivalent AC resistance is approximately 5.33 times larger than the on-state equivalent resistance, $R_{ac,\ off} = 5.33R_{ac,\ on}$. These values are far enough apart that switcing causes detectable amounts of current change in the primary coil, as desired.

An expression for efficiency is given by [76] as (3.56), however the derivation is not complete. They proceed to rewrite this equation incorrectly, leaving out an important R_{ac} term. This leads to the incorrect conclusion that finding an optimal R_{ac} is not achievable.

The actual expression for efficiency is given as (3.56), with the required R_{ac} term included as needed. The efficiency expression may be differntiated to find an optimal AC resistance.

$$\eta = \frac{k^2 Q_1 Q_2^3 R_2 R_{ac}}{(R_{ac} + Q_2^2 R_2)\left((1 + k^2 Q_1 Q_2)R_{ac} + Q_2^2 R_2\right)} \tag{3.56}$$

Setting $\frac{\partial \eta}{\partial R_{ac}} = 0$ yields the optimal solution for R_{ac} (3.57).

$$R_{ac,\ opt} = \frac{Q_2^2 R_2}{\sqrt{1 + k^2 Q_1 Q_2}} \tag{3.57}$$

Nevertheless, the authors built their circuit and subjected it to various tests for verification. The switch was implemented with a double-diffusion MOSFET (DMOS), specifically a Siliconix SD210. A CMOS inverter is used as the DMOS driver. Titanium wire was chosen as the inductor material for biocompatibility among other reasons.

The system successfully delivered 80 mW wirelessly at 8.75 MHz power carrier. A data signal was transmitted at a rate of 36 kbps. Power transfer efficiency was compared for switch always on, switch always off, and switch during modulation with similar results and best case 33%. The powering distance did not exceed 5 cm and was optimized for 2.54 cm. Modulation index was also measured versus distance and was found that the circuit was capable of correctly demodulating the signal for a lowest case index of 0.02. Similar results were obtained for modulation index when the coils were offset laterally by 2 cm. For angles between $\pm 60°$, pitch angle between coils did not have an impact on modulation index or transfer efficiency. The data frequency did not have a significant impact on modulation index until switching limitations were reached. Finally, the powering frequency was cited to be insignificant as it relates to tissue absorption.

Therefore, load shift keying may be achieved by temporarily converting a full-wave rectifier to a Greinacher voltage doubling rectifier, as is supported by [76]. The full-wave topology with switch placement is shown in Figure 3.3. The voltage doubling topology is shown in Figure 3.6.

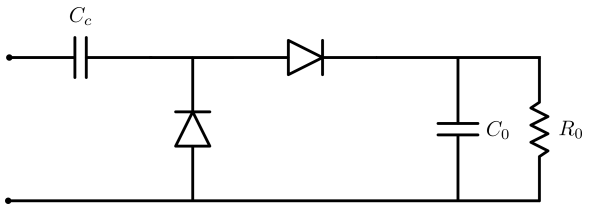

Figure 3.6: The equivalent circuit of Figure 3.3 when the switch is closed. This topology is known as a Grienacher voltage doubling rectifier.

3.4.1 Reverse Telemetry Data Protocol

The sampled rectified voltage, along with its sign bit are input to a microcontroller within the implant. The microcontroller then encodes this information using the scheme from [11]. Figure 3.7 shows a sample data stream consisting of "0101" and the switch signal that is used to realize this data stream (shown only for the middle

two bits "10").

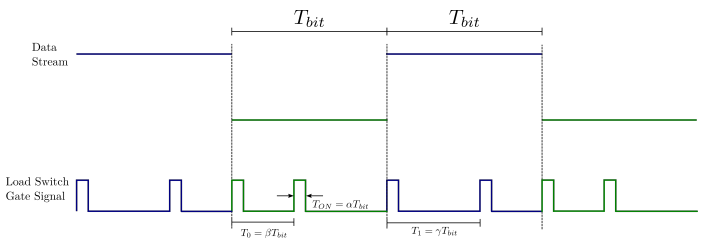

Figure 3.7: The encoding scheme similar to that used in [11], adopted for this work.

3.5 Reverse Telemetry

The load switch, discussed previously is used to send data from the implant back to the external side. In order to accomplish this, the binary data must conform to some protocol that is generated on the secondary side and decoded on the primary. For system functionality, the primary side needs knowledge of how much DC voltage is being supplied to the secondary. Then decisions may be made on whether to increase or decrease the input power.

This is accomplished by digitizing the analog voltage to a discrete value using an N-bit ADC. Additionally, the analog voltage may be differentiated to obtain a single sign bit that gives information about whether the rectified voltage is increasing or decreasing. It may also be desirable to transmit tissue impedance and temperature, which is easily obtained from the RHD2132 as 16-bit digital values. Thus, a data packet may be formed for each sample that consists of $N+1$ power bits, 16 impedance bits, 16 temperature bits, and 3 parity bits. Then the data packet consists of $N+36$ bits. Since this data is used to control the input power, dead-time is inserted as the packet prefix. The dead-time is chosen to be long enough to allow for the power update transients to settle.

If an 8-bit ADC is used, the packet contains 44 bits plus dead time. Then the packet period is given by (3.58).

$$T_{packet} = T_{dead} + 44T_{bit} \tag{3.58}$$

Choosing the packet and dead times to be 10 ms and 2 ms respectively, gives a bit period of about 180 μs. In other words, the load switch will be modulated at 5.55 kHz, corresponding to 100 power updates per second.

3.6 Power Control Unit

A closed loop system is employed in order to have dynamic power adjustment for physical conditions that vary with time. The Class E power amplifier previously discussed has an output power that is dependent on its DC supply voltage. Conveniently, the component values are not dependent on the value of supply voltage. By controlling the supply voltage, a variable output power PA is created. For this application, there is no RF signal that needs to be amplified, therefore a switching topology is ideal since it does not have a true RF signal input, but achieves high efficiency through its switched nature.

The goal of the power control unit is simple and summarized by the block diagram in Figure 3.8. Digital data that informs about the amount of power that has been rectified is the input to this sub-system. Physically, this data comes in the form of current pulses that are sensed by an inductor. These pulses are conditioned from tiny jagged spikes to a larger, squared off signal that is input to a microcontroller. The microcontroller applies the packet protocol to incoming signal to determine if the pulses are digital 1's or 0's. Once the entire packet is in, it double checks to ensure the signal was not received in error. Using this information, the microcontroller applies an algorithm to determine whether the supply voltage needs to increase or decrease and encodes this as a data word. This data word is then queued using the appropriate protocol of the DAC and then sent to the DAC. The output of the DAC is an analog current that feeds into a DC-DC converter whose voltage depends on this current

input.

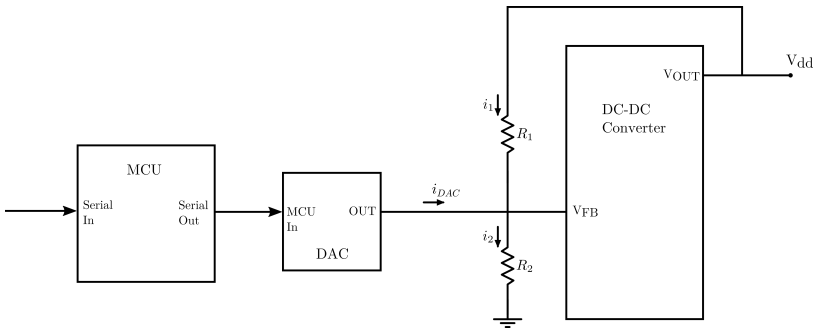

Figure 3.8: The power control unit topology showing current directions for KCL used for determining (3.61)

3.6.1 Detector

The detector is an inductor wrapped around part of the primary coil such that changes in coil current induce a small, but detectable current in the sense inductor. The induced current is converted into a voltage through a simple envelope detector comprised of a diode and capacitor. The envelope signal is then low-pass filtered to reduce any higher frequency spectral content (dominated primarily by the 13.56 MHz carrier).

3.6.2 Amplifier and Comparator

The differential filtered envelope signal is passed to a differential amplifier that boosts the signal levels to make comparison possible. The differential amplifier outputs are fed into both inputs of a comparator such that the output is high when the difference between non-inverting and inverting inputs is positive. The output of this sub-block is a series of square pulses appropriate for microcontroller input.

3.6.3 Microcontroller Decoder

The serial pulses output by the comparator do not explicitly represent 1's and 0's. That is, low does not map to zero and high does not map to one. Instead, a protocol must be used to determine the value of the data stream. This layer of abstraction

is an effort to reduce errors in transmission. The particular protocol was mentioned in the section pertaining to the load switch. An example data packet that might be encoded at the secondary and received by the decoder is shown in Figure 3.9.

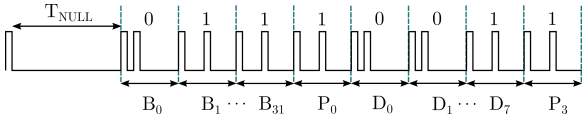

Figure 3.9: The data packet format representing a settling time, 32 bits of information, 8 bits of power data, and 4 parity bits.

Once the data packet has been received, it is checked against the parity scheme being used (even or odd). If the parity check fails, this data packet is ignored and the supply voltage is not updated. If the parity check passes, the protocol that determines how the supply voltage should be updated is applied, which generates an N-bit data word, where 'N' is the bit resolution of the digital-to-analog converter.

3.6.4 Microcontroller Encoder

The data word that has been computed is currently located in microcontroller memory. The DAC that is used will have a specific interface in which it receives data. This interface could be parallel, serial, or parallel with shift register. In parallel interfaces, all data enters the DAC at the same time. In parallel interfaces with shift registers, a sub-set of the data word enters at the same time, then the next sub-set comes in during the next clock cycle until the entire data word has been received. In serial interfaces, a protocol such as SPI or I^2C is used which determines the specifics on how the serial data should be sent. Therefore, it is the microcontroller's responsibility to ensure that it applies the protocol of the DAC to the data word.

3.6.5 Digital-to-Analog Converter

A digital-to-analog converter is used to provide a digital means of controlling the output of the DC-DC buck converter. There are many DC-DC converters that ensure regulation by feeding the output voltage back to the input through a resistive divider.

The converter is always working to bring its feedback node to a particular reference voltage. By sinking or sourcing current to the feedback node, it appears from the perspective of that node that the output voltage has changed. Therefore the IC will compensate and therefore the output voltage will change. Therefore, digital control of the supply voltage may be achieved using a digital to analog converter with current output connected to the feedback pin of a DC-DC buck down converter. Consider the circuit of Figure 3.8.

Applying KVL around the output-feedback node loop provides an expression for the output voltage (3.59). Applying KCL to the feedback node provides an expression for the current through the top feedback resistor (3.60).

$$V_{out} = V_{ref} + i_1 R_1 \tag{3.59}$$

$$i_1 = \frac{V_{ref}}{R_2} - i_{DAC} \tag{3.60}$$

Substituting (3.60) into (3.59) gives an expression for output voltage in terms of the digital-to-analog converter output. The minus sign in front of the DAC current term implies that the output voltage decreases with increasing DAC current.

$$\begin{aligned} V_{out} &= V_{ref} + \left(\frac{V_{ref}}{R_2} - i_{DAC}\right) R_1 \\ &= V_{ref}\left(1 + \frac{R_1}{R_2}\right) - i_{DAC} R_1 \end{aligned} \tag{3.61}$$

Thus the minimum output voltage occurs at maximum DAC current. Likewise, the maximum output voltage occurs at minimum DAC current. The resistor values may

be calculated by (3.62) and (3.63).

$$
\begin{aligned}
V_{min}R_2 &= V_{ref}R_1 + V_{ref}R_2 - i_{DAC,max}R_1R_2 \\
R_2 &= \frac{V_{ref}}{V_{min} - V_{ref} + i_{DAC,max}R_1}R_1 \\
V_{max} &= V_{ref} + \frac{V_{ref}R_1}{V_{ref}R_1}\left(V_{min} - V_{ref} + i_{DAC,max}R_1\right) - i_{DAC,min}R_1 \\
V_{max} &= V_{min} + \Delta i_{DAC}R_1 \\
R_1 &= \frac{\Delta V_{out}}{\Delta i_{DAC}} \qquad (3.62) \\
R_2 &= \frac{V_{ref}}{V_{min} - V_{ref}}\frac{\Delta V_{out}}{\Delta i_{DAC}} \qquad (3.63)
\end{aligned}
$$

3.6.6 DC-DC Converter

A DC-DC converter is used to control the supply voltage of the class E power amplifier and consequently the amount of power sent and ultimately received. DC-DC conversion has been extensively studied in the literature. Some converters, known as buck converters, are capable of down conversion, where the output voltage is lower than the input voltage. Other converters, known as boost converters, are capable of up conversion, where the output voltage is higher than the input voltage. There are also topologies that are a combination of buck and boost.

For this research, a down converter is used that operates from a higher DC voltage that is regulated down, where it is used as the power amplifier supply voltage.

The primary concerns for this application are output power capability and output ripple. Output power capability is a concern since all of the system power must be delivered through the converter, so it must be able to handle this power. Since DC-DC converters typically operate in a switched-mode (similar to the class E amplifier), there is an output voltage ripple at the converter's switching frequency. This is a concern because changes in primary coil current are detected and decoded as data sent from the implanted unit. If the changes in coil current are actually due to the

supply voltage ripple and not data from the implant, then non-sense data is being decoded. Therefore, care must be taken to ensure that the converter's output ripple is small enough that it does not cause current changes on the same order of magnitude as those generated by the actual data.

3.7 Neural Signal Acquisition

The RHD2132 digital electrophysiology interface chip by Intan Technologies is designed to make working with biomedical signals as simple as possible. It is selected for this research as the primary circuitry responsible for obtaining the ECoG recordings. Minimal supporting circuitry is required for proper functionality of this chip, so the overall system design is simplified by primarily focusing only on delivering power to the RHD2132. A block diagram is presented in the component's datasheet as Figure 3.10.

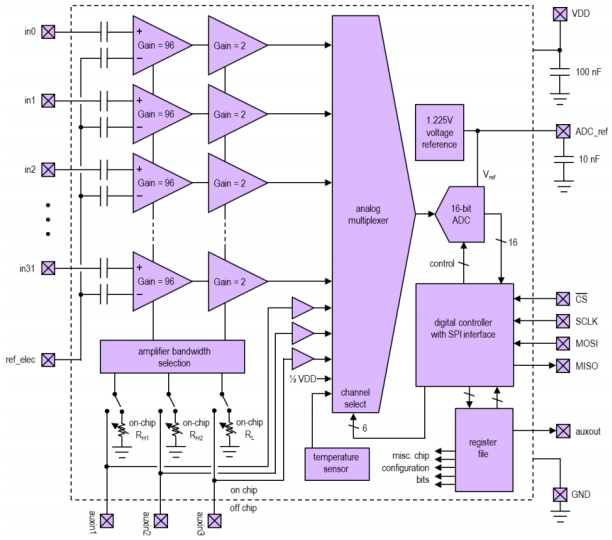

Figure 3.10: A block diagram of the Intan RHD2132 digital electrophysiology interface chip [12].

The chip interfaces directly with up to 32 electrodes and allows for the amplification and signal conditioning of the resulting neurological signals. It has an integrated analog to digital converter capable of sampling each electrode channel at 30×10^3 Samples/s. It is also capable of measuring electrode impedance and has an onboard temperature

sensor. The chip outputs serial digital data that conforms to the SPI standard, which makes communication with microcontrollers simple. Finally, it consumes a maximum of 37.3 mW worst case, and a typical 4.4 mW for ECoG applications, operating from a 3.3 V supply. For these reaons, this chip is found suitable for this research.

Sample ECoG data recorded with the RHD2132 is also provided by the datasheet as shown in Figure 3.11.

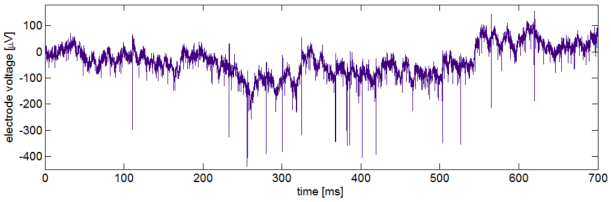

Figure 3.11: A sample of ECoG data taken using an Intan RHD2132.

CHAPTER 4: DESIGN SUMMARY AND COMPONENT SELECTION

4.1 Design Summary

In this section, discussion is given regarding the design of a particular subsystem for the more complicated subsystems. Example designs are provided for the convenience of those who may continue the project in the absence of the author.

4.1.1 Power Amplifier

The power amplifier was chosen to be a class E due to its quality of having superior efficiency and the ability to naturally drive inductive loads. A Gallium Nitride field effect transistor (GaNFET) was chosen due to its ability to switch efficiently at 13.56 MHz and being able to conduct large amounts of current.

The design steps are listed here, in order, for convenience.

1. Choose slope ζ and duty cycle D
2. Compute ϕ using (3.33)
3. Compute g using (3.29)
4. Compute h using (3.42)
5. Compute ψ using (3.44)
6. Compute C using (3.39)
7. Compute X using (3.45)
8. Ensure $L_0 > \frac{X}{\omega}$
9. Compute C_0 using (3.46)

4.1.2 Wireless Power Transfer Link

The method of wireless power delivery chosen was inductive coupling with impedance matching operating at resonance for high efficiency. The primary reason for this choice was due to being able to deliver large amounts of power over relatively large distances even with small implantable package size. Copper litz wire was chosen to increase efficiency by minimizing frequency dependent losses.

4.1.3 Example Design for Simulation

In [13], the four coil system is constrained such that all four coils are identical. In this research, it is desired to loosen that restriction such that small coils may be implanted while large coils are used externally. In this section, the equations derived in the previous sections are employed to a sample design. These sample parameters will then be given to ADS and HFSS to simulate.

4.1.3.1 Design Constraints

Let the scenario be that it is desired to transfer power over a distance of 15 cm at a frequency of 13.56 MHz. The characteristic impedance of the power source is 50 Ω. The device that is being powered has an input impedance of approximately $100 + j0\ \Omega$ near 13.56 MHz. Note that it is not necessary to have a zero imaginary part. Let a final constraint be that the load has maximum dimensions of 4cm$\times$5cm$\times$2cm.

4.1.3.2 Preliminary Design

The design is begun by choosing parameter values that are within the constraints. For the purposes of this simple example, all four coils are considered to be single turn, $N = 1$.

1. $(r_1, r_2, r_3, r_4) = (20, 20, 2, 2)$ cm
2. $(a_1, a_2, a_3, a_4) = (1, 1, 1, 1)$ mm
3. $(G_2, G_3) = (10^{-7}, 10^{-7})$ Siemens – i.e. Assume negligible capacitor loss.

4. $R'_{in} = Z_0 = 50\ \Omega$

When performing the calculation steps using these starting values, it is found that $(d_{12},\ d_{34}) = (13.88,\ 0.756)$ cm and $S_{21}|_{f=13.56\text{MHz}} = -3$ dB. It is desired to make the distances smaller and S_{21} closer to 0 dB. So the outer loop radii is changed to $(r_1,\ r_4) = (12,\ 1.6)$ cm, and the inner wire radii to $(a_2,\ a_3) = (2.9,\ 2)$ mm.

In [13], the inductance and series resistance of a circular loop are given by (4.1), (4.2).

$$L = \mu_0 r \left[\ln\left(\frac{8r}{a}\right) - 2\right] \tag{4.1}$$

$$R_s = \frac{\omega L}{Q} \tag{4.2}$$

Unfortunately, the loop quality factor, Q, is usually calculated in terms of the series resistance, not the other way around. Therefore, (4.2) is not a good way of determining the loop's series resistance. Another way of determining a wire's AC resistance is presented by Knight [78] and is summarized as (4.3)–(4.7). After experimenting with the curvefit expression, it was discovered that this indeed describes the effective wire resistance remarkably well for single stranded wires that have small (submillimeter) wire radius. For multi-stranded and/or large wire radii, the constants need to be adjusted, but that has not been explored at this time.

$$R_{acTEDML} = \frac{r^2}{\left(2r\delta_i' - \delta_i'^2\right)(1+y)} \cdot \frac{\ell}{\sigma A} \tag{4.3}$$

$$\delta_i' = \delta_i \left[1 - \exp\left(\frac{-r}{\delta_i}\right)\right] \tag{4.4}$$

$$\delta_i = \sqrt{\frac{2}{\sigma\omega\mu}} \tag{4.5}$$

$$y = \frac{0.189774}{\left(1 + 0.272481\left[z^{1.82938} - z^{-0.99457}\right]^2\right)^{1.0941}} \tag{4.6}$$

$$z = 0.62006\frac{r}{\delta_i} \tag{4.7}$$

where r is the wire radius, ℓ is the length of the wire, and A is the cross sectional wire area (usually πr^2). This formula for AC resistance will be adopted here for now.

The impedance parameters of a system composed of two coils is straightforward and is given by (4.8).

$$[\mathbf{Z}]_{2Coils} = \begin{bmatrix} R_{s1} + j\omega L_1 & -j\omega M_{12} \\ -j\omega M_{12} & R_{s2} + j\omega L_2 \end{bmatrix} \tag{4.8}$$

Therefore, $R_{s1},\ R_{s2},\ L_1,$ and L_2 may be extracted from an HFSS simulation consisting of two loops with the dimensions of loops 1 and 2. A second simulation may be performed with the dimensions of loops 3 and 4 to find their impedances.

While that is simulating, calculate the system parameters using the equations from the analysis section.

1. $(L_1,\ L_2,\ L_3,\ L_4) = (0.734,\ 1.084,\ 0.0599,\ 0.0573)\ \mu$H
   from (4.1)

2. $(R_{s1},\ R_{s2},\ R_{s3},\ R_{s4}) = (117,\ 67.0,\ 9.74,\ 15.6)$ mΩ
   from (4.3)

From the HFSS simulation, the parameters are extracted as:

1. $(L_1,\ L_2,\ L_3,\ L_4) = (0.744,\ 1.098,\ 0.0590,\ 0.0558)\ \mu$H

   We see that for the larger radii, the calculation underestimates the simulation, and for the smaller radii the opposite is true.

2. $(R_{s1},\ R_{s2},\ R_{s3},\ R_{s4}) = (136,\ 193,\ 15.0,\ 18.9)\ \text{m}\Omega$

   We see that the reistance calculation always underestimates the simulated value, but particularly so for large wire radii.

Something needs to be done about these inconsistencies.

For now, we'll continue the design using the HFSS simulated loop impedance values.

3. $(M_{23},\ K_{23}) = (2.017\ \text{nH},\ 0.00792)$

   from (2.11) and (2.12)

4. $(C_2,\ C_3) = (126.5,\ 2336)\ \text{pF}$

   from (2.27) and (2.24)

5. $(K_{12},\ K_{34}) = (0.1193,\ 0.4589)$

   from (2.26) and (2.23)

6. $(d_{12},\ d_{34}) = (8.94,\ 0.501)\ \text{cm}$

   from finding the points where a curvefit of K vs. d intersects the constants $K = K_{12}$ and $K = K_{34}$

7. $S_{21}|_{f=13.56\text{MHz}} = -2.63\ \text{dB}$

   from (2.38) in dB

4.1.4 Rectifier

Voltage rectification was achieved through a capacitively coupled full-bridge rectifier. Although this rectifier requires four large diodes, the full-bridge topology offers an attractive means of converting to a voltage doubling circuit when the load switch is active. Schottkey barrier diodes were chosen as the rectifiers for their ability to

conduct current at 13.56 MHz and having low forward voltage, which also improves efficiency.

4.1.5 Regulator

A low-dropout regulator is used for DC load regulation. It's low dropout nature minimizes voltage overhead which would result in excessive power dissipation which equates to poor efficiency, as well as potentially dangerous heating.

4.1.6 Load Switch Modulator

The design of the load switch is not complicated. The main constraint is that the switch should be able to turn fully on and back off within the designated T_{on} period. Recall that the bit period contains two short pulses, spaced by different durations to encode a "0" versus a "1". The time difference between two pulses will be referred to as T_0 for a zero bit and T_1 for a one bit. The constraint on bit periods are then given by (4.9).

$$\begin{aligned} T_{ON} &= \alpha T_{bit} \\ T_0 &= \beta T_{bit} \\ T_1 &= \gamma T_{bit} \\ 0 < \alpha &< \frac{1}{2} \\ \alpha < \beta &< 1 - \alpha \\ \beta < \gamma &< 1 - \alpha \end{aligned} \tag{4.9}$$

In this work, the on pulse period is chosen to be $T_{ON} = 0.1T_{bit}$. Zero and one periods are chosen to be $T_0 = 0.3T_{bit}$ and $T_1 = 0.7T_{bit}$. Note that it is not a requirement for $T_0 + T_1 = T_{bit}$. It is a coincidence that it occurs for the chosen periods. In order to reduce transmission errors, the zero and one periods should be far enough apart

that it is easy to distinguish between a zero and a one. For example, choosing the periods to be 62% for a zero and 63% for a one would likely result in mistakes when interpreting the bits.

The bit period is determined by the chosen packet period. It is desired for the power to be updated 100 times per second, resulting in a packet period of 10 ms. The packet consists of null period of 2 ms, 16 tissue impedance bits, 16 temperature bits, 8 power bits, 1 sign bit, and 4 parity bits.

$$T_{bit} = \frac{T_{packet} - T_{null}}{N} \tag{4.10}$$

where N is the number of bits in a packet. For this work, $T_{bit} \approx 177.78\ \mu$s, $T_0 \approx 53.33\ \mu$s, $T_1 \approx 124.44\ \mu$s, $T_{ON} = 17.77\mu$s.

4.1.7 Data Decoder

Since the data is bieng encoded in the low kHz range, the constraints on the data decoding circuitry is very relaxed and does not require any special consideration. A simple envelope detector followed by a bandpass filter will suffice. The filtered output will then be compared in order to shape the gradual signal to a sharp edged series of pulses.

4.2 Creating Software for Design

In order to aid in the design of wireless power transfer, computers should be utilized to avoid tedious number crunching. A software tool was developed using Matlab for this purpose. This software tool has also been extended to Python in effort to make it free for everyone to use. A brief description of the tool's inputs and outputs is depicted in Figure 4.1.

4.2.1 Graphical User Interface Using Matlab

From the theoretical analysis, a mathematical model has been formed which describes the design of wireless power transfer systems that consist of four inductively coupled

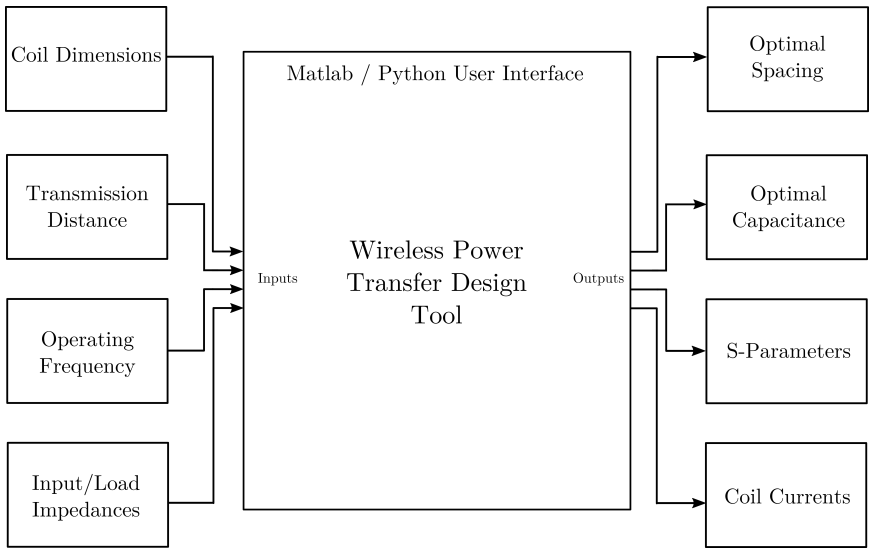

Figure 4.1: The inputs and outputs of a software design tool developed for streamlined design of inductive wireless power transfer systems.

coils of multiple sizes. Matlab was utilized to create a graphical user interface for designing such wireless power transfer systems.

The input parameters are: coil dimensions, power transfer distance, center frequency, characteristic impedance, load impedance, and desired input resistance (usually $R'_{in} = Z_0$).

The output parameters are optimized values of: distances between adjacent coils and external capacitors C_2 and C_3.

Plots are also generated of: S-parameters, Z-parameters, and magnitude and phase of current in each coil.

CHAPTER 5: SIMULATION RESULTS

5.1 Wireless Power Transfer Link

The system was simulated using Advanced Design System (ADS) by Keysight, and High Frequency Structural Simulator (HFSS) by Ansys using the values from the example design section.

5.1.1 Simulation with ADS

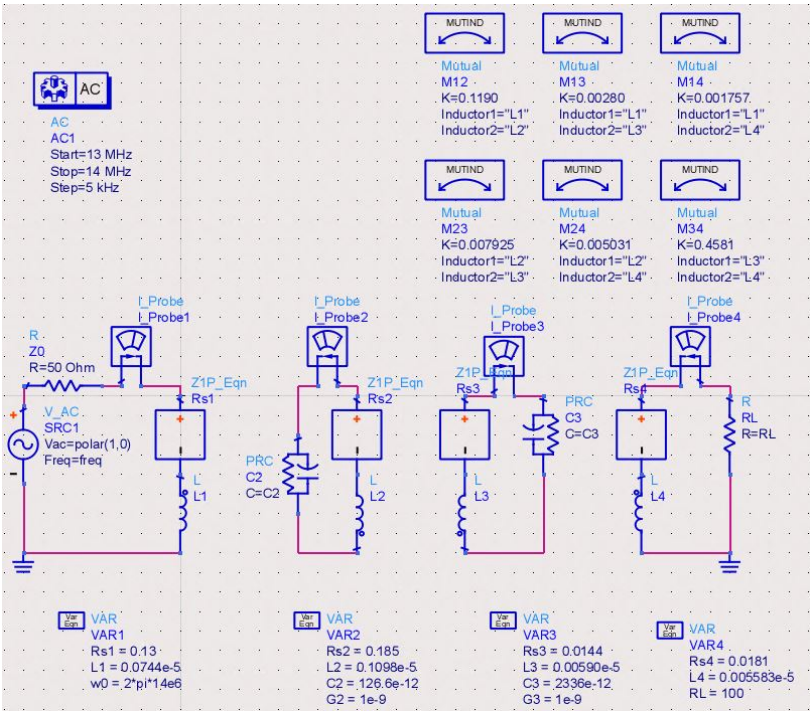

Figure 5.1: ADS Simulation Configuration to Find Coil Currents

The power transfer system was modeled in ADS as shown in Figure 5.1. The Z1P_Eqn blocks, found in the Eqn Based-Linear palette, were used in place of resistors so that the frequency dependent resistance of the loops could be accounted for. The i^{th} resistor block has a value of $Z[1,1] = R_{si}\frac{f}{f_0}$ where f_0 is the frequency at

which the values of R_{si} and L_i were extracted (in HFSS).

As in the analysis, the self capacitance of the loops is ignored. Capacitors C_2 and C_3 represent capacitors physically added to loops two and three. The losses of these capacitors are modeled as a parallel resistor with resistances $\frac{1}{G_2}$ and $\frac{1}{G_3}$.

The coupling coefficients that were not calculated in the example design section were computed using (2.12). From Figure 5.5, it is apparent that the distances used to find K_{14}, K_{13}, and K_{24} are:

$$d_{14} = d_{12} + d_{23} + d_{34}$$

$$d_{13} = d_{12} + d_{23}$$

$$d_{24} = d_{23} + d_{34}$$

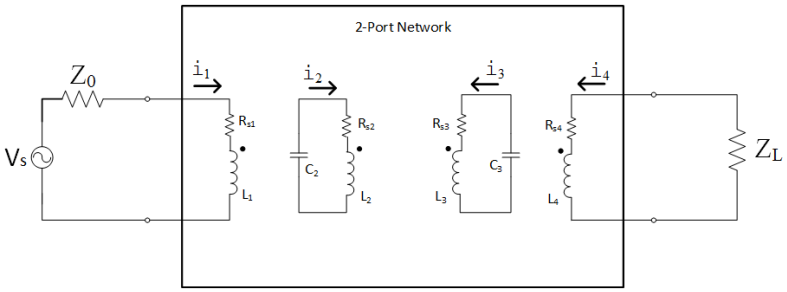

Figure 5.2: ADS Simulation Configuration to Find Coil Currents

Figure 5.1 depicts the circuit used to simulate the current in each loop. In order to verify that the simulation matches the calculations, an analysis similar to that of finding the Z parameters of the system may be performed.

In particular, KVL may be applied to each loop of the circuit in Figure 5.1 resulting

in (5.1) – (5.4).

$$V_s - Z_1 i_1 - Z_{12} i_2 - Z_{13} i_3 - Z_{14} i_4 = 0 \tag{5.1}$$

$$-Z_{12} i_1 - Z_2 i_2 - Z_{23} i_3 - Z_{24} i_4 = 0 \tag{5.2}$$

$$-Z_{13} i_1 - Z_{23} i_2 - Z_3 i_3 - Z_{34} i_4 = 0 \tag{5.3}$$

$$-Z_{14} i_1 - Z_{24} i_2 - Z_{34} i_3 - Z_4 i_4 = 0 \tag{5.4}$$

where each of the impedances are the same as those defined in the analysis section. Therefore, the current in each loop is given by the solution to the linear system and is given as (5.5). The calculation and simulation are compared in Figure 5.3 and 5.4.

$$\begin{bmatrix} i_1 \\ i_2 \\ i_3 \\ i_4 \end{bmatrix} = \begin{bmatrix} Z_1 & Z_{12} & Z_{13} & Z_{14} \\ Z_{12} & Z_2 & Z_{23} & Z_{24} \\ Z_{13} & Z_{23} & Z_3 & Z_{34} \\ Z_{14} & Z_{24} & Z_{34} & Z_4 \end{bmatrix}^{-1} \begin{bmatrix} Vs \\ 0 \\ 0 \\ 0 \end{bmatrix} \tag{5.5}$$

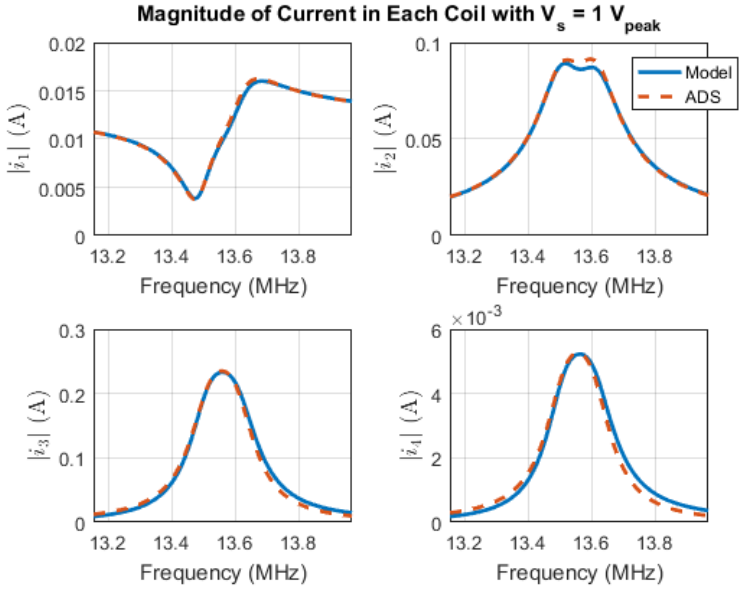

Figure 5.3: The Magnitude of Current as Calculated and Simulated

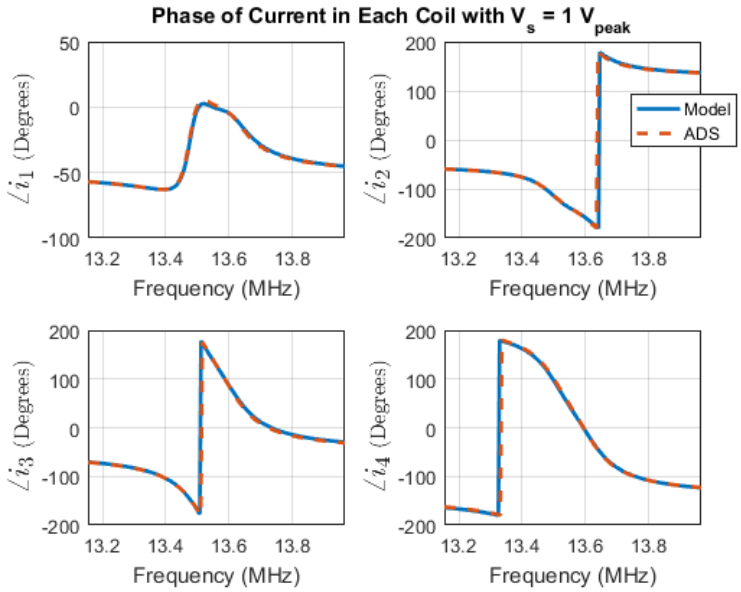

Figure 5.4: The Phase of Current as Calculated and Simulated

Since the simulation and calculation are in good agreement, the analysis based on the circuit model is confirmed. However, the validity of the circuit model must be assessed in order to determine if a physical system will behave the same way.

ADS was also used to find the S-parameters of the circuit, shown in Figure 5.6. MATLAB was used to perform the computations listed in the calculation summary over a range of frequencies so that the simulation results may be overlaid with the mathematical model. The S-parameters of the model are in relatively good agreement within a small interval of the desired operating frequency. The maximum transmission values are $S_{21ADS} = -2.577$ dB and $S_{21Model} = -2.624$ dB

5.1.2 Simulation with HFSS

The entire four coil system was constructed in HFSS as shown in Figure 5.5.

Each of the loops have a small section subtracted out (near x-axis) where a 2D sheet was inserted. Loops 2 and 3 have Lumped RLC Boundaries assigned on their sheets for the external capacitances C_2 and C_3. Loops 1 and 4 have Lumped Ports assigned to their sheets.

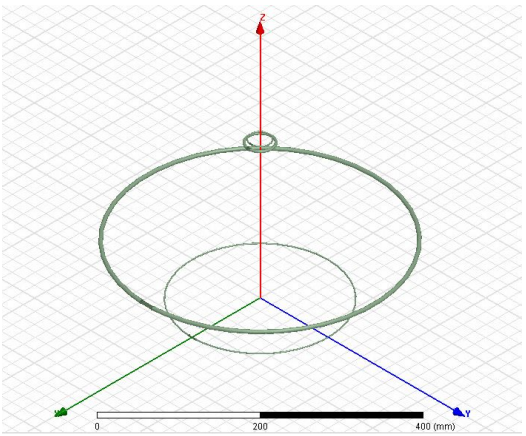

Figure 5.5: WPT System Drawn for Simulation in HFSS

The scattering parameters were solved using HFSS. The resulting plot of transmitted and reflected power of the four loop system may be seen in Figure 5.6. The values assigned in HFSS were the same values as those chosen/computed in the example design section with the exception of capacitor values.

The capacitor values computed in the example design do cause a nice resonant S_{21} peak of about -2.6 dB, however it occurs at 13.625 MHz instead of 13.56 MHz. This is to be expected since the loops do not resonate at exactly $\frac{1}{2\pi\sqrt{LC}}$ which is evident in (2.27) and (2.24) and since there is self-capacitance that is unaccounted for. Instead, (2.42) was used to move the resonance from 13.625 MHz to 13.56 MHz. The values that incur the appropriate shift are $C_2 = 127.8$ pF and $C_3 = 2358$ pF. Using these capacitor values results in a peak transmitted power of $S_{21HFSS} = -2.6965$ dB.

Recall that the calculations heavily depend on the equations for inductance and series resistance of the loops. Therefore, the validity of these equations will be assessed.

5.2 Varactor Impedance Matching

The proposed varactor tunning network was also simulated using ADS. Each component value was swept while holding the others constant in order to determine the effect on input impedance. It was discovered that increasing the inductor value decreases the resonant frequency dramatically, which is depicted in Figure 5.7. Similarly, slight

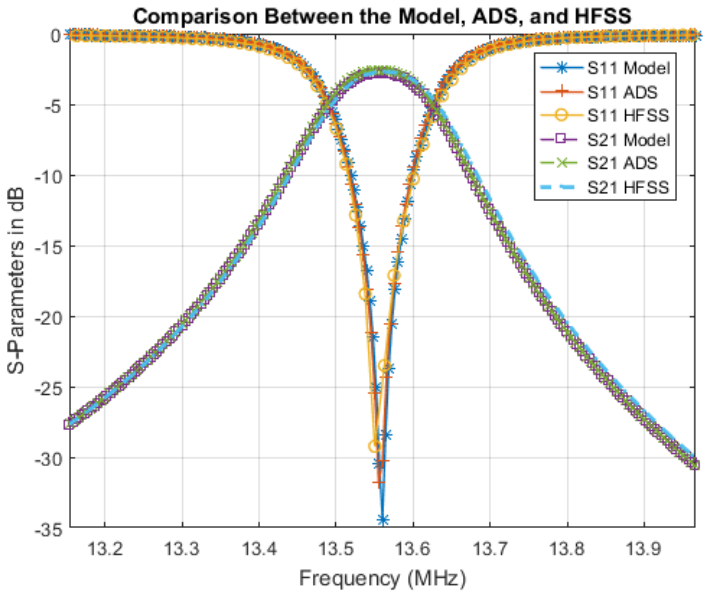

Figure 5.6: S-Parameters of WPT System with Values from [13]

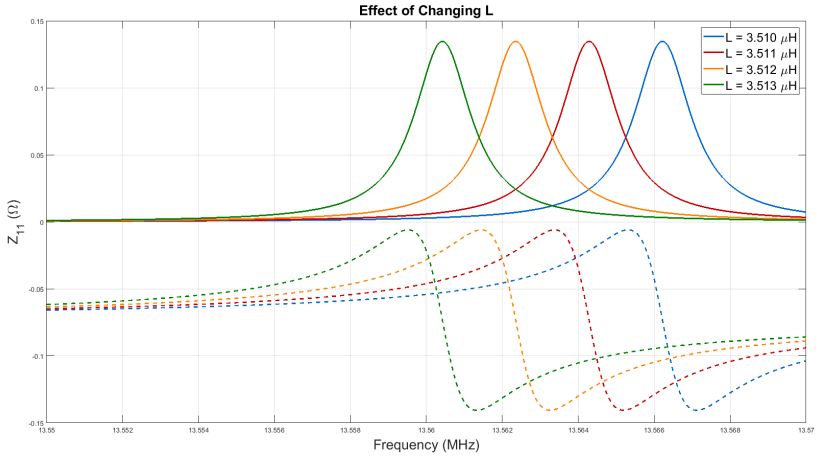

Figure 5.7: Decreased resonant frequency due to increasing the value of L in the proposed Π-network, simulated in ADS.

changes in the second capacitor value also causes a shift in resonant frequency, as depicted in Figure 5.8.

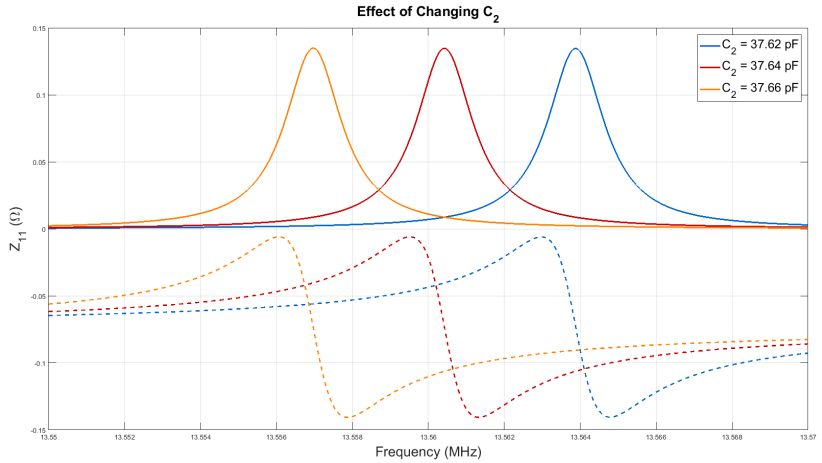

Figure 5.8: Decreased resonant frequency due to increasing the value of C_2 in the proposed Π-network, simulated in ADS.

Another simulation was performed, this time sweeping the value of the first capacitor. Primarily, increasing C_1 only slightly decreases the resonant frequency, but primarily decreases the amplitude of R_{in}, as shown in Figure 5.9. Hence, a tunable impedance matching network may be created by making C_1 a variable capacitor.

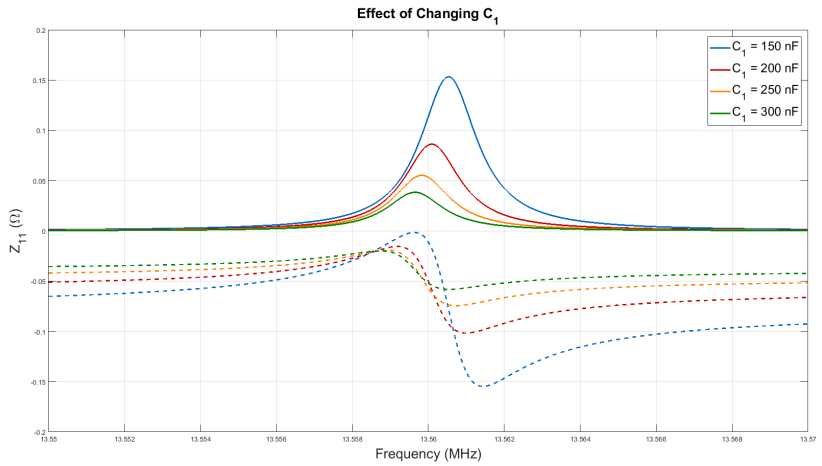

Figure 5.9: Decreased input impedance due to increasing the value of C_1 in the proposed Π-network, simulated in ADS.

Since real inductors must ultimately be used, the effect of adding series resistance to

the inductor was simulated. It was found that , similar to the effect of C_1, increasing the inductor series resistance leads to lower amplitude impedance, depicted in Figure 5.10. Therefore, to overcome losses, simply decrease C_1 to undo the amplitude degredation caused by losses. This will slightly increase the resonant frequency, so it may also be necessary to slightly increase C_2.

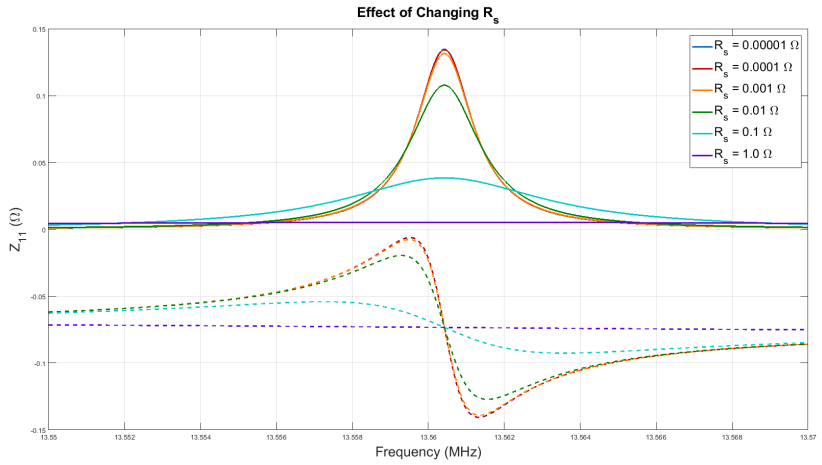

Figure 5.10: Decreased input impedance due to increasing the value of R_s in the proposed Π-network, simulated in ADS.

5.3 Rectifier

Various rectifier topologies were constructed and simulated in ADS to determine if the desired performance was feasible. The transient output voltage response of a fullwave rectifier composed of four Schottkey barrier diodes may be seen in Figure 5.11. The input voltage amplitude was 4V, with a load resistance of 100 Ω and smoothing capacitor of 1μF.

5.4 Load Switch Modulator

The load modulator used to switch between fullwave and voltage doubling rectifier topologies was simulated in ADS. As a result of this modulation, changes in coil current are easily observed in Figure 5.12, and detectable by external-side circuitry. The simulation plot depicts the data-driven gate signal (output from the receiver-side

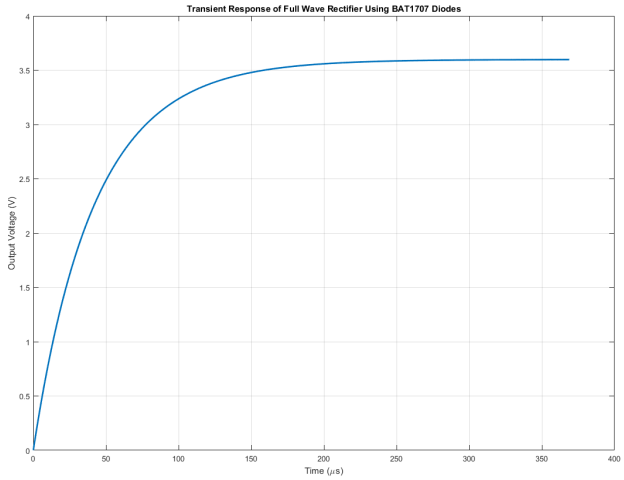

Figure 5.11: The simulated transient response of a fullwave rectifier using BAT1707 diodes and a 100 Ω load resistance with 4V amplitude input.

microcontroller) and corresponding secondary coil current.

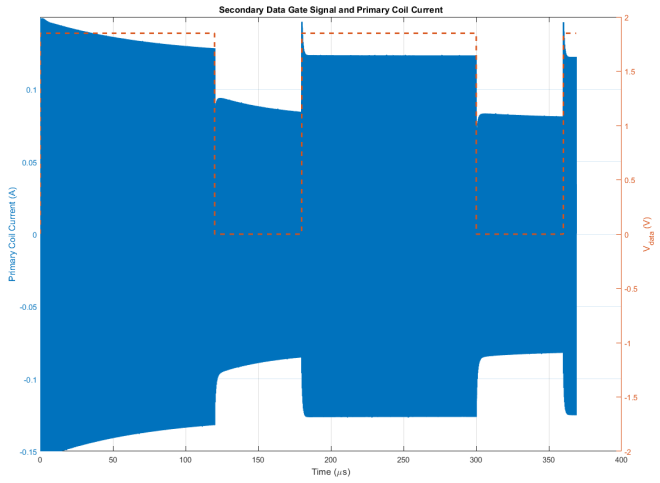

Figure 5.12: The simulated change in coil current as a result of load modulation.

Since the external and implanted circuits are linked through mututal inductance, these current changes will propagate to the external transmitter-side and may be recovered, thus closing the power transfer loop.

CHAPTER 6: CONCLUSIONS

6.1 Future Work

Although a lot of work has been completed here, it is only the beginning of this project. The remainder of the project will be carried out by successors who may choose to draw upon this as a starting point. This section describes work left to be completed, and suggested steps to be taken in order for overall system completion.

6.1.1 Neural Data Transmission

The recorded ECoG data needs to be transmitted back to the external world in some way. Originally it was intended that this data would use the same link as the reverse telemetry using LSK. However, during the design, it was discovered that the dead-time introduced to allow for power settling would cause chunks of data to go missing. This is acceptable for power data since it is not required to be sampled as quickly as the neural electrodes. In fact, a grid of 32 electrodes needs to be sampled around 15 kHz in order to accurately reconstruct the data. This results in 480 kSamples/s, which is well within capability of the RHD2132. Since the RHD2132 uses a 16-bit ADC, this corresponds to 7.68 Mbps data rate – a bit period of 0.13 μs.

Therefore some sort of wireless data link must be created that can handle these speeds. The power transfer coils are optimized for 13.56 MHz, but they also resonate at higher frequencies due to parasitics. It may be possible for them to be used to simultaneously transmit power and receive ECoG data. Whatever the specifics, the data is made available by the RHD2132 and controlled by a microcontroller unit, which should make feeding any antenna system relatively straightforward.

On the primary side, the circuitry has been designed that demodulates the incoming

power data. There is a microcontroller that is responsible for decoding this data into a binary stream. However, some protocol must be developed that takes this binary stream as an input, and outputs a 7-bit binary word that is fed into the 7-bit DAC that controls the DC-DC converter. This portion of the project is a software algorithm that takes place in the microcontroller, requiring no additional circuit design.

Once the antenna transmitter/receiver and supporting circuitry are designed, and a power protocol is developed, the system will be ready to be prototyped.

6.1.2 Miniaturization of Electronics

The analysis and design presented in this work has been focused on developing a proof-of-concept prototype as the first phase of the overall project. As such, there has been little focus on minimizing power consumption or circuit area. Both of these must be revisited before an implantable version can be made.

In order for the circuit to be small enough to be implantable, on-chip circuits will need to be designed to replace many of the off-the-shelf components that have been utilized here. Rather than using large off-chip rectifier diodes, active rectifiers may be designed using MOSFETs on chip. Many active rectifier topologies have been proposed in the literature that have higher conversion efficiency than conventional diode rectifiers [79], [80]. . Therefore, higher overall system efficiency could potentially be improved using one of these topologies for AC-to-DC conversion.

6.1.3 Low-Power Electronics

Inductive coupling is capable of delivering the amount of power required for this application. However, in the event that the SAR levels exceed safe limits for the implantable unit, it may be desirable to alter the system design to use lower power electronics that operate in the microwatt instead of milliwatt range.

REFERENCES

[1] M. A. Sayeed, S. P. Mohanty, E. Kougianos, and H. Zaveri, "An energy efficient epileptic seizure detector," in *2018 IEEE International Conference on Consumer Electronics (ICCE)*, pp. 1–4, Jan 2018.

[2] S. Gabriel, R. W. Lau, and C. Gabriel, "The dielectric properties of biological tissues: Iii. parametric models for the dielectric spectrum of tissues," *Physics in Medicine & Biology*, vol. 41, no. 11, p. 2271, 1996.

[3] H. Jiang, J. M. Zhang, S. S. Liou, R. Fechter, S. Hirose, M. Harrison, and S. Roy, "A high-power versatile wireless power transfer for biomedical implants," in *2010 Annual International Conference of the IEEE Engineering in Medicine and Biology*, pp. 6437–6440, Aug 2010.

[4] T. Biswas, P. Ghosh, B. Manna, A. Banerji, and S. K. Biswas, "Non-radiative wireless power transfer using inductive resonance coupling," in *2017 IEEE Calcutta Conference (CALCON)*, pp. 479–483, Dec 2017.

[5] T. C. Beh, T. Imura, M. Kato, and Y. Hori, "Basic study of improving efficiency of wireless power transfer via magnetic resonance coupling based on impedance matching," in *2010 IEEE International Symposium on Industrial Electronics*, pp. 2011–2016, July 2010.

[6] J. H. Kim and C. H. Ahn, "Method to reduce metal plate effect between transmitter and receiver in wireless power transfer system," *IEEE Antennas and Wireless Propagation Letters*, vol. PP, no. 99, pp. 1–1, 2018.

[7] R. Hua, B. Long, and A. P. Hu, "Enhancing wireless power transfer capability of inductive power transfer system using matrix power repeater," in *2017 IEEE 12th International Conference on Power Electronics and Drive Systems (PEDS)*, pp. 957–961, Dec 2017.

[8] K. L. Montgomery, A. J. Yeh, J. S. Ho, V. Tsao, S. M. Iyer, L. Grosenick, E. A. Ferenczi, Y. Tanabe, K. Deisseroth, S. L. Delp, and A. S. Y. Poon, "Wirelessly powered, fully internal optogenetics for brain, spinal and peripheral circuits in mice," *Nature Methods*, vol. 12, no. 10, pp. 969–974, 2015.

[9] T. Akin, K. Najafi, and R. M. Bradley, "A wireless implantable multichannel digital neural recording system for a micromachined sieve electrode," *IEEE Journal of Solid-State Circuits*, vol. 33, pp. 109–118, Jan 1998.

[10] M. R. Basar, M. Y. Ahmad, J. Cho, and F. B. Ibrahim, "An improved wearable resonant wireless power transfer system for biomedical capsule endoscope," *IEEE Transactions on Industrial Electronics*, vol. PP, no. 99, pp. 1–1, 2018.

[11] G. Wang, W. Liu, M. Sivaprakasam, and G. A. Kendir, "Design and analysis of an adaptive transcutaneous power telemetry for biomedical implants," *IEEE Transactions on Circuits and Systems I: Regular Papers*, vol. 52, pp. 2109–2117, Oct 2005.

[12] "Rhd2000 series digital electrophysiology interface chips," Sep. 2013.

[13] C.-J. Chen, T.-H. Chu, C.-L. Lin, and Z.-C. Jou, "A study of loosely coupled coils for wireless power transfer," *IEEE Transactions on Circuits and Systems – II: Express Briefs*, pp. 536–540, July 2010.

[14] R. S. Fisher, C. Acevedo, A. Arzimanoglou, A. Bogacz, J. H. Cross, C. E. Elger, J. Engel, L. Forsgren, J. A. French, M. Glynn, D. C. Hesdorffer, B. Lee, G. W. Mathern, S. L. Moshe, E. Perucca, I. E. Scheffer, T. Tomson, M. Watanabe, and S. Wiebe, "Ilae official report: A practical clinical definition of epilepsy," *Epilepsia*, vol. 55, no. 4, pp. 475–482.

[15] B. S. Joshi, I. Acharya, and H. P. Zaveri, March 2016.

[16] M. Hampe, "Specific absorption rate in human tissues: Accurate and approximated values," in *2013 International Symposium on Electromagnetic Compatibility*, pp. 143–148, Sept 2013.

[17] C. A. Balanis, *Antenna Theory*. Wiley, 2016.

[18] S. Cecil, G. Schmid, K. Lamedschwandner, J. Morak, G. Schreier, A. Oberleitner, and M. Bammer, "Numerical assessment of specific absorption rate in the human body caused by nfc devices," in *2010 Second International Workshop on Near Field Communication*, pp. 65–70, April 2010.

[19] J. O. Mur-Miranda and G. Fanti, "Peak wireless power transfer using magnetically coupled series resonators," in *2010 IEEE International Energy Conference*, pp. 728–733, Dec 2010.

[20] P. V. Testa, V. RieB, C. Carta, and F. Ellinger, "200 ghz chip-to-chip wireless power transfer," in *2018 IEEE Radio and Wireless Symposium (RWS)*, pp. 117–120, Jan 2018.

[21] K. Agarwal, R. Jegadeesan, Y. X. Guo, and N. V. Thakor, "Wireless power transfer strategies for implantable bioelectronics," *IEEE Reviews in Biomedical Engineering*, vol. 10, pp. 136–161, 2017.

[22] R. Shadid, S. Noghanian, and A. Nejadpak, "A literature survey of wireless power transfer," in *2016 IEEE International Conference on Electro Information Technology (EIT)*, pp. 0782–0787, May 2016.

[23] D. B. Ahire and V. J. Gond, "Wireless power transfer system for biomedical application: A review," in *2017 International Conference on Trends in Electronics and Informatics (ICEI)*, pp. 135–140, May 2017.

[24] J. C. Olivares-Galvan, E. Campero-Littlewood, S. Maximov, S. Magdaleno-Adame, and W. Xu, "Wireless power transfer: Literature survey," in *2013 IEEE International Autumn Meeting on Power Electronics and Computing (ROPEC)*, pp. 1–7, Nov 2013.

[25] H. J. Kim, H. Hirayama, S. Kim, K. J. Han, R. Zhang, and J. W. Choi, "Review of near-field wireless power and communication for biomedical applications," *IEEE Access*, vol. 5, pp. 21264–21285, 2017.

[26] M. Kiani and M. Ghovanloo, "The circuit theory behind coupled-mode magnetic resonance-based wireless power transmission," *IEEE Transactions on Circuits and Systems I: Regular Papers*, vol. 59, pp. 2065–2074, Sept 2012.

[27] A. Kurs, A. Karalis, R. Moffatt, J. D. Joannopoulos, P. Fisher, and M. Soljačić, "Wireless power transfer via strongly coupled magnetic resonances," *Science*, vol. 317, no. 5834, pp. 83–86, 2007.

[28] S. Peng, M. Liu, Z. Tang, and C. Ma, "Optimal design of megahertz wireless power transfer systems for biomedical implants," in *2017 IEEE 26th International Symposium on Industrial Electronics (ISIE)*, pp. 805–810, June 2017.

[29] M. Stanculescu, L. Iordache, M. Iordache, D. Niculae, and V. Bucata, "Using s parameters in wireless power transfer analysis," in *2017 10th International Symposium on Advanced Topics in Electrical Engineering (ATEE)*, pp. 107–112, March 2017.

[30] P. Perez-Nicoli and F. Silveira, "Matching networks for maximum efficiency in two and three coil wireless power transfer systems," in *2016 IEEE 7th Latin American Symposium on Circuits Systems (LASCAS)*, pp. 215–218, Feb 2016.

[31] S. Y. R. Hui, "Magnetic resonance for wireless power transfer [a look back]," *IEEE Power Electronics Magazine*, vol. 3, pp. 14–31, March 2016.

[32] M. Kiani, U. M. Jow, and M. Ghovanloo, "Design and optimization of a 3-coil inductive link for efficient wireless power transmission," *IEEE Transactions on Biomedical Circuits and Systems*, vol. 5, pp. 579–591, Dec 2011.

[33] R. F. Xue, K. W. Cheng, and M. Je, "High-efficiency wireless power transfer for biomedical implants by optimal resonant load transformation," *IEEE Transactions on Circuits and Systems I: Regular Papers*, vol. 60, pp. 867–874, April 2013.

[34] Y. You, B. H. Soong, S. Ramachandran, and W. Liu, "Palm size charging platform with uniform wireless power transfer," in *2010 11th International Conference on Control Automation Robotics Vision*, pp. 85–89, Dec 2010.

[35] S. H. Lee and R. D. Lorenz, "Development and validation of model for 95percent efficiency 220-w wireless power transfer over a 30-cm air gap," *IEEE Transactions on Industry Applications*, vol. 47, pp. 2495–2504, Nov 2011.

[36] P. J. Abatti, C. M. de Miranda, M. A. P. da Silva, and S. F. Pichorim, "Analysis and optimisation of three-coil wireless power transfer systems," *IET Power Electronics*, vol. 11, no. 1, pp. 68–72, 2018.

[37] W. X. Zhong, C. Zhang, X. Liu, and S. Y. R. Hui, "A methodology for making a three-coil wireless power transfer system more energy efficient than a two-coil counterpart for extended transfer distance," *IEEE Transactions on Power Electronics*, vol. 30, pp. 933–942, Feb 2015.

[38] S. Cheon, Y.-H. Kim, S.-Y. Kang, M. L. Lee, J.-M. Lee, and T. Zyung, "Circuit-model-based analysis of a wireless energy-transfer system via coupled magnetic resonances," *IEEE Transactions on Industrial Electronics*, pp. 2906–2914, July 2011.

[39] A. K. RamRakhyani, S. Mirabbasi, and M. Chiao, "Design and optimization of resonance-based efficient wireless power delivery systems for biomedical implants," *IEEE Transactions on Biomedical Circuits and Systems*, pp. 48 – 63, February 2011.

[40] Q. Yuan, Q. Chen, and K. Sawaya, "Maximum transmitting efficiency of wireless power transfer system with resonant/non-resonant transmitting/receiving elements," in *2010 IEEE Antennas and Propagation Society International Symposium*, pp. 1–4, July 2010.

[41] C. L. W. Sonntag, E. A. Lomonova, and J. L. Duarte, "Implementation of the neumann formula for calculating the mutual inductance between planar pcb inductors," in *2008 18th International Conference on Electrical Machines*, pp. 1–6, Sept 2008.

[42] E. B. Rosa and F. W. Grover, "Formulas and tables for mutual and self-inductance," *Washington, D.C.: U.S. Dept. of Commerce, Bureau of Standards*, vol. 8, no. 1, pp. 1–237, 1912.

[43] L. Cohen, "An exact formula for the mutual inductance of coaxial solenoids," *Washington, D.C.: U.S. Dept. of Commerce, Bureau of Standards*, vol. 3, no. 2, pp. 295–303, 1907.

[44] Y. Nishizawa, Y. Narusue, and Y. Kawahara, "Enhancing the quality factor of thin film printed coils for efficient wireless power transfer," in *2018 IEEE Radio and Wireless Symposium (RWS)*, pp. 25–27, Jan 2018.

[45] M. X. Chen and K. W. E. Cheng, "Design of flat magnetic core for inductively coupled coils in high efficiency wireless power transfer application," in *2017 7th International Conference on Power Electronics Systems and Applications - Smart Mobility, Power Transfer Security (PESA)*, pp. 1–7, Dec 2017.

[46] E. Bou, T. Nagashima, H. Sekiya, and E. Alarcon, "Class e2 resonant non-radiative wireless power transfer link: A design-oriented joint circuit-system

co-characterization approach," in *2014 IEEE 11th International Multi-Conference on Systems, Signals Devices (SSD14)*, pp. 1–4, Feb 2014.

[47] T. P. Delhaye, N. AndrÃ©, S. Gilet, C. Gimeno, L. A. Francis, and D. Flandre, "High-efficiency wireless power transfer for mm-size biomedical implants," in *2017 IEEE SENSORS*, pp. 1–3, Oct 2017.

[48] E. Bou-Balust, R. Sedwick, P. Hu, and E. Alarcon, "Advances in non-radiative resonant inductive coupling wireless power transfer: A comparison of alternative circuit and system models driven by emergent applications," in *2014 IEEE International Symposium on Circuits and Systems (ISCAS)*, pp. 2037–2040, June 2014.

[49] Z. Dai, Z. Fang, H. Huang, Y. He, and J. Wang, "Selective omnidirectional magnetic resonant coupling wireless power transfer with multiple-receiver system," *IEEE Access*, vol. PP, no. 99, pp. 1–1, 2018.

[50] R. Erfani, F. Marefat, A. M. Sodagar, and P. Mohseni, "Transcutaneous capacitive wireless power transfer (c-wpt) for biomedical implants," in *2017 IEEE International Symposium on Circuits and Systems (ISCAS)*, pp. 1–4, May 2017.

[51] R. Erfani, F. Marefat, A. M. Sodagar, and P. Mohseni, "Modeling and experimental validation of a capacitive link for wireless power transfer to biomedical implants," *IEEE Transactions on Circuits and Systems II: Express Briefs*, vol. PP, no. 99, pp. 1–1, 2017.

[52] S. Sinha, B. Regensburger, A. Kumar, and K. Afridi, "A very-high-power-transfer-density gan-based capacitive wireless power transfer system," in *2017 IEEE 5th Workshop on Wide Bandgap Power Devices and Applications (WiPDA)*, pp. 360–365, Oct 2017.

[53] J. Lee and S. Nam, "Fundamental aspects of near-field coupling small antennas for wireless power transfer," *IEEE Transactions on Antennas and Propagation*, vol. 58, pp. 3442–3449, Nov 2010.

[54] A. S. Y. Poon, S. O'Driscoll, and T. H. Meng, "Optimal frequency for wireless power transmission into dispersive tissue," *IEEE Transactions on Antennas and Propagation*, vol. 58, pp. 1739–1750, May 2010.

[55] I. J. Yoon and H. Ling, "Realizing efficient wireless power transfer using small folded cylindrical helix dipoles," *IEEE Antennas and Wireless Propagation Letters*, vol. 9, pp. 846–849, 2010.

[56] K. R. Li, K. Y. See, W. J. Koh, and J. W. Zhang, "Design of 2.45 ghz microwave wireless power transfer system for battery charging applications," in *2017 Progress in Electromagnetics Research Symposium - Fall (PIERS - FALL)*, pp. 2417–2423, Nov 2017.

[57] M. I. Abbasi, S. A. Adnan, M. Amin, and F. Kamran, "Wireless power transfer using microwaves at 2.45 ghz ism band," in *6th International Bhurban Conference on Applied Sciences Technology*, pp. 99–102, Jan 2009.

[58] A. Mueed, M. N. Jafri, and S. I. Butt, "Integrated design of rectenna using microstrip patch for wireless power transfer at 4.3 ghz," in *6th International Bhurban Conference on Applied Sciences Technology*, pp. 144–148, Jan 2009.

[59] S. O'Driscoll and T. H. Meng, "Adaptive signal acquisition and wireless power transfer for an implantable prosthesis processor," in *Proceedings of 2010 IEEE International Symposium on Circuits and Systems*, pp. 3589–3592, May 2010.

[60] G. Sun, B. Muneer, Y. Li, and Q. Zhu, "Ultracompact implantable design with integrated wireless power transfer and rf transmission capabilities," *IEEE Transactions on Biomedical Circuits and Systems*, vol. PP, no. 99, pp. 1–11, 2018.

[61] R. Das and H. Yoo, "A multiband antenna associating wireless monitoring and non-leaky wireless power transfer system for biomedical implants," *IEEE Transactions on Microwave Theory and Techniques*, vol. 65, pp. 2485–2495, July 2017.

[62] W. Liu, K. Vichienchom, M. Clements, S. C. DeMarco, C. Hughes, E. McGucken, M. S. Humayun, E. D. Juan, J. D. Weiland, and R. Greenberg, "A neuro-stimulus chip with telemetry unit for retinal prosthetic device," *IEEE Journal of Solid-State Circuits*, vol. 35, pp. 1487–1497, Oct 2000.

[63] C. Sauer, M. Stanacevic, G. Cauwenberghs, and N. Thakor, "Power harvesting and telemetry in cmos for implanted devices," *IEEE Transactions on Circuits and Systems I: Regular Papers*, vol. 52, pp. 2605–2613, Dec 2005.

[64] S. Stoecklin, A. Yousaf, T. Volk, and L. Reindl, "Efficient wireless powering of biomedical sensor systems for multichannel brain implants," *IEEE Transactions on Instrumentation and Measurement*, vol. 65, pp. 754–764, April 2016.

[65] H. Li, J. Li, K. Wang, W. Chen, and X. Yang, "A maximum efficiency point tracking control scheme for wireless power transfer systems using magnetic resonant coupling," *IEEE Transactions on Power Electronics*, vol. 30, pp. 3998–4008, July 2015.

[66] C. Huang, T. Kawajiri, and H. Ishikuro, "A 13.56-mhz wireless power transfer system with enhanced load-transient response and efficiency by fully integrated wireless constant-idle-time control for biomedical implants," *IEEE Journal of Solid-State Circuits*, vol. 53, pp. 538–551, Feb 2018.

[67] K. Kurokawa, "Power waves and the scattering matrix," *IEEE Transactions on Microwave Theory and Techniques*, vol. 13, pp. 194–202, Mar 1965.

[68] F. J. Hyde, S. Deval, and C. Toker, "Varactor diode measurements," *Radio and Electronic Engineer*, vol. 31, pp. 67–75, February 1966.

[69] F. Raab, "Idealized operation of the class e tuned power amplifier," *IEEE Transactions on Circuits and Systems*, vol. 24, pp. 725–735, December 1977.

[70] H. Liu, Q. Shao, and X. Fang, "Modeling and optimization of class-e amplifier at subnominal condition in a wireless power transfer system for biomedical implants," *IEEE Transactions on Biomedical Circuits and Systems*, vol. 11, pp. 35–43, Feb 2017.

[71] F. H. Raab and N. O. Sokal, "Transistor power losses in the class e tuned power amplifier," *IEEE Journal of Solid-State Circuits*, vol. 13, pp. 912–914, Dec 1978.

[72] M. Danilovic, Z. Chen, R. Wang, F. Luo, D. Boroyevich, and P. Mattavelli, "Evaluation of the switching characteristics of a gallium-nitride transistor," in *2011 IEEE Energy Conversion Congress and Exposition*, pp. 2681–2688, Sept 2011.

[73] H. Holler and J. Schrodt, "Theory and performance of rectifiers," *Washington, D.C.: U.S. Dept. of Commerce, Bureau of Standards*, pp. 466–526, 1924.

[74] G. Kriegsmann, "An asymptotic theory of rectification and detection," *IEEE Transactions on Circuits and Systems*, vol. 32, pp. 1064–1068, October 1985.

[75] M. K. Hosain and A. Z. Kouzani, "Design and analysis of efficient rectifiers for wireless power harvesting in dbs devices," in *2013 IEEE 8th Conference on Industrial Electronics and Applications (ICIEA)*, pp. 651–655, June 2013.

[76] Z. Tang, B. Smith, J. H. Schild, and P. H. Peckham, "Data transmission from an implantable biotelemeter by load-shift keying using circuit configuration modulator," *IEEE Transactions on Biomedical Engineering*, vol. 42, pp. 524–528, May 1995.

[77] W. H. Ko, S. P. Liang, and C. D. F. Fung, "Design of radio-frequency powered coils for implant instruments," *Medical and Biological Engineering and Computing*, vol. 15, pp. 634–640, Nov 1977.

[78] D. W. Knight, "Practical continuous functions and formulae for the internal impedance of cylindrical conductors," *G3YNH. info*, April 2016.

[79] L. Cheng, W. H. Ki, and T. S. Yim, "A 13.56 mhz on/off delay-compensated fully-integrated active rectifier for biomedical wireless power transfer systems," in *2017 22nd Asia and South Pacific Design Automation Conference (ASP-DAC)*, pp. 31–32, Jan 2017.

[80] Q. Li, J. Wang, and Y. Inoue, "A high efficiency cmos rectifier with on-off response compensation for wireless power transfer in biomedical applications," in *2014 International Symposium on Integrated Circuits (ISIC)*, pp. 91–94, Dec 2014.

[81] E. B. Rosa and L. Cohen, "Formulas and tables for the calculation of mutual and self-inductance," *Washington, D.C.: U.S. Dept. of Commerce, Bureau of Standards*, vol. 5, no. 1, pp. 1–132, 1909.

APPENDIX A: Selected Components

A.1 Transmitter Components

Specific components have been selected to realize the power transmitter circuitry presented in Figure 1.17. In many cases, the components have been modeled using Advanced Design System for simulation. The list of major transmitter components are given with their respective power losses for 1 Watt input power. The total transmitter loss is about 360 mW.

Table A.1: Selected Components for Proof-of-Concept Transmitter with Corresponding Power Losses Assuming Tx Input Power of 1 Watt.

Component	**Subcircuit**	**Manufacturer**	**Part Number**	**Maximum Power Consumption (mW)**
MCU	Power Control Unit	Analog Devices	ADuCM360	21
DAC	Power Control Unit	Linear Technologies	LTC7106	5
Buck Converter	Power Control Unit	Linear Technologies	LTC3610	50
Power MOSFET	Power Control Unit	Vishay	SiS438DN	12
GaNFET	Power Amplifier	Efficient Power Conversion	EPC2010C	25
Heatsink	Power Amplifier	Aavid	531202B02500G	N / A
Crystal Oscillator	Power Amplifier	Kyocera	KC3225K13.5600C1GE00	18
Gate Driver	Power Amplifier	IXYS	IXDI602SIA	54
Toroidal Ferrite Core	Power Amplifier	TDK	B64290L0022X830	27
Diode	Detector	Diodes Inc.	B120-13-F	5
Amp / Comparator	Detector	Texas Instruments	LM392	5
Loop 1	Inductive Link	N / A	N / A	8
Loop 2	Inductive Link	N / A	N / A	140

A.2 Receiver Components

Specific components have been selected to realize the power receiver circuitry presented in Figure 1.17. In many cases, the components have been modeled using Advanced Design System for simulation. The list of major receiver components are given in Table A.2 with their respective power losses for 1 Watt input power. The total transmitter loss is about 330 mW.

The total system loss for both transmitter and receiver is about 690 mW for 1 Watt input. The calculated values assume a 15 cm separation between transmitter and receiver. The total system efficiency is about 31%. The power loss values have been extracted from each components' datasheet. The conditions in datasheets are often

Table A.2: Selected Components for Proof-of-Concept Receiver with Corresponding Power Losses Assuming Tx Power of 1 Watt.

Component	**Subcircuit**	**Manufacturer**	**Part Number**	**Maximum Power Consumption (mW)**
MCU	Reverse Telemetry / Matching	Analog Devices	ADUCM360	21
MOSFET Switch	Reverse Telemetry	Infineon	BSD235N	3
4x Schottkey Diodes	Rectifier	Infineon	BAT1707	100
Zener Diode	Regulator	Diodes Inc.	DDZ4V3BSF	80
LDO	Regulator	Linear Technologies	LT1521	31
Varactor Diode	Matching Network	Skyworks	SMV1702-011LF	3
Loop 4	Matching Network	N / A	N / A	0.2
Loop 3	Inductive Link	N / A	N / A	93
ECoG Chip	Recording Circuitry	Intan Technologies	RHD2132	5

somewhat idealistic and can be hard to replicate. Therefore, even in the presence of a 50% derating, the total system efficiency is still 15%, which is acceptable for this application.

APPENDIX B: Extraction of Power Transfer Coil Parameters

In order to design inductive wireless power transfer systems like the ones presented here, it is imperative to know each coil's physical properties. However, determining these values is not a trivial task. The specific required properties are the self-inductance, mutual-inductances, and AC resistance. Some expressions for these are listed in this appendix for the reader's convenience. However, they are not intended to be a catch-all set of expressions; additional work may be required to find an expression that fits the specifics of a particular system.

B.1 Self Inductance

The self-inductance of a circular, single turn loop may be approximated as (B.1)

$$L = \mu r \left(\ln \frac{8r}{a} - 2 + \frac{Y}{2} \right) \tag{B.1}$$

where r is the loop radius, and a is the wire radius. This expression is valid when $r >> a$.

The self-inductance of a rectangular loop may be approximated as (B.2)

$$\begin{aligned} L = \frac{\mu}{4\pi} \Bigg[& c \ln \frac{2c}{a} + d \ln \frac{2d}{a} - (c+d)(2 - \frac{Y}{2}) \\ & + 2\sqrt{c^2 + d^2} - c\sinh^{-1}\left(\frac{c}{d}\right) - d\sinh^{-1}\left(\frac{d}{c}\right) + a \Bigg] \end{aligned} \tag{B.2}$$

For a circular coil with multiple turns, consider using Wheeler's formula (B.3). This can also represent a planar spiral.

$$L = \frac{1 \times 10^{-6} a^2 n^2}{8a + 11b} \tag{B.3}$$

For a multi-turn coil composed of multiple layers, consider using (B.4). Multi-layer

coil with n total turns

$$L = \frac{0.8 \times 10^{-6} a^2 n^2}{6a + 9b + 10c} \tag{B.4}$$

Inductance of helical coil composed of an infinitesimally thin current sheet

$$L_{sheet} = \frac{4\mu_0 N^2 r^2}{3l\sqrt{1-k^2}} \left[\frac{1-k^2}{k}(K(k) - E(k)) + E(k) - k \right] \tag{B.5}$$

A correction inductance may be defined in order to account for round wires instead of a current sheet. The corrected inductance is then $L = L_{sheet} - \Delta L$.

$$\Delta L = 4 \times 10^{-9} \pi r N \left(\frac{5}{4} - \ln\left(\frac{p}{a}\right) + \frac{2}{N} \sum_{m=1}^{N-1} \sum_{i=1}^{\infty} \frac{N-m}{2i(2i+1)(i+1)m^{2i}} \right) \tag{B.6}$$

$$L = \mu_0 N^2 a \left(\ln\left(1 + \frac{\pi a}{b}\right) + \frac{1}{2.3 + 1.6\left(\frac{b}{a}\right) + 0.44\left(\frac{b}{a}\right)^2} \right) \tag{B.7}$$

B.2 Mutual Inductance

The mutual inductance between two coaxial circular multi-turn coils is given by (B.8) [81]

$$\begin{aligned} M_{12} = 4\pi\sqrt{r_1 r_2}\frac{1}{k}\left[(2-k^2)F(k) - 2E(k)\right] \\ + \frac{1}{24}\left[(b_1^2 + b_2^2)\frac{d^2 M_0}{dx^2} + c_1^2 \frac{d^2 M_0}{dr_1^2} + c_2^2 \frac{d^2 M_0}{dr_2^2}\right] \end{aligned} \tag{B.8}$$

where d is the mean distance between the coils, the turns occupy a cross sectional area given by $b_i \times c_i$, and

$$\begin{aligned} \frac{d^2 M_0}{dr_i^2} &= \pi \frac{k}{r_i}\left[(2-k^2)F(k) - \left(2 - k^2 \frac{1-2k^2}{1-k^2}\right)E(k)\right] \\ \frac{d^2 M_0}{dx^2} &= \pi \frac{k^3}{r_1}\left[F(k) - \frac{1-2k^2}{1-k^2}E(k)\right] \end{aligned}$$

In the special case where the two circles have only one turn each, a similar formula may be used (B.9) [42]. This formula makes use of the double factorial operator, which successively multiplies same parity integers, such as $8!! = 8 \cdot 6 \cdot 4 \cdot 2$.

$$M = \frac{\pi^2 k^3}{4}\sqrt{r_1 r_2}\left[1 + \frac{1}{8}\sum_{n=1}^{\infty}\left(\frac{(2n+1)!!}{(2n)!!}\right)^2 \frac{k^{2n}}{(2n-1)(n+1)}\right] \tag{B.9}$$

The mutual inductance between two closed circuits may be calculated through Neumann's integral formula as described by (2.10). This expression may be discretized so that it may be solved numerically, as described in (B.10)

$$M_{ij} \approx \frac{\mu}{4\pi}\sum_{\alpha=1}^{n^i}\sum_{\beta=1}^{n^j}\frac{\Delta\bar{r}_\alpha^i \cdot \Delta\bar{r}_\beta^j}{\left|\bar{r}_\alpha^i - \bar{r}_\beta^j\right|} \tag{B.10}$$

where each $\bar{r}_k$ is the position vector that maps the parameterized coil k. Therefore, $\Delta\bar{r}_\gamma^k$ is the γ-th position vector increment along coil k such that $\Delta\bar{r}_\gamma^k = \bar{r}_k(\gamma+1) - \bar{r}_k(\gamma)$. n^k is the discrete number of points that are used in coil k's discretation.

B.3 Equivalent Series Resistance

A very important parameter necessary for accurate modeling of a wireless power transfer system is a coil's frequency dependent series resistance. This formula may be approximated using (B.11)

$$R_{ac} = \frac{l}{\sigma\delta_i(d - \delta_i)} \tag{B.11}$$

where l is the arc length of the coil, σ is the conductivity, d is the wire diameter, and δ_i is the skin depth, denoted as (B.12).

$$\delta_i = \sqrt{\frac{2}{\sigma\omega\mu}} \tag{B.12}$$

David Knight has performed extensive research on the calculation of effective AC resistance. One accurate expression presented by Knight in [78] was mentioned

previously as (4.3).

VITA

Luke Stuemke attended the University of North Carolina from 2012 to 2015 where he obtained a Bachelor of Science in Electrical Engineering. He continued from 2016 to 2018 to pursue a Master of Science in Electrical Engineering. His research interests include wireless power transfer, microwave and radio frequency circuits, and electromagnetics.